Theoretical Study of C–H Bond Activation by Mononuclear and Dinuclear High-Valent Iron Complexes

Dissertation

zur

Erlangung des Doktorgrades (Dr. rer. nat.)

der

Mathematisch-Naturwissenschaftlichen Fakultät

der

Rheinischen Friedrich-Wilhelms-Universität Bonn

vorgelegt von

Caiyun Geng

aus

Pingdu, Shandong, China

Bonn 2012

Angefertigt mit Genehmigung der Mathematisch-Naturwissenschaftlichen Fakultät der
Rheinischen Friedrich-Wilhelms-Universität Bonn

1. Gutachter: Prof. Dr. Frank Neese

2. Gutachter: Prof. Dr. Stefan Grimme

Tag der Promotion: 28.09.2012

Erscheinungsjahr: 2012

Abstract

The C–H bond activation by high-valent iron complexes have been investigated into detail using density functional theory (DFT). The first part of the present PhD thesis concerns with the reaction mechanism of C–H bond hydroxylation by mononuclear iron(IV)oxo model complexes ($[Fe^{IV}(O)(NH_3)_5]^{2+}$ (**a**), $[Fe^{IV}(O)(OH)_{(axial)}(NH_3)_4]^{+}$ (**b**), $[Fe^{IV}(O)(OH)_{2(eq)}(NH_3)_3]$ (**c**)). In addition to the classical σ-pathway for quintet state ($^5\sigma$) and π-pathway ($^3\pi$) for triplet state, two new reaction pathways, $^5\pi$ and $^3\sigma$, have been established. This is the first time that all viable reaction pathways for the C–H bond hydroxylation by high-valent iron(IV)-oxo complex have been identified in the same system. The new triplet σ pathway ($^3\sigma$) is too high in energy to be involved in C–H bond activation, but the reactivity of the quintet π channel ($^5\pi$) is comparable or even higher than the triplet pathway. The existence of at least three energetically feasible pathways may offer, however, a new element of specificity control in C–H bond activation reactions by iron(IV)–oxo species.

The second part of the thesis deals with the H-atom abstraction reactivity of six hypothetic iron–oxo ($Fe(O)(NH_3)_4(OH)_{axial}$) and iron–nitrido ($Fe(N)(NH_3)_4(OH)_{axial}$) model complexes. The iron oxidation state ranges from IV to VI. The calculations reveal that the iron-oxo species (**1 – 3**) and their nitrido analogues (**4 – 6**) feature dramatically different intrinsic reactivity towards C-H bonds. In the case of the iron-oxo series, the reactivity order of **1** < **2** << **3** was observed, reflecting an increase in the electrophilicity of iron-oxo complexes upon the increased iron oxidation state. Surprisingly, the iron-nitrido series is not as reactive as its oxo counterpart and the reactivity order was inverted in the oxidation of ethane C-H bonds, i.e., **4** ≥ **5** > **6**. All these results correlated well with the Bell-Evans-Polanyi principle in which a linear relationship between the energy barrier and the thermodynamic driving force was observed. Furthermore, the different properties of the iron–oxo and –nitrido complexes as well as the counterintuitive reactivity of these two series were understood by analyzing the thermodynamical nature of H-atom affinity, i.e. its electron and proton affinity component.

The C–H bond activation by four high-valent diiron complexes, two with diamond core structure, ($Fe^{III}(\mu\text{-oxo})_2Fe^{IV}$, **1** and $Fe^{IV}(\mu\text{-oxo})_2Fe^{IV}$ **2**) and two with open core structure (OH-Fe^{IV}-O-Fe^{IV}=O, **3** and OH-Fe^{III}-O-Fe^{IV}=O, **4**) was reported in the third part of this thesis. Our calculations show that, processing from **1** to **4**, the computed barriers decrease and follow the order **1** < **2** < **3** < **4**, in good agreement with the reactivity trend observed experimentally (Xue, G.; De Hont, R.; Münck, E.; Que, L. *Nature Chem.* **2010**, *2*, 400–405.). Their reaction mechanisms fall essentially into two categories, hydrogen atom

transfer in the case of **1**, **3** and **4** and hydride transfer for **2**. The different reactivity of complexes **1** – **4** can be well rationalized by the thermodynamic and kinetic considerations. First, the thermochemistry has successfully captured the essence of the hydride transfer reaction by **2** that, there is a thermodynamic preference of 27.5 kcal/mol for hydride transfer pathway than that for HAT. Second, the relative sluggish reactivity of diamond core complexes **1** and **2** can be attributed to the higher energetic penalty required for the structural arrangements upon redox processes than the open core ones **3** and **4**. Finally, the highest efficiency of HAT by complex **4** originates from the thermodynamic and kinetic preference. The strongest O–H bond formed during the oxidation process by **4** offers the largest thermodynamic driving force, and the lowest reorganization energy both for the diiron reagent and substrate makes **4** also favorable in kinetic aspect.

The last part of the present thesis is about the hydrogen bond effect in modulating C–H bond activation. The C–H bond activation by two high-valent localized open core diiron complexes (**1**-OH_{cis}, $OH–Fe^{III}–O–Fe^{IV}=O$ and **1**-F_{trans}, $F–Fe^{III}–O–Fe^{IV}=O$) have been explored using DFT. The computed geometry parameters of these two complexes show that **1**-OH_{cis} adopts a *cis* conformation in which an H–bond is formed between the terminal oxo and hydroxo group. However, a *trans* conformation is established for **1**-F_{trans}. Our detailed reactivity study demonstrates that **1**-F_{trans} displays even higher oxidation power than that of **1**-OH_{cis}, which is in good agreement with the experimental findings. Furthermore, our calculations revealed that the hydrogen bond between the oxo and hydroxo group in **1**-OH_{cis} does not significantly change the electrophilicity of the reactive $Fe^{IV}=O$ unit. However, during the reaction of C-H bond oxidation, this hydrogen bond has to be partially broken. This leads to the slightly higher barrier for **1**-OH_{cis} relative to **1**-F_{trans}, which has similar open-core structure but no hydrogen bond.

LIST OF PUBLICATION

PUBLICATIONS RELATED TO THE THESIS

- **Chapter 3**

  C. Geng, S. Ye, F. Neese. **Analysis of Reaction Channels for Alkane Hydroxylation by Nonheme Iron(IV)oxo Complexes.** *Angew. Chem. Int. Ed*. 2010, 49, 5717 –5720

  In this work all viable reaction pathways for the C–H bond hydroxylation by high-valent iron(IV)-oxo complex have been identified in the same system. This is the first time to show the complete picture of the reaction mechanism of this kind of reactions. I carried out the entire study.

- **Chapter 4**

  C. Geng, S. Ye, F. Neese. **Does a Higher Oxidation State of a Metal Center Necessarily Imply Higher Oxidizing Power? A Computational Study of C-H Bond Activation by High–Valent Iron–oxo and –nitrido Complexes**. To be submitted to *Chem. Sci.*

  In this work the different reactivity of high-valent iron–oxo and –nitrido complexes toward C-H bond activation was studied by using six model complexes. The iron oxidation states are ranging from IV to VI. I carried out the entire study.

- **Chapter 5**

  C. Geng, S. Ye, F. Neese. **Differences in and Comparison of the Catalytic Properties of Diiron complexes with Diamond Core or Open Core Structures: A Theoretical Study**. To be submitted to *Chem. Sci.*

  In this work the different reactivity of four diiron complexes towards C-H bond activation was investigated by theoretical approach. I carried out the entire study.

- **Chapter 6**

  C. Geng, S. Ye, F. Neese. **Hydrogen bonding effects on the reactivity of [X-Fe^{III}–O–Fe^{IV}=O] (X = OH, F) complexes towards C–H bond cleavage.**

  In this work the hydrogen effects on the reactivity of [X-Fe^{III}–O–Fe^{IV}=O] (X = OH, F) complexes towards C–H bond cleavage was studied in a combined experimental and computational approach. I carried out the entire quantum chemical study.

Acknowledgements

Here is the place and time to say “thank you” to everybody who, in one way or other, contributed to my life during my years in Germany. Some of you helped me by simply being my friends, and some even took part in my research and, of course, all of you made it possible for me to come to “the finish”.

First of all, I would like to express my gratitude to my supervisor Frank Neese who gave me the opportunity to make my PhD here in Germany. It is really an honor to be your student! Thank you very much Frank! – For your scientific guidance, invariable support and patience!

My special thanks to Dr. Shengfa Ye, who has done a lot in my whole Ph.D study. Thank you very much for the insightful discussions and the expert suggestions and comments about my research!

I would like to thank all past and present members of our group, whom I had the pleasure to meet, for making a positive and enjoyable working environment. Especially, I would like to give my heartfelt thanks to Vera and Barbara who are always being available to help.

I dedicate this thesis to family; especially my loving parents. You have been taking care of my son for nearly four years! It is very hard to find words to thank you for your unconditional love and support. My dear husband Jilai, thank you for your love and care, constant help and encouragement! Also thanks a lot for scientific discussions during my study and comments about the design of my thesis. I love you very much! And finally, my little sunshine – my sweet son Zengguan, thank you for your appearance in my life and mum loves you so much and wants to stay with you for every second from now on! In a word, all your love and support are the vehicles that drove this thing over the finish line. And it would mean nothing without you to share it with.

This work was financially supported by the China Scholarship Council (CSC) (for the first three and half years) and Max Planck Society (for the last half year).

Contents

List of Schemes xi

List of Tables xiii

List of Figures xv

Nomenclature xix

1. Introduction 1

1.1 Iron-oxo complexes 2

1.1.1 Iron-oxo complex in biology 2

1.1.2 Biologically inspired catalysis 6

1.1.3 C-H bond activations 10

1.2 Nitrido complexes 17

1.3 The aim of current thesis 18

2. Theoretical Background and Methods 21

2.1 Elementary quantum chemistry 21

2.2 Density functional theory 22

2.3 Reaction mechanism 24

2.4 Transition State Theory 25

2.5 Solvent effects 28

2.6 Chemical models 29

2.7 Calculations setup 29

3. Analysis of Reaction Channels for Alkane Hydroxylation by Nonheme Iron(IV)oxo Complexes 31

3.1 Introduction 31

3.2 Computational details 33

3.3 Results and discussion 34

3.4 Conclusion 38

4. Does a Higher Oxidation State of a Metal Center Necessarily Imply Higher Oxidizing Power? A Computational Study of C-H Bond Activation by High–Valent Iron–oxo and –nitrido Complexes 41

4.1 Introduction 41

4.2 Computational details 43

4.3 Results....44
4.3.1 Geometry structures....44
4.3.2 Reactivity....47
4.4 Discussion....53
4.5 Conclusions....57
5. Differences in and Comparison of the C-H Bond Oxidation Activity by Diiron Complexes with Diamond Core or Open Core Structures: A DFT Study....59
5.1 Introduction....59
5.2 Computational details....61
5.3 Results and discussion....61
5.3.1 Geometric and Electronic Structures of Complexes 1 – 4.....61
5.3.2 Reactivity....62
5.4 Discussion....67
5.4.1 Reaction driving force.....67
5.4.2 Kinetic considerations....69
5.3.3 The relevance to Marcus Theory....71
5.4 Conclusion....72
6. Hydrogen Bonding Effects on the Reactivity of [X-Fe^{III}–O–Fe^{IV}=O] (X = OH, F) Complexes towards C–H Bond Cleavage....73
6.1 Introduction....73
6.2 Computational details....75
6.3 Results and discussion....75
6.3.1 Geometric structure....75
6.3.2 Reactivity....76
6.3.3 Discussion....78
6.4 Conclusion....80
7. Conclusion....83
Bibliography....85

List of Schemes

Scheme 3. 1 The feasible reaction channels for the H-atom abstraction by oxo-iron(IV) complexes. 32

Scheme 4. 1 Six high-valent iron–oxo and –nitrido complexes.....43

Scheme 5. 1 Scheme 5.1. Core structures and supporting ligand of complexes 1–4, F, ferromagnetic; AF antiferromagnetic. 61
Scheme 5. 2 Orbital occupancy-evolution diagrams during C-H bond oxidation and the corresponding orbital-selection rules for predicting transition state structures. 64
Scheme 5. 3 Comparison of the reaction driving forces of DHA C-H bond oxidation by complex 2 with the different reaction pathways. 67

Scheme 6. 1 Structures of high-valent diiron complexes. 74

List of Tables

Table 3. 1 Geometric parameters of the transition states of complexes a, b and c. 34

Table 4. 1 Calculated Energies and Selected Geometric Parameters and electronic structures for the high-valent Iron–Oxo and –Nitrido Complexes predicted by B3LYP calculations (Energy in kcal/mol and Bond Distances in Angstroms).....47
Table 4. 2 Selected Key Geometric Parameters of Transition States for C-H Bond Activation by the high-valent Iron Oxo and Nitrido Complexes (Bond Distances in Angstrom, Angles in Degree).....49
Table 4. 3 B3LYP Calculated Reaction Energies (kcal/mol) and Bond Dissociation Energies (kca/mol) for the Most Feasible Reaction Pathway of Iron-Oxo and -Nitrido Complexes...54

Table 6. 1 Selected Geometry Parameters for the Key Points along the Reaction Pathways. Normal, with VDW effect. In parentheses, values without VDW effect are given.....81
Table 6. 2 BP86 Calculated Geometry Parameters for the Key Points along the Reaction Pathways. Normal, with VDW effect. In parentheses, without VDW effect. 81

List of Figures

Figure 1. 1 Schematic representation of the different intermediates generated during the catalytic cycle of cytochrome P450 3
Figure 1. 2 The proposed mechanism of Taurine hydroxylation catalyzed by TauD.....5
Figure 1. 3 Catalytic of O2 activation and alkane hydroxylation in sMMO. 6
Figure 1. 4 Correlation between electron richness of iron(IV)-oxo complexes and their reactivity. 7
Figure 1. 5 Axial ligand effects on the O-atom transfer (dotted line) and H-atom abstraction (bold line) reactivity of complex [(TMP$^{-\bullet}$)Fe^{IV}(O)(X)] (X = $CF_3SO_3^-$, Cl^-, AcO^-, OH^-). 7
Figure 1. 6 Polydentate chelating ligands used in the synthesis of iron non-heme biomimetic complexes.....9
Figure 1. 7 The four synthesized high-spin iron(IV)-oxo complexes.....10
Figure 1. 8 The proposed rebound mechanism for C–H bond hydroxylation. 11
Figure 1. 9 Schematic summary of the electronic changes along the reaction pathway in the heme-base iron(IV)-oxo catalysts.....11
Figure 1. 10 Schematic summary of the electronic structure changes along the reaction pathway in the triplet and quintet state of mononuclear non-heme iron(IV)-oxo complexes. 13
Figure 1. 11 Rebound mechanism for the hydroxylation of substrate by sMMO. 14
Figure 1. 12 Noradical mechanism proposed in the Yoshizawa model of sMMO.....14
Figure 1. 13 The two-oxidant hypothesis using CpdI and Cpd0, and a probe substrate (P) that can open differently depending on whether it leads to radical or a cationic intermediate. 14
Figure 1. 14 B3LYP/LACV3P++**//LACVP-calculated TSR/MSR scenario during hydroxylation of cyclohexane by [(N4Py)Fe^{IV}O]$^{2+}$.....15
Figure 1. 15 Thermodynamic cycle describing the BDE_{OH} (a), and the relationship between redox potential and pK_a for a metal-oxo species in the cleavage of a C–H bond in methane (b).....17

Figure 2. 1 The chart showing the PES of an elementary single-step bimolecule reaction.26

Figure 3. 1 Schematic Gibbs free energy (ΔG) energy surface for ethane hydroxylation by three model systems: (A) B3LYP/def2-TZVPP//B3LYP/TZVP, (B) CCSD(T) (def2-TZVP for Fe, N, O and def2-SV(P) for H atoms)//B3LYP/TZVP. 36
Figure 3. 2 Schematic MO diagram of $^5TS_{H\pi}$ (A), $^3TS_{H\sigma}$ (B), $^5TS_{Re\sigma}$ (C) for $[Fe^{IV}(O)(NH_3)_5]^{2+}$...37

Figure 4. 1 B3LYP Calculated Schematic MO diagrams for complex 2 and 3. 44
Figure 4. 2 B3LYP Calculated Schematic MO diagrams for complexes 4, 5 and 6. 46

Figure 4. 3 Schematic energy profiles (ΔH) for the ethane hydroxylation by complexes 1 ($[Fe^{IV}O(OH)(NH_3)_4]^+$) and 2 ($[Fe^{V}O(OH)(NH_3)_4]^{2+}$). 48
Figure 4. 4 Schematic MO diagram of $^2TSH_\pi$ and $^4TSH_\pi$ for complex 5 $[Fe^{V}O(OH)(NH_3)_4]^{2+}$. C grey, N blue, O red, Fe orange. 49
Figure 4. 5 Schematic Gibbs free energy (ΔG) surfaces for the ethane C-H bond activation by the $[Fe^{IV}N(OH)(NH_3)_4]$ (4) and $[Fe^{V}N(OH)(NH_3)_4]^+$ (5) systems. 50
Figure 4. 6 Schematic MO diagram of $^3TSH_\pi$, $^5TSH_\sigma$ and $^5TSH_\pi$ for $[Fe^{IV}N(OH)(NH_3)_4]$ (4). C grey, N blue, O red, Fe orange. 51
Figure 4. 7 Schematic MO diagram of $^2TSH_\pi$ and $^4TSH_\pi$ for $[Fe^{V}N(OH)(NH_3)_4]^+$ (5). C grey, N blue, O red, Fe orange. 52
Figure 4. 8 Schematic energy profiles (ΔH) for most feasible pathway of ethane H-tom abstraction by complexes 1 – 6. 53
Figure 4. 9 Plots of the reaction energy barrier ($\Delta H^{\ddagger}$) for the reaction with 1 – 5 as a function of the driving force (ΔH). 54
Figure 4. 10 Correlation between reaction exothermicity with BDE_{EH}. 55
Figure 4. 11 B3LYP Calculated Relative Adiabatic Electron and Proton Affinity for most feasible reaction pathways of Iron-Oxo and -Nitrido Complexes. 56

Figure 5. 1 B3LYP optimized structures and spin populations of key atoms in core structure for complexes 1 – 4. Fe green, O red, N blue, C grey, H white. 62
Figure 5. 2 Potential energy surfaces for DHA C–H bond oxidation by complexes 1 – 4, and the comparison of rate constants obtained from experiments and DFT calculations. The blue bars represent experimental reaction rates, whereas the red bars correspond to the calculated relative rate constants using 1 as reference. 63
Figure 5. 3 B3LYP calculated transition state structures and spin populations for the key atoms. Fe green, O red, N blue, C grey, H white. 64
Figure 5. 4 Orbital occupancy-evolution diagrams for C–H bond activation by 2. 65
Figure 5. 5 Orbital occupancy-evolution diagrams for C–H bond activation by 3. 66
Figure 5. 6 Overlays of the geometries of complex 1 – 4 (green line) and their corresponding transition state (magenta line). For clarity, all hydrogen atoms and the substrate in the transition states are not shown. 66
Figure 5. 7 B3LYP Calculated Relative Adiabatic Electron Affinities for Complexes 1 – 4, Proton Affinities for Their One-Electron Reduced Form and Bond Dissociation Energies for the O-H Bond of Their Intermediates. 68
Figure 5. 8 Three energetic contributions to the reaction barriers for DHA C-H bond oxidation by complexes 1 – 4. 70

Figure 6. 1 Optimized Core structures of 1-OH and 1-F. Bond lengths are in angstroms, angles in degrees. Atom color scheme: H, white; O, red; Fe, orange; F, green. 75
Figure 6. 2 The geometric data from previous theoretical results for $1\text{-}OH_{cis}$ and $1\text{-}F_{trans}$.[262] 76

Figure 6. 3 Calculated Schematic Gibbs free energy (ΔG) surfaces for DHA C-H bond activation by 1-OH_{cis}, 1-F_{trans} and 1-OH_{trans}. In parentheses, energies without inclusion of VDW effects are given. 77
Figure 6. 4 BP86 Calculated Schematic Gibbs free energy (ΔG) surfaces for DHA C-H bond activation by 1-OH_{cis} and 1-F_{trans}. In parentheses energies with inclusion of VDW effects are given. 77
Figure 6. 5 Space-filling models of reaction complexes (RCs) and transition states (TSHs) for 1-F_{trans}, 1-OH_{cis} and 1-OH_{trans}. Atom color scheme: C, gray; H, white; N, blue; O, red; Fe, orange; F, green.....79

Nomenclature

P450	cytochromes P450
LS	Low Spin
HS	High Spin
CpdI	Compound I
αKGD	α-ketoglutarate dependent dioxygenases
αKG	α-ketoglutarate
sMMO	Soluble methane monooxygenase
EXAFS	Extend X-ray Absorption Fine Structure
KIE	Kinetic Isotopic Effect
TSR	Two-state Reactivity
MSR	Multistate Reactivity
BDE	Bond Dissociation Energy
MOH	Metal-hydroxo
QM	Quantum Mechanics
HF	Hartree-Fock
MO	Molecular Orbital
LCAO	Linear Combination of Atomic Orbitals
MCSCF	Multiconfigurational Self-consistent Field
CASSCF	Complete Active Space Self-consistent Field
DFT	Density Functional Theory
KS	Kohn-Sham
LDA	Local Density Approximation
LSDA	Local Spin Density Approximation
GGA	Generalized Gradient Approximation
TS	Transition State
PES	Potential Energy Surface

TST	Transition State Theory
COSMO	Conductor-like Screening Model
VDW	van der Waals
HAT	Hydrogen Atom Transfer
EA	Electron Affinity
PA	Proton Affinity

1. Introduction

The selective transformation of ubiquitous but inert C–H bonds to other functional groups has far-reaching practical implications, even though it has been studied for over 100 years. The thermodynamic stability of most C–H bonds is often cited as the most common reason for their underutilization in chemical synthesis.[1] To overcome the thermodynamic barrier, one has to use reagents that are highly oxidizing, nonselective, and often incompatible with other functional groups. In addition, many of these oxidants contain expensive and toxic metal ions, whose cost and environment incompatibilities would limit their use. Therefore, the development of new reagents that are efficient, benign, and easily accessible toward specific C–H bond activation is currently an important area in chemical science.

Directly linked to the quest for new reagents for C–H functionalization are investigations into the chemistry of metal complexes with dioxygen, a connection arising from the prevalence of metal-containing oxygenases that selectively cleave C–H bonds.[2-8] These metalloproteins typically contain one or more metal ions within their active sites, which first bind and activate dioxygen, initially producing what are believed to be high valent metal–oxo species that then cleave C–H bonds of substrates. There are several features of metalloenzyme-catalyzed C-H bonds functionalization: 1) These enzymes have evolved to efficiently perform these transformations under mild conditions; 2) metalloenzyme-catalyzed oxidation exhibits exquisite substrate specificity as well as regioselectivity and/or stereoselectivity; 3) most metalloenzymes achieve this challenging task by using cheap, abundant and environmental friendly first-row transition metals, like iron, copper and manganese. Therefore, unveiling the key chemical principles that underlie their high efficacy will enable people to gain atomic level insight into catalytic reactivity of the enzymes and could also shed light on synthesizing new reagents that can modify target C–H bonds with high efficiency and specificity.

In this chapter, a brief review of metalloenzyme-catalyzed C-H bonds functionalization in biology will be given, and then the development of synthetic catalysts that model enzymatic functions will be summarized, based on the significant advances in understanding of how these enzymes functionalize.

1.1 Iron-oxo complexes

1.1.1 Iron-oxo complex in biology

1.1.1.1 The heme paradigm

The most extensively studied oxygen-activating enzymes are the cytochromes P450 (P450).[9-12] P450 represent a large superfamily of heme thiolate proteins, which catalyze a great variety of stereospecific and regioselective oxygen insertion processes into organic compounds. Generally, the P450s react as monooxygenase that transfer one oxygen atom originating from molecular oxygen to the substrate, which is either hydroxylated (aliphatic or aromatic), epoxidized, or sulfoxidized.[13-17] These processes are of vital importance in biochemical transformations ranging from biodegradation of toxic compounds in the liver to the biosynthesis of hormones in the body. Furthermore, its drug metabolism and involvement in brain chemistry make this enzyme a target for the drug industry and biochemical research.[10]

The consensus oxygen activation mechanism for P450 is referred to as the heme paradigm (Figure 1.1). The main steps include: (i) substrate binding to the Fe^{3+} center of P450 (**A**); this step usually perturbs the water ligand coordinated as the sixth ligand of the heme iron and changes the low-spin (LS) state in **A** to a high-spin (HS) state in the substrate-bound complex **B**. (ii) first electron reduction to build up a Fe^{2+} state; the Fe^{3+} state has a more positive reduction potential and thus is much easier reduced to the ferrous state (**C**). (iii) binding of O_2 to the Fe^{2+} heme; oxygen binding leads to an oxy-P450 complex (**D**), which is the last relatively stable intermediate in the reaction cycle. (iv) delivery of the second electron; the second reduction step is the rate-determining step in many P450s; this relative slow step generates a negatively charged iron(III)-peroxo complex (**E**). (v) delivery of the first proton; the protonation of the terminal oxygen atom in **E** produces a P450-Fe^{III}-OOH intermediate **F**. (vi) cleavage of the O-O bond in the oxygen derived ligand; this step is also called the second protonation step in which formally an iron(V)-oxo species **G** and a water molecule are generated by heterolytic cleavage of the O-O bond. (vii) insertion of an oxygen atom into the substrate and release of the hydroxylation product. Steps (vi) (vii) are certainly the most complicated ones to understand, owing to the fleeting nature of the intermediates.

The high-valent iron complex **G** is regarded as the active oxidant toward C–H bond activation. This complex termed as Compound I (CpdI) in P450 enzymes has one oxidizing equivalent that is not stored at the iron center but instead delocalized on the porphyrin marcocycle ring, and hence is best formulated as an iron(IV)-oxo unit chelated by a

porphyrin π-radical. The fleeting nature of this intermediate has long been a big obstacle for its assignment as the active oxidant in P450, only indirect evidence from biomimetic and computational studies[18,19] supported its existence.[18,19] Until recently, Rittle and Green have successfully trapped and characterized CpdI using Mössbauer, electron paramagnetic resonance, and UV-Vis spectroscopic methods, and provided unambiguous proof for its activity in substrate hydroxylation.[20]

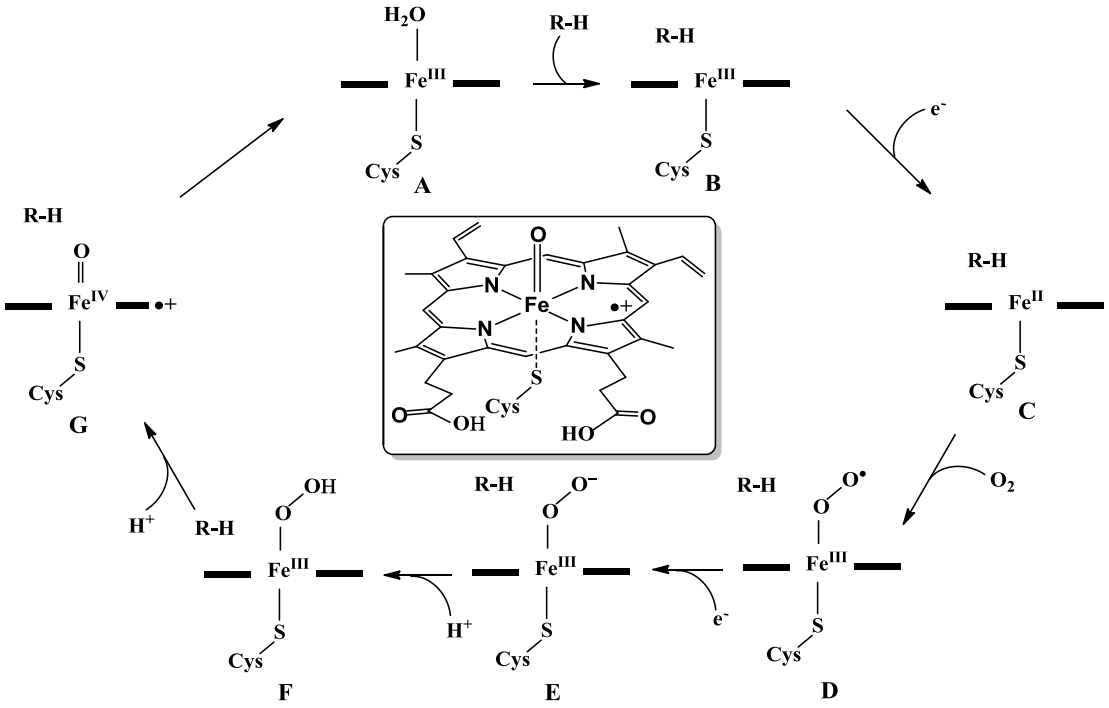

Figure 1. 1 Schematic representation of the different intermediates generated during the catalytic cycle of cytochrome P450

1.1.1.2 Non-heme iron enzymes

Two types of high-valent iron-oxo active sites have been identified in non-heme enzymes. The first type involves mononuclear iron centers that are coordinated to two histidines and a carboxylated group, thereby forming a characteristic 2-his-1-carboxylate facial triad, which has been recognized as a common structural motif for many mononuclear non-heme iron enzymes.[8,21,22] In contrast to the monooxygenase P450 enzymes that use only one atom of molecular oxygen to hydroxylate substrates while the second oxygen atom leaves the process as water, this type of non-heme enzymes are able to utilize both oxygen atoms of molecular oxygen and therefore work as dioxygenase. One of the most important dioxygenase is the α-ketoglutarate dependent dioxygenases (αKGD), which are involved in e.g. the biosynthesis of collagen in mammals and antibiotics in microbes.[23-25]

The big difference between αKGD and P450 enzymes, however, is the fact that the dioxygenase are non-heme enzymes that do not contain a co-enzyme but utilize α-ketoglutarate (αKG) as a cosubstrate instead. Taking the extensively studied αKGD enzyme, TauD, as an example, the proposed catalytic mechanisms for non-heme iron enzymes are shown in Figure 1.2. The cycle starts from the resting state (**H**), where the active center is a six-coordinated iron(II) ligated by two histidine amino acid residues (His_{99}, His_{205}), a carboxylic acid group from Asp_{101} and three water molecules. The initial step in the cycle is binding of αKG via its C-1 carboxylate and ketone oxygen to the Fe(II) center of the binary enzyme:Fe(II) complex, with displacement of two water ligands. The next step in the catalytic cycle is substrate (taurine) binding and leads to formation of a five-coordinated Fe(II) site by dissociation of a third coordinated water molecule (**J**). Upon dioxygen binding (intermediate **K**) the catalytic cycle enters a grey zone, where the intermediates react so fast and only limited information about the individual intermediates is known. It has been postulated that the dioxygen molecule take an end-on attack to the open coordinate site on the Fe(II) (complex **L**), followed by a nucleophilic attack of the uncoordinated oxygen atom of O_2 on the carbonyl of αKG yielding succinate and an oxo–iron species (complex **M**). In 2003, intermediate **M** has been trapped and characterized with various spectroscopic techniques, such as Mössbauer, resonance Raman, and X-ray asbsorption spectroscopies, showing that the intermediates have a high-spin (S = 2) iron(IV)-oxo unit with double bond character between the iron and oxygen atom. The high-valent iron(IV)-oxo intermediates have been identified as the key active oxidizing species for other non-heme enzymes as well.[7,26,27] The iron(IV)-oxo species subsequently abstracts a hydrogen atom from taurine (complex **N**) and rebounds the hydroxyl group to the rest group to form the product complex (**O**). Release of products (succinate and hydroxylated taurine) and rebinding of water molecules to the active center brings the catalytic cycle back into the resting state.

There is an alternative key reactive species proposed in the mononuclear non-heme iron enzymes. Mechanistic studies of naphthalene 1,2-dioxygenase, a member of the Rieske dioxygenase family, point strongly towards the involvement of a highly electrophilic iron(V)-oxo species, but with only indirect proof of its existence.[8,26,28-32] Very recently, using variable-temperature mass spectrometry, Prate a al. provided evidence for such a reactive intermediate in a synthetic system.[33]

The second type of non-heme enzymes contains carboxylate-bridged non-heme diiron active sites, which are associated with methane and toluene monooxygenases, fatty acid desaturases and ribonucleotide reductase.[34,35] Soluble methane monooxygenase (sMMO) is a well-studied case and can convert methane into methanol. The sMMO consists of three separate protein components termed (i) hydroxylase (MMOH), (ii) NADH oxidoreductase (MMOR), and (iii) regulatory protein (MMOB).[36,37] Kinetic and spectroscopic studies have shown that the reactions of oxygen activation and substrate

hydroxylation occur at MMOH site which has an $(\alpha\beta\gamma)_2$ subunit structure with a bis-*u*-hydroxo dinuclear Fe(III) cluster in the active site of the α-subunit.[37-39] The mechanism of this diiron non-heme enzyme is similar to those of mononuclear heme- and non-heme containing enzymes, that is, the O_2 is activated through a reductive process that results in O–O bond cleavage and then generation of a high-valent iron–oxo reactive species (Figure 1.3).

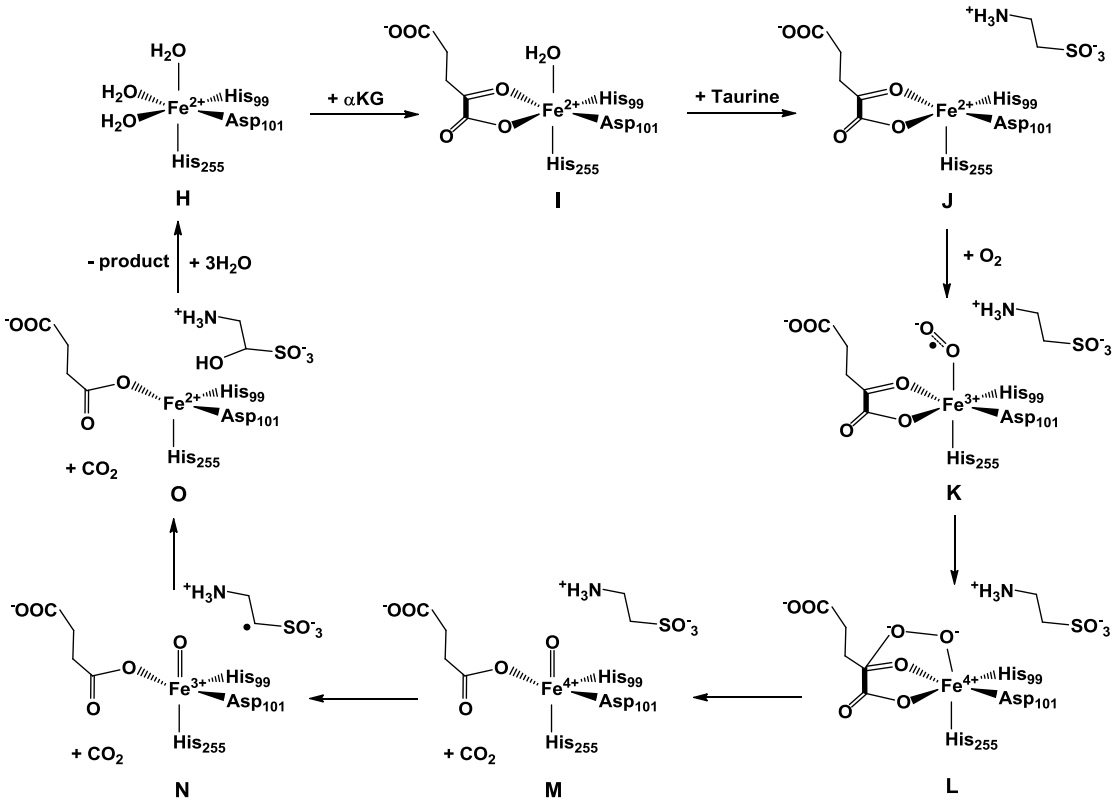

Figure 1. 2 The proposed mechanism of Taurine hydroxylation catalyzed by TauD.

Intermediate **Q** is considered as the key oxidizing species in the catalytic cycle of sMMO, performing the chemical challenging conversion of methane to methanol. A detailed analysis of EXAFS and Mössbauser spectroscopic data by Que, Münck, and coworkers revealed that Q is best described as a strongly exchange-coupled diiron(IV) species with an Fe···Fe distance of 2.46 Å and pairs of short and long Fe–O bonds of 1.77 and 2.05 Å, respectively, consistent with an $[Fe^{IV}_2(u\text{-}O)_2]$ diamond core.[40,41]

In all the non-heme iron enzymes, the iron(IV) center has been found to be in a HS $S = 2$ state, presumably due to the weak ligand field exerted by a combination of histidine and carboxylate weak ligands.

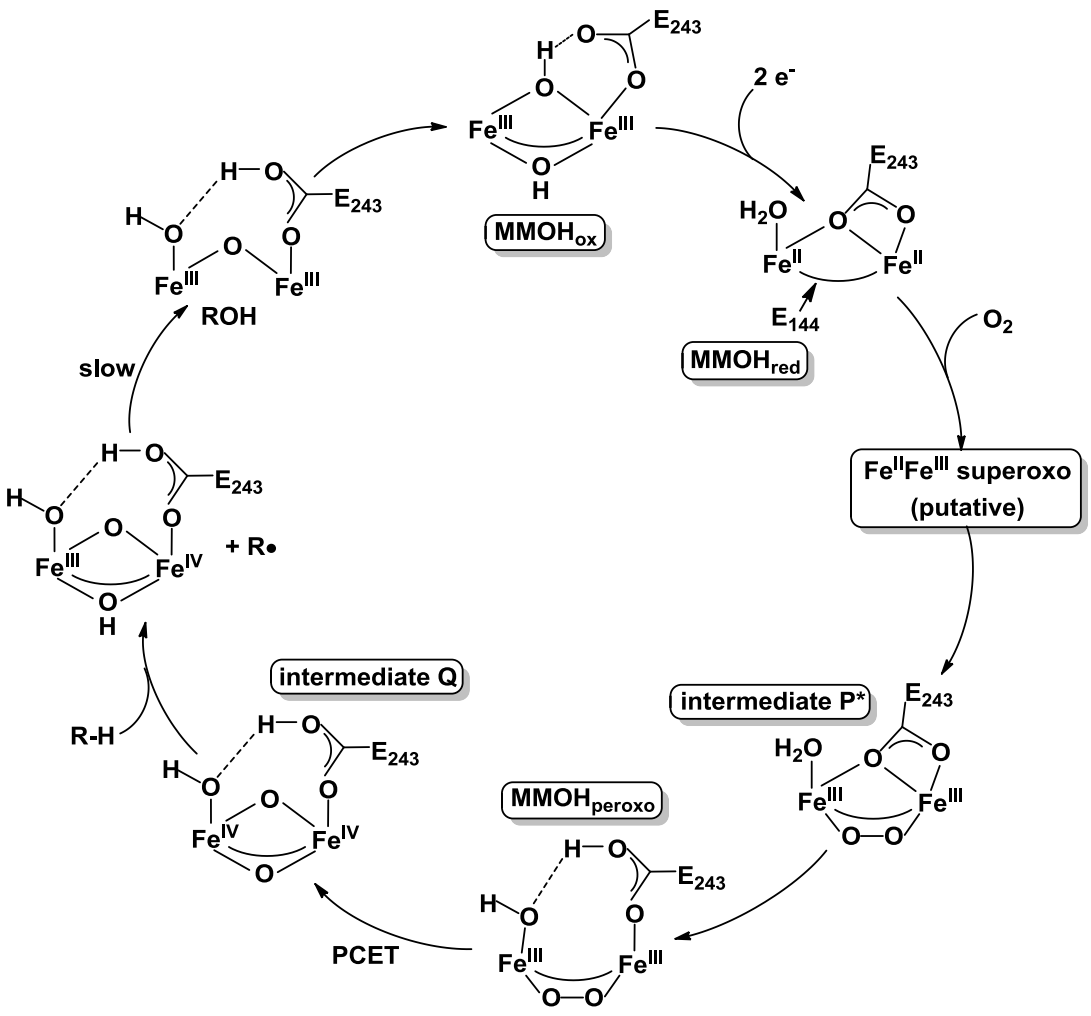

Figure 1. 3 Catalytic of O2 activation and alkane hydroxylation in sMMO.

1.1.2 Biologically inspired catalysis

One of the major goals of bioinorganic chemistry is the elucidation of factors that determine enzymes' ability to active inert C-H bonds. Central to these efforts have been attempts to obtain electronic and geometric characterization of the highly reactive intermediates, high-valent iron(IV)-oxo species, which is thought to be responsible for such demanding oxidation.[18,42,43] However, due to the different locations of the two oxidizing equivalents in the high-valent iron(IV)-oxo species, i.e. the two oxidizing equivalents are distributed between the iron center and the porphyrin ligand for P450, between the two iron centers in sMMO and are localized on the mononuclear iron center of TauD, there are thus several possible strategies for developing biomimetic catalysts.

1.1.2.1 Heme-based biomimetic catalysts

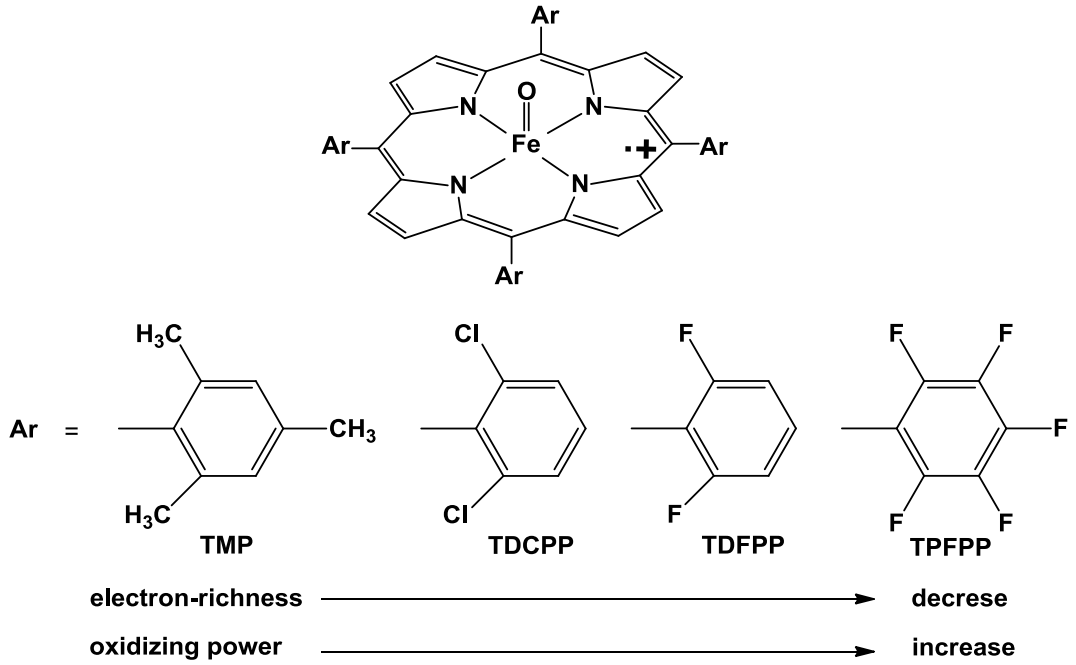

Figure 1. 4 Correlation between electron richness of iron(IV)-oxo complexes and their reactivity.[44]

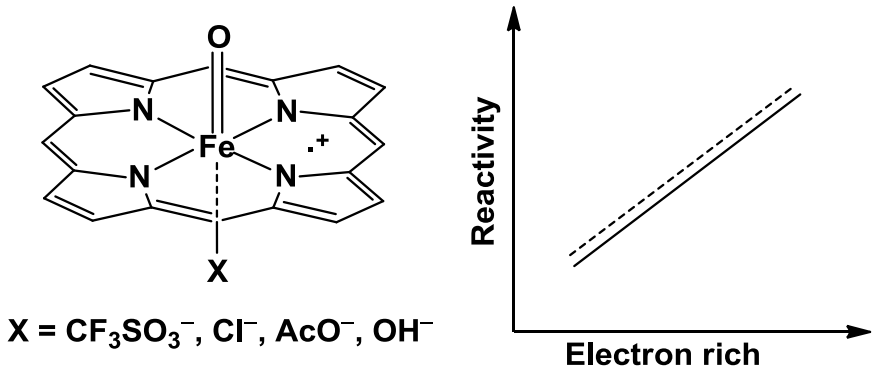

Figure 1. 5 Axial ligand effects on the O-atom transfer (dotted line) and H-atom abstraction (bold line) reactivity of complex [($TMP^{-\bullet}$)Fe^{IV}(O)(X)] (X = $CF_3SO_3^-$, Cl^-, AcO^-, OH^-).[45]

Much effort has been invested into the development of metalloporphyrin catalysts that mimic the reactivity of P450.[46] The first high-valent iron(IV)-oxo porphyrin π-radical intermediate was synthesized and characterized in 1981 by Groves and co-workers.[47] In the reaction of [(TMP)Fe^{III}(Cl)] (TMP = meso-tetramesityl porphinate dianion) with meta-chloroperbenzoic acid in a dichloromethane-methanol mixture at –78°C, a green species, which is best described as an iron(IV)-oxo coordinated with a porphyrin π-radical, [(TMP$^-$

$^{\bullet}$)$Fe^{IV}(O)(CH_3OH)]^+$ has been detected on the basis of various spectroscopic measurements. This species exhibits the characteristic features of CpdI intermediates and was found to be the kinetically competent oxidant in olefin epoxidation and alkane hydroxylation.[48-50] Since then, a number of iron(IV)-oxo porphyrin π-radicals bearing electron-rich and –deficient porphyrins and with different axial ligands have been prepared in an effort to understand the electronic effects of porphyrin and axial ligands on the reactivity of the iron(IV)-oxo intermediates.[22,48,49,51] The results of these studies indicate that the electronic properties of porphyrin ligands control the oxidizing power of iron-oxo porphyrins, and that iron(IV)-oxo species with electron-deficient porphyrin ligands exhibit higher reactivity towards oxygenation of organic substrates (Figure 1.4).[44] The axial ligands bound trans to the iron-oxo moiety also remarkably influence the reactivity of the iron(IV)-oxo porpyrin π-radicals. For example, a study reported by Gross *et al*., in which pronounced axial ligand effect has been observed in the O-atom transfer reactions with a range of complexes [($TMP^{-\bullet}$)$Fe^{IV}(O)(X)$] bearing different axial ligands. The results shows that [($TMP^{-\bullet}$)$Fe^{IV}(O)(X)$] complexes bearing ligating anionic ligands (e.g., F^-, Cl^-, and $CH_3CO_2^-$) have a greater reactivity than those bearing nonligating anions (e.g., $CF_3SO_3^-$ and ClO_4^-) in the epoxidation of styrenes.[52] Very recently, an investigation of a series complexes [($TMP^{-\bullet}$)$Fe^{IV}(O)$(*p*-Y-pyO)]$^+$ (Y = OCH_3, CH_3, H, Cl) and [($TMP^{-\bullet}$)$Fe^{IV}(O)(X)$] (X = $CF_3SO_3^-$, Cl^-, AcO^-, OH^-) in H-atom abstraction and O-atom transfer reactions by Kang *et al*. showed that the reaction rates of both the O-atom transfer and H-atom abstraction increase with increasing electron donation from the axial ligand (Figure 1.5).[45] Thus, all the results mentioned above have been extended to correlate the strong oxidizing power of the thiolate-ligated P450 enzyme whereby the cysteinate ligang creates a “push-effect” and donates electron density to the heme iron center.[12]

1.1.2.2 Non-heme-based biomimetic catalysts

In contrast to the heme-inspired systems in which the synthesis and characterization of an iron(IV)-oxo porphyrin species appeared in 1981,[47] the original report of a non-heme iron(IV)-oxo complex appeared almost two decades later in 2000.[53] A non-heme iron(IV)-oxo intermediate in the reaction of [Fe^{III}(cyclam-acetato)(CF_3SO_3)]$^+$ and O_3 in acetone and water at –80°C was detected spectroscopically by Wieghardt and co-workers for the first time; this green species was characterized as an intermediate-spin (IS) Fe(IV)-oxo (*S* = 1) intermediate based on the Mössbauer analysis.[53] Subsequently, the first well-characterized mononuclear non-heme iron(IV)-oxo complex was reported in 2003. Münck, Nam, Que, and their co-workers reported the first X-ray crystal structure of a mononuclear *S* = 1 iron(IV)-oxo complex that was generated in the reaction of [(Me_4cyclam)$Fe^{II}(CH_3CN)]^{2+}$ (Me_4cyclam = 1,4,8,11-tetramethylcyclam) and iodosobenzene (PhIO) in CH_3CN at –40°C.[54] This intermediate was characterized with various

spectroscopic methods and features a short Fe=O bond distance of 1.646(3) Å.[54-56] Since then, extensive efforts have been devoted to examining the reactivities of mononuclear non-heme oxoiron(IV) complexes bearing macrocyclic tetradentate N4, tripodal tetradentate N4, and pentadentate N5 and N4S ligands in the oxidation of various substrates, including alkane hydroxylation, olefin epoxidation, alcohol oxidation, N-dealkylation, and the oxidation of sulfides and PPh_3.[26,51,57-71] (Figure 1.6).

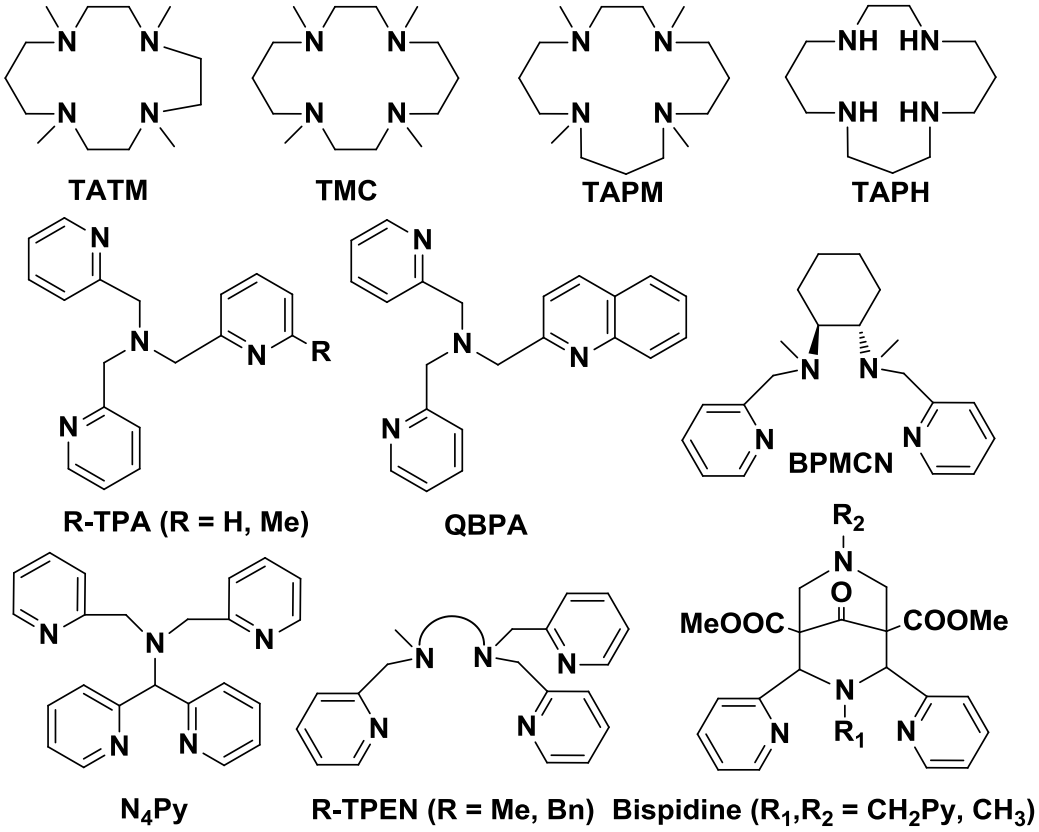

Figure 1. 6 Polydentate chelating ligands used in the synthesis of iron non-heme biomimetic complexes.

The most challenge task in laboratory chemistry now is to synthesize Fe(IV)=O reagents that possess high-spin, *S* = 2 ground states as found in nature. Indeed, synthetic high-spin iron(IV)-oxo complexes remain rare and are limited to seminal contributions by Bakac, Que, Borovik and Chang (Figure 1.7).[72-76] In these complexes, the iron(IV)-oxo core is mainly protected by the sterically bulky chelator which would attenuate their reactivity towards C–H bond cleavage. As such, the identification and characterization of new high-spin state iron(IV)-oxo complexes, particular with high efficiency towards C–H bond activation, is of fundamental interest in elucidating underlying principles of their reactivity.

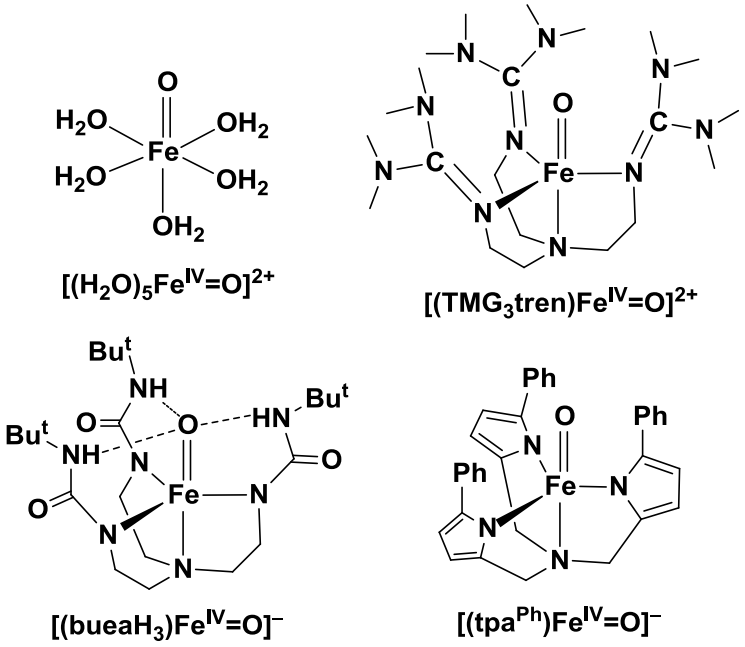

Figure 1. 7 The four synthesized high-spin iron(IV)-oxo complexes.

In contrast to the great number of synthesized iron(IV)-oxo complexes, the true iron(V)-oxo complexes are rather rare. Till now, the sole iron(V)-oxo complex was spectroscopically characterized by Collins et al.[77] This compound is supported by a tetraanionic ligand, which is likely quench its electrophilicity, and was found to be a sluggish oxidant, reacting with the weak C–H bond of dihydroanthracene only.[77]

Although considerable effort has been made by synthetic chemists to prepare viable models for the putative reaction intermediates in sMMO, the nature of the high-valent diiron(IV) intermediate Q remains less understood than those of mononuclear iron(IV)-oxo compounds.[51] A synthetic precedent for the $[Fe^{IV}_2(u\text{-}O)_2]$ diamond core proposed for intermediate Q has been recently reported by Xue *et al*..[40] By electrochemical oxidation of the precursor $[(^{Me2(OMe)}TPA)_2Fe^{III/IV}(u\text{-}O)_2](ClO_4)_3$ (with $^{Me2(OMe)}TPA$ = tris(3,5-dimethyl-4-methoxypyridyl-2-methyl)amine), they succeeded in preparing the first and only example of a synthetic complex possessing a $[Fe^{IV}_2(u\text{-}O)_2]$ core structure.[78] Analysis of Mössbauser and EXAFS spectroscopic data revealed that this complex contains two IS Fe^{IV} centers that are antiferromagnetically coupled and exhibits Fe–O and Fe···Fe distances of 1.78 and 2.73 Å, respectively.

1.1.3 C-H bond activations

The reactivity of high-valent iron(IV)-oxo complexes in C–H hydroxylation also has been investigated in depth by theoretical and experimental methods. The central focus of active research has been directed toward understanding the nature of these high-valent-

metal intermediates and how they react with C–H. So far, all the studies have led to some significant progress on many aspects of iron(IV)-oxo mediated C–H oxidation.

1.1.3.1 Reaction mechanism

The mechanism of high-valent iron(IV)-oxo mediated C–H bond hydroxylation has been a subject of intense studies; however, the mechanistic features remain disputed and raise questions. The consensus mechanisms for both heme and non-heme iron(IV)-oxo complexes are the "rebound mechanism" which was first proposed in 1978 in a short communication by Groves, McClusky, White, and Coon.[79] In this mechanism, the ferryl oxygen initially abstracts a hydrogen from the substrate, leaving a carbon radical on the substrate, which in turn recombines with the equivalent of a hydroxyl radical coordinated to the iron atom (Figure 1.8). All theoretical studies indicated that the initial H-atom abstraction from the substrate is the rate-determining step of the process.

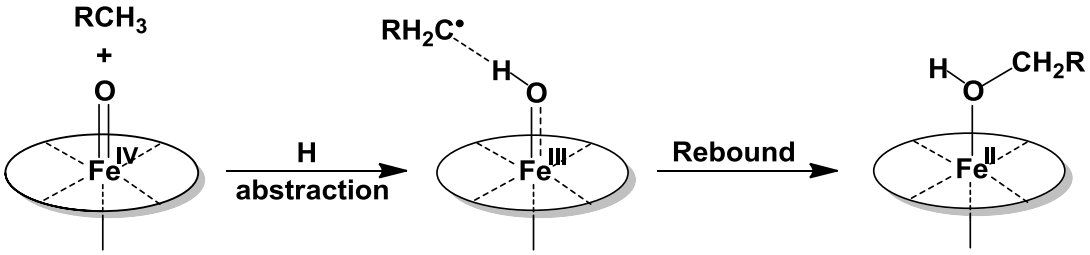

Figure 1. 8 The proposed rebound mechanism for C–H bond hydroxylation.

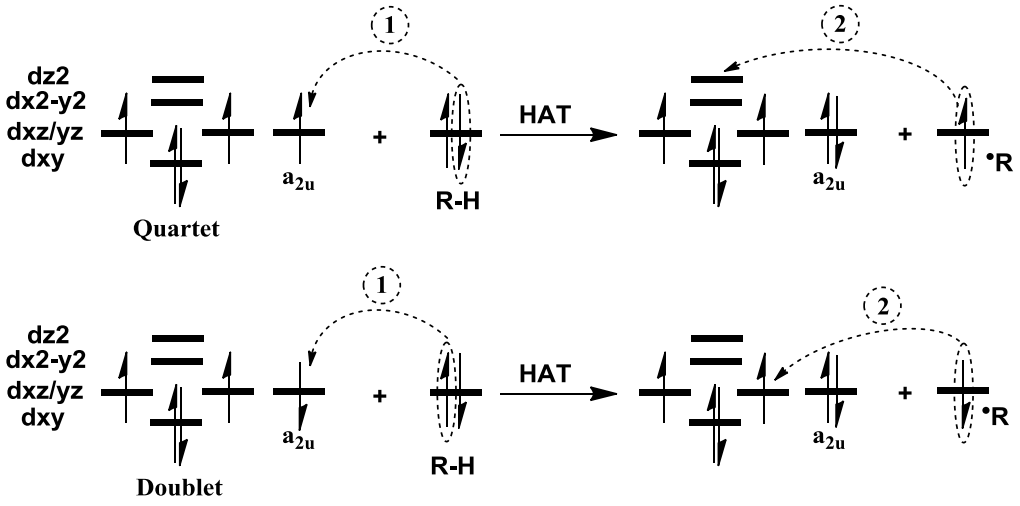

Figure 1. 9 Schematic summary of the electronic changes along the reaction pathway in the heme-base iron(IV)-oxo catalysts.

In heme-based catalysts, the d^4 configuration ($\delta^2\pi^{*1}\pi^{*1}$) of the iron center can either ferromagnetically or antiferromagneically couple to the unparied electron of porphyrin π-radical (a_{2u}^1), leading to two low-lying spin state: quartet (S = 3/2) and doublet (S = 1/2),

labeled as $^{4,2}A_{2u}$. Figure 1.9 shows the orbital evolution diagram for C–H bond hydroxylation by these two spin states. In the course of H-abstraction, an β or α electron shifts from the σ_{CH} orbital to the singly occupied a_{2u} orbital in quartet and doublet states, respectively, leading to intermediates $^{4,2}I_{rad}$(IV) with Fe^{IV} centers that are antiferromagnetically or ferromagnetically coupled to the substrate radical φ_C. In the rebound steps, the electron will shift from φ_C to the heme to form the ferric-alcohol complex [^{4,2}P(III)]. In the case of $^{2}I_{rad}$(IV), the bound process involves transferring the electron in φ_C to the low-lying π^*_{XZ}(FeO) orbital and thereby is nearly barrier-free. Whereas for the rebound step of $^{4}I_{rad}$(IV), the electron has to be shifted into the higher-lying σ^*_{Z2} orbital thus leading to a significant rebound barrier.[80]

There are two additional layers of complexity for C–H bond activation by mononuclear non-heme iron(IV)-oxo complexes. First, the non-heme iron(IV)-oxo complexes are known to have either triplet or quintet ground spin states. Therefore, they have different d-electron occupation in the iron centers and several of the semi-occupied or unoccupied iron-based molecular orbitals could serve as electron acceptors. The second layer of complexity stems from the geometry of the substrate approach. The cleaving C–H bond may attack the iron(IV)-oxo unit either from the top or from an equatorial position. Both types of reaction geometries lead to different electronic structures in transition states and hence to different reaction pathways. Figure 1.10 shows the orbital occupancy evolution diagram for the well-established reaction pathways in C–H bond hydroxylation by non-heme iron(IV)-oxo complexes. In the triplet channel, the electron of the substrate is transferred into the π*(FeO) antibonding orbital (π-mechanism). To accomplish the maximum orbital overlap between the electron-donor and –acceptor orbitals, the substrate may take a horizontal approach to the iron(IV)-oxo reactive center. Finally, the offset between the orbital overlap and the Pauli repulsion leads to the transition states $^{3}TS_{H\pi}$ characteristic of a bent Fe-O-H angle. In the quintet state pathway, the electron of the substrate is shifted to the σ*(FeO) orbital (σ-mechanism). The upwards pointing lobe of the Op_z orbital requires a vertical approach of the substrate; hence, $^{5}TS_{H\sigma}$ features a nearly collinear Fe-O-H-C arrangement. In the rebound step, the formation of the C–O bond is accompanied by a simultaneous electron transfer from the substrate into the Fe d_{z2} and $Fe_{dxz/yz}$ orbitals, respectively. Thus, the rebound step appears to follow a σ-mechanism on the triplet state surface and a π-mechanism on the quintet state surface.

So far, all the theoretical studies have led to the common conclusion that the quintet ferryl species are aggressive oxidants than the corresponding triplet counterparts, the analysis of the electronic structure changes along the reaction coordinate revealed that increased Pauli repulsion and attenuated orbital interaction increase the barriers for the triplet π-pathway.[5,81-85] Direct experimental evidence for the higher reactivity of the *S* = 2 state is lacking in the literature. Presumably, because the majority of model complexes prefer the triplet ground states and the few recently reported *S* = 2 complexes are

sterically bulky, their reactivities toward C–H bond cleavage are only comparable with triplet ferryl analogous.[51,73,74,76]

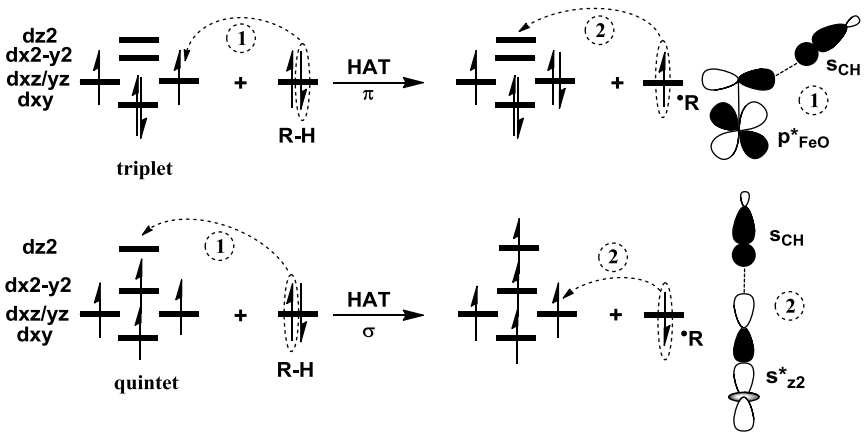

Figure 1. 10 Schematic summary of the electronic structure changes along the reaction pathway in the triplet and quintet state of mononuclear non-heme iron(IV)-oxo complexes.

Due to the lack of the exact structure of the active site of intermediate Q, different computational models have been proposed in order to study the mechanism of methane hydroxylation by sMMO.[86-88] Four different models were proposed by the research group of Yoshizawa,[88-90] Morocuma–Basch,[91] Siegbahn,[92-94] and Friesner–Lippard.[86,95-97] These models differ in their size, spin state, charge, and Fe coordination number. Mechanistically, they fall into two distinctively different classes. The first class was proposed by Yoshizawa and Hoffmann based on the reaction mechanism of C–H bond activation by bare metal-oxo $[FeO]^+$ species.[98-101] It is called as the noradical mechanism with the salient feature of formation a Fe-C bond in the catalytic cycle (Figure 1.11). This mechanism implies that the metal is an actor in the C–H bond activation. The second reaction mechanism is called as the radical oxygen rebound mechanism, which is the same as the "rebound mechanism" established in mononuclear heme and non-heme iron(IV)-oxo complexes (Figure 1.12). The Morocuma–Basch, Siegbahn, and Friesner–Lippard models all follow this mechanism. Unlike the Yoshizawa model, in this reaction mechanism C–H bond activation takes place at the one of the bridging oxo group. The initial oxidative C–H bond activation is the rate-limiting step, which involves the first electron transfer to one iron center. The reaction proceeds by the attack of the substrate radical at the newly formed bridging hydroxide group and finally leads to the reduction of the second iron center.

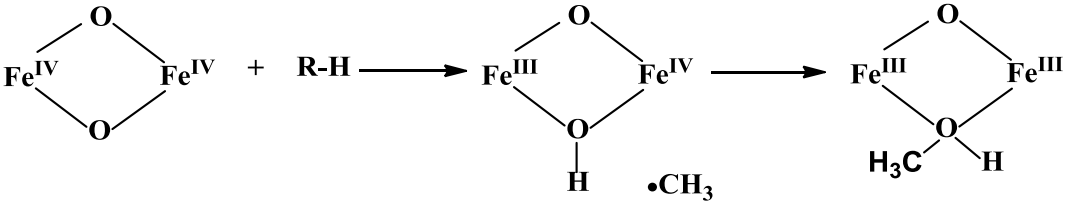

Figure 1. 11 Rebound mechanism for the hydroxylation of substrate by sMMO.

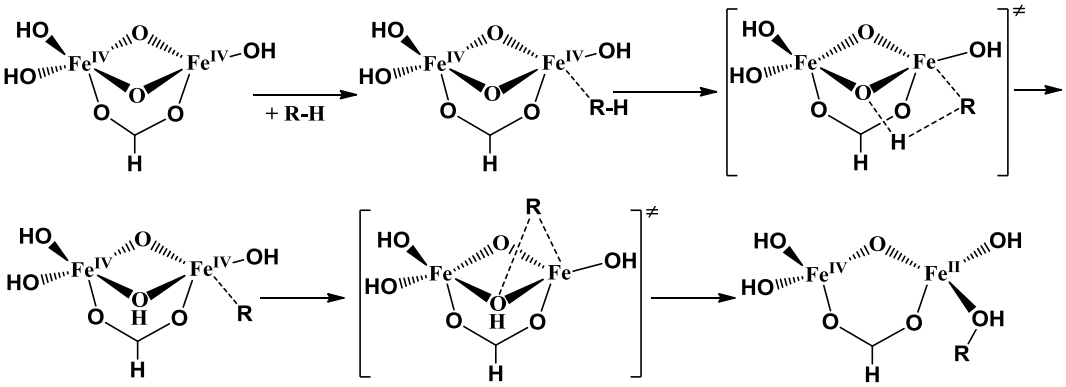

Figure 1. 12 Noradical mechanism proposed in the Yoshizawa model of sMMO.

1.1.3.2 TSR/MSR scenarios

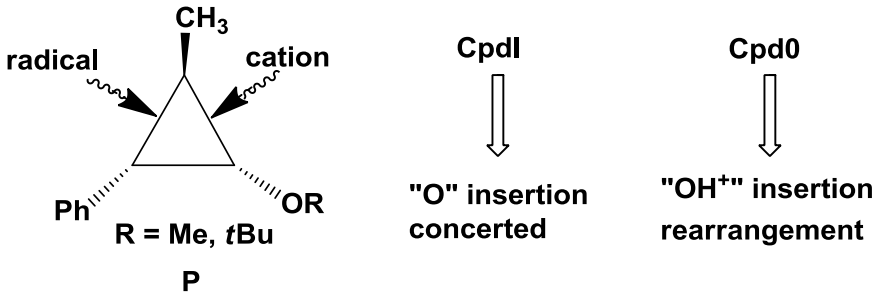

Figure 1. 13 The two-oxidant hypothesis using CpdI and Cpd0, and a probe substrate (P) that can open differently depending on whether it leads to radical or a cationic intermediate.[102]

The support for the consensus rebound mechanism are mainly from the findings of rearranged alcohol products which indicate the presence of a free radical with a finite lifetime[103] and the kinetic isotope effect (KIE) measurements of Dinnocenzo, Jones et al.[104] The picture started to cloud, however, when radical clocks were used to gauge the rate of the rebound step.[13] Several studies by Newcomb and co-workers, designed to probe the radical using alkane substrates that would yield ultrafast radical clocks, do not concur with a free-radical intermediacy.[102,105] For example, some rearrangement patterns of clocks like **P**, depicted in Figure 1.13, were shown to correspond to carbocationic species.[105-108] Subtraction of the rearranged products from the overall product mixture results in

lifetimes as short as 70 fs;[105,106] apparent lifetimes are too fast to correspond to a real free-radical intermediate. These unrealistic lifetimes and the rearranged products derived from carbocations have led Newcomb and co-workers to propose a "two-oxidant hypotheses" as an alternative mechanism and suggest that the radical intermediate is not present during the reactions (Figure 13).[102]

Newcomb's work has cast the rebound mechanism into doubt, and the mechanistic dilemma posed by the reactivity patterns is perhaps too subtle for current experimental means to be resolved. An eventual resolution of this controversy will no doubt come from the interplay of the theory and experiment. In this sense, the two-state reactivity (TSR) and multistate reactivity (MRS) concepts have emerged in response to intriguing experimental data.[10,109-113] The fundamental feature of the TSR/MSR scenario is that the reaction proceed at least on two potential energy surfaces with different spin multiplicities that either cross or remain in proximity, whereby different states coproduce different reaction intermediates and products in a given process. Figure 1.14 shows a typical TSR/MSR scenario, with C–H activation and rebound in the reaction of cyclohexane hydroxylation by $[(N4Py)Fe^{IV}O]^{2+}$. It is seen that the quintet state cuts below the barrier of the triplet ground state and hence predominantly mediates the transformation.[114] This scenario paradigm provides a satisfactory rational for the controversial findings in the field. Till now, this TSR/MSR scenario has been extensively performed by Shaik, Jerusalem, and Yoshizawa et. al.[80,114-117]

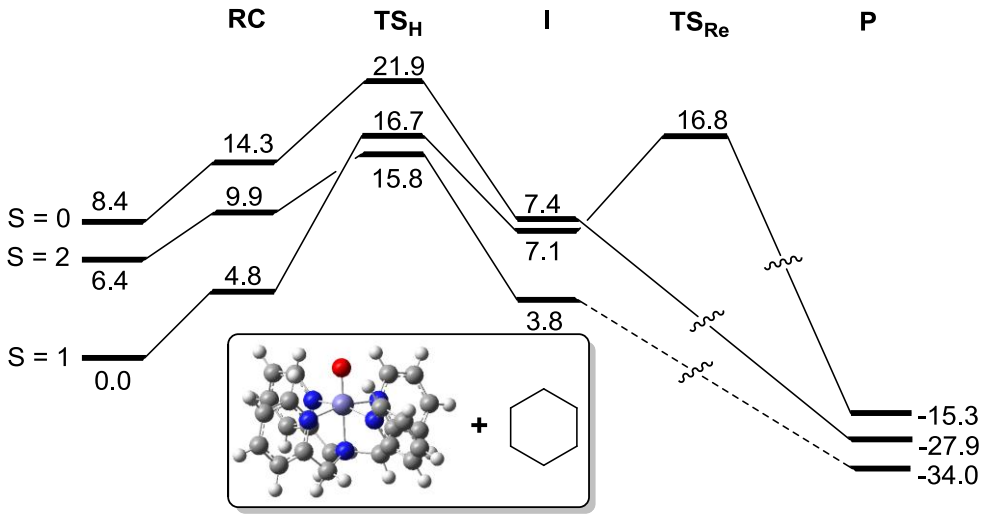

Figure 1. 14 B3LYP/LACV3P++//LACVP-calculated TSR/MSR scenario during hydroxylation of cyclohexane by $[(N4Py)Fe^{IV}O]^{2+}$.[114]**

1.1.3.3 Axial ligand effects

One of the central focuses of current active research is to determine the role of the axial ligand in the reactivity of iron(IV)-oxo species.[45,118-122] For many years, it has been believed

that the nature of the axial ligand is one of the predominant determinants of the chemistry performed by high-valent intermediates. This important hypothesis originally arises from the different catalytic ability of heme oxygen activating enzymes. P450s are known as powerful oxidants toward specific functionalization of unactivated hydrocarbons, while the peroxidases, such as horseradish peroxidase (HRP), are only function as one-electron oxidants. They cannot readily perform the demanding two-electron oxidations or oxygen-transfer reactions observed for P450s. The difference in the axial ligands between the P450s and other oxygen activating enzymes has been proposed to be the reason for their differences in catalytic function. The cysteinate ligand in P450s creates a "push-effect" and donates electron density to the heme iron center, while the histidine axial ligand in peroxidases withdraws electrons, thus resulting in a pull effect. This difference in push/pull effect of the axial ligand changes the central properties of the heme-iron unit and results in functional differences. Indeed, Gross et al.[52,123,124] and Nam et al.[45,55,65,125,126] have unambiguously identified the axial ligand effect on the substrate oxidation by a series of iron(IV)-oxo oxidants with variable axial ligands. These studies used biomimetic iron(IV)-oxo oxidants where the ligand trans to the oxo group was occupied by either an anion, e.g., F^-, Cl^-, acetate, perchlorate, etc, or a neutral solvent molecule, e.g., acetonitrile. Rate constants for styrene expoxidation and hydrogen abstraction reactions were measured and shown to vary with the nature of the axial ligand.

Understanding the role of axial ligand is therefore very important. Green et al. have undertaken a systematic study of the high-valent form of P450s by using a variety of spectroscopic techniques. The results pointed out that all thiolate-ligated heme proteins have much higher enhanced basicity of the ferryl in the compound II intermediate and it would therefore confer to the preceding compound I greater C–H-activating potency or, alternatively, equivalent potency at diminished potential.[122] This results lead to the conclusion that the redox potential is not the only parameter that needs to be considered for C-H bond oxidation. Mayer has elegantly used thermodynamic cycles to evaluate the ability metal-oxo complexes to cleave C-H bonds.[127,128] Building on the pioneering work of Polanyi[129-132] and Bordwell[133], Mayer's approach demonstrates a direct thermodynamic connection of the O–H bond dissociation energies (BDE_{OH}) for the metal-hydroxo (MOH) complexes formed after the initial cleavage event with the strength of the cleaving C-H bond: the energy require for hemolytic C–H bond cleavage must comparable to that produced in forming the MO–H bond.[128,134]

A thermodynamic cycle for such an analysis is shown in Figure 1.15a, from which one can derive an equation: $BDE_{OH} = 23.06\ E^\circ + 1.37\ pK_a + C$.[133] C is a constant that corrects for the properties of the hydrogen atom in solution and depends on solvent and the redox potential reference. From this equation, one can see that the critical feature of this

analysis is the inclusion of the pK_a values for the metal-hydroxo species, the conjugate acid of the metal-oxo unit, and thus a gauge of the basicity of the oxo ligand. Furthermore, this analysis shows that the basicity of the oxo ligand affects the reactivity of metal-oxo complexes and provides another tunable parameter that can influence the efficacy of C–H bond cleavage. The importance of this effect is illustrated graphically in Figure 1.15b for the cleavage of a C–H bond in methane. Note that at low pK_a values the redox potentials required are prohibitory to maintain the function. However, as the basicity of the oxo ligand increases there is a decrease in the required redox potential for C–H bond oxidation.

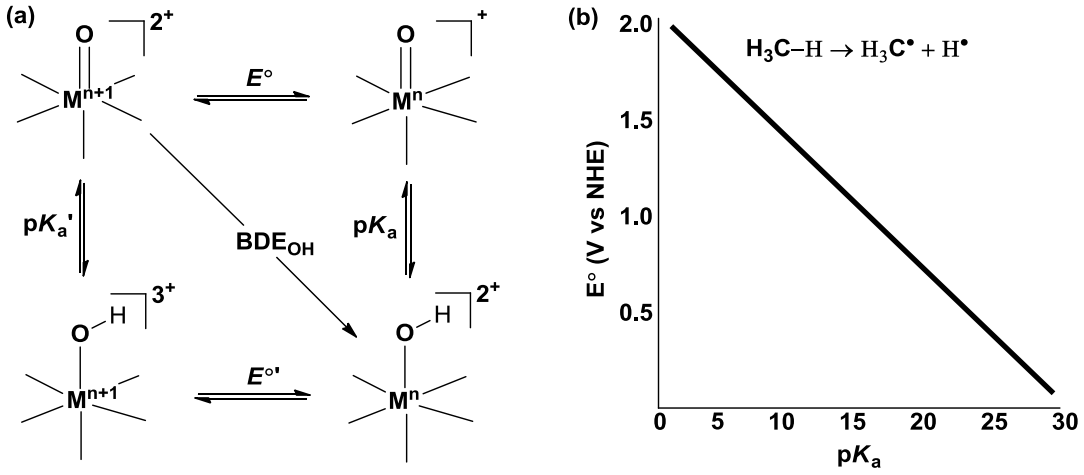

Figure 1. 15 Thermodynamic cycle describing the BDE_{OH} (a), and the relationship between redox potential and pK_a for a metal-oxo species in the cleavage of a C–H bond in methane (b).

In summary, advances in understanding key factors that dictate the reactivity of metal-oxo species towards C–H bond clevage have been achieved through the extensive studies of the tuning effect of the axial ligand.[3,119,134,135] Within a thermodynamic framework that relies on the interplay between basicity and redox potential, axial ligands control these basic properties in proteins and are now being used in synthetic systems to discover new catalysts.

1.2 Nitrido complexes

Iron-nitrido complexes, which are isoelectronic to iron-oxo species, are also considered as key intermediates in a number of important biological transformations.[136-138] However, while a number of transient high-valent iron-oxo intermediates in the catalytic cycle of heme and non-heme enzyes have been identified and spectroscopically characterized,[8,21,22,34,35,48-50,139] direct evidence for the involvement of iron-nitrido intermediates in biology is lacking. To probe the possibility of the involvement of iron-nitrido intermediates in biological dinitrogen-reduction and atom-transfer reactions,

bioinorganic chemists became interested in the synthesis and reactivity studies of model compounds involving high-valent metal-nitrido moieties. Till now, the synthetic iron–nitrido complexes have iron oxidation state ranging from +4 to +6.[140-149] Here we briefly summarized the recent advances in this field.

All reported terminal iron(IV)-nitrido complexes possess the distorted trigonal pyramidal coordination geometry, and two isolable iron(IV) nitrido complexes have been crystallographically characterized recently.[140,142,143,150] The first terminal Fe^{IV}≡N complex was synthesized by Betley and Peter in 2004.[140] By using phenyl-*tris*-diisopropylphosphinoborate ($PhBP^{iPr}_3^-$) as the stabilizing tripodal chelating ligand and lithium amide 2,3,5,6-dibenzo-7-azabicyclo[2.2.1]hepta-2,5-diene (dbabh) as the N-atom transfer reagent, the four-coordinate [($PhBP^{iPr}_3^-$)Fe^{IV}(N)] could be obtained and thoroughly characterized by various spectroscopic techniques. The first crystallographically characterized Fe^{IV}≡N complex was accomplished in 2008. Photolysis of an N-anchored tris(carbine)-ligated azide complex [($TIMEN^{mes}$)$Fe^{II}(N_3)$]$^+$ ($TIMEN^{mes}$ = tris[2-(3-mesityimidazol-2-ylidene)ethyl]amine) yield the four-coordinate tetravalent [($TIMEN^{mes}$)Fe^{IV}(N)]$^+$.[142] Later, Specpaniak et al. reported the second crystallographically characterized Fe^{IV}≡N complex [($PhB(^tBuIm)_3$)Fe^{IV}(N)] ($PhB(^tBuIm)_3$ = phenyl-*tris*(1-*tert*-butylimidazol-2-ylidene)borate) by combining the ligand systems of Vogel et al. and that of Betley and Peter.[143] The characterization of iron(V)-nitrido complexes started from the resonance Raman detection of [Fe^{V}(N)(TPP)]$^-$ (TPP^{2-} = tetraphenylporphinate(2-)) complex by Nakamato and coworkers.[151] More recently, the photolysis of [(cyclam–ac)$Fe(N_3)$]$^+$ (cyclam–ac$^-$ = 1,4,8,11–tetraazacyclitetradecane–1–acetate) leading to the desired [(cyclam–ac)Fe^{V}(N)]$^+$ species was reported.[53] Later, the detailed geometric and electronic structure analysis using a combined spectroscopic and theoretical approach revealed the complex has a doublet ground state.[148] Very recently, Meyer and Smith reported the synthesis of a four–coordinated iron(V)-nitrido complex supported by a tripodal N–heterocyclic carbine ligand, which also feature a LS (S = 1/2) ground state.[144] When it comes to the iron(VI)-nitrido complex, Wieghardt and coworkers reported the second Fe(VI) compound (the first one is $[Fe^{VI}O_4]^{2+}$) generated by photolysis of a stable iron(IV) azido compound, [(Me_3–cyclam–ac)$Fe^{IV}(N_3)$]$^{2+}$.[149] This is the first hexavalent iron compound to be synthesized in laboratory. The reactivity of the synthetic iron-nitrido complexes with various oxidation states have also been investigated in depth experimentally; interestingly, most of the reactions exhibited to be non-catalytic, with the reactivity falling far short of that of iron–oxo complexes.[142-144]

1.3 The aim of current thesis

The first part of the present PhD thesis is concerned with the reaction mechanism of alkane hydroxylation by model iron(IV)-oxo complexes $[Fe(O)(NH_3)_5]^{2+}$, $[Fe(O)(NH_3)_4(OH)]^+$, and $[Fe(O)(NH_3)_3(OH)_2]$. By exploring all the possible pathways in C–H bond hydroxylation,

the energetic feasible quintet π-channel provides a new element of specificity control in C–H bond activation by iron(IV)-oxo species. The choice of σ- or π-pathways could be controlled – at least in part – by steric hindrance in model systems or by the restrictions of the protein pocket in metalloenzymes.

The second part of the thesis is focus on the reactivities of high-valent iron–oxo and –nitrido complexes with the iron oxidation state ranging from IV to VI. All the calculations were performed on model complexes in which the iron centers is coordinated in a distorted octahedral arrangement with ammonia acting as the equatorial ligand, and hydroxyl group as the axial ligand tran to the oxo or nitrido group. The nearly identical coordination environment of all the complexes allows us to make more generalized comments about structural and electronic properties, relative reactivities of high-valent iron–oxo and –nitrido species. Clarifying the difference in the redox reactivity between the iron–oxo and –nitrido moieties in the nearly identical structures and oxidation states, that is, $Fe^{n+}O$ and $Fe^{n+}N$, contributes to a basis for enhanced understanding of nature's redox enzymes and the matching catalyst systems to target oxidation processes.

The third part of the thesis deals with the reactivities of four close related diiron complexes. These four complexes can convert with each other but differ by charge, spin state and core geometry structure. Clarifying the difference in reactivity of these complexes will provide a comprehensive theoretical framework in which the preference of the terminal Fe=O unit and HS state of iron(IV) center in C–H bond activation can be understood.

The forth part of the thesis is a cooperation work with experiment. In this study, we well rationalized the relative higher oxidative power of the fluoride substituted complex **1-F**$_{trans}$ $(F–Fe^{III}–O–Fe^{IV}=O)^{2+}$ compared to its precursor **1-OH**$_{cis}$ $(OH–Fe^{III}–O–Fe^{IV}=O)^{2+}$. Our calculations revealed that the hydrogen bond between the oxo and hydroxo group in **1-OH**$_{cis}$ does not significantly change the electrophilicity of the reactive Fe^{IV}=O unit. However, during the reaction of C-H bond oxidation, this hydrogen bond has to be partially broken. This leads to the slightly higher barrier for **1-OH**$_{cis}$ relative to **1-F**$_{trans}$, which has similar open-core structure but no hydrogen bond.

2. Theoretical Background and Methods

2.1 Elementary quantum chemistry

Quantum chemistry is a branch of chemistry whose primary focus is the application of Quantum Mechanics (QM) to solve chemical problems. QM is centered on the Schrödinger equation, which exists in time-dependent and time-independent form. In the present thesis, ground state chemical reactions have been studied. In this case it is sufficient to use the time-independent form of the Schrödinger equation ($\hat{H}\Psi = E\Psi$) as a starting point. However, only for one-electron systems the equations can be solved exactly, the interactions of a many-body system are too complicated to be solved. Hence approximations are necessary. The first approximation is the so-called Born-Oppenheimer approximation that based upon the large difference in the mass between nuclei and electrons. It assumes that in a molecule electrons move in a static nuclear framework and the electron can thereby be approximated to move in a field of fixed nuclei. Therefore, the kinetic energy of the nuclei can then be neglected, and the nuclei-nuclei repulsion will be constant for a fixed geometry. The electronic energy is obtained for a frozen conformation of the nuclei. By calculating the electronic energy for different nuclear arrangements a potential energy surface can be obtained, which defines the equilibrium conformations of a molecule. The notion of potential energy surface is meaningful only under the validity of the Born-Oppenheimer approximation.

Unfortunately, the Born-Oppenheimer approximation is not enough to solve the electronic Schrödinger equation for a many-body system. Further approximations for wave functions are needed. The basic wave function method is called the Hartree–Fock (HF) method, which is based on the independent–particle model or molecular orbital (MO) model. There are certain conditions, which the wave function must satisfy in order to describe some peculiar properties of the electrons. Each electron is associated with a one-electron wave function, which is the product of a spatial function that depends on the coordinate of the electron and a spin function that depends on its spin (the one-electron wave functions are called spin orbitals). The molecular orbitals in a molecule are usually constructed as a linear combination of the atomic orbitals of the corresponding atoms (LCAO, Linear Combination of Atomic Orbitals). In order to satisfy the antisymmetry principle, which also fulfills the Pauli Principle, the solution of the Schrödinger equation is obtained by constructing the wave function as a Slater determinant. Each column in the Slater determinant contains a spin orbital and the rows are labeled by the electron coordinates. If two electrons occupy the same spin–orbital, two rows in the determinant become equal, i.e. the determinant will vanish (Pauli Exclusion Principle). An interchange

of two rows, which corresponds to interchange the coordinates of two electrons, changes the sign of the determinantal wave function, thus satisfying the requirement of antisymmetry. After having selected the form of the wave function, the variational principle provides a method to numerically solve the Schrödinger equation. The expectation value of the energy is minimized with respect to some parameters of the trial wave function and by imposing the appropriate normalization condition.

However, a major limit of HF method is that it treats each electron in an average field due to the repulsion from all other electrons, instead of the explicit electron-electron interaction. In other words HF method lacks a certain part of the electronic energy, referred to as correlation energy. Although the correlation energy represent a quite small percentage of the total energy, it is rather essential for solving chemical problems and the evaluation of relative energies.

To improve the accuracy beyond the HF method, explicit correlation between electrons has to be included. Many highly correctly wave function based approaches have been developed in order to take into account the correlation energy explicitly. Some of them, like the Møller–Plesset perturbation methods (e.g. MP2 and MP4), configuration interaction method (e.g. CISD) and coupled cluster methods (e.g. CCSD(T)), achieve this goal by including more determinants in the wave function. The wave function thus becomes more flexible allowing the electrons to correlate their movement in different orbitals. However, all the methods mentioned above are built upon the single determinant HF method. Thus, when a single determinant is a bad initial approximation, this problem will be "inherited" to the wave function even including correlation. This occurs when a system is of multiconfigurational character (near degeneracy). In these cases the multiconfigurational self–consistent field (MCSCF) and the complete active space (CASSCF) methods, are better starting points. These methods add more determinants and optimize both their orbitals and coefficients. NEVPT2 is a multireference method using additionally perturbation theory, which will improve the results more significantly.

The accuracy of the calculations with the methods listed above is improved significantly compared to HF; however, the computational costs are also extremely increased. Thus, only small systems can be treated. For large systems, as in the present thesis, alternative methods have to be used.

2.2 Density functional theory

From the first attempts to use the electron density instead of the wave function dates back to the 1930s and the breakthrough paper of Hohenberg and Kohn in the 1960s showed that the ground-state energy and other properties of a system were uniquely defined by the electron density.[152,153] The development of DFT methods opened up a new

era where relatively large systems, containing transition metals as well, could be investigated quantum mechanically.[154]

The foundation which DFT is built upon is the Hohenberg–Kohn theorem, which shows that the total energy is a unique functional of the electron density of the system, $E[\rho]$, and the determination of the complicated many–electron wave function is not needed. In other words, the fundamental problem in DFT is that the exact form of the functional connecting the energy with a given electron density is not known. The energy functional can be written as a sum of terms from the kinetic energy $T[\rho]$, electron–electron repulsion $E_{ee}[\rho]$, and nuclei and electrons interaction $E_{ne}[\rho]$:

$$E[\rho] = T[\rho] + E_{ee}[\rho] + E_{ne}[\rho] \qquad (2.1)$$

Kohn and Sham introduced the mathematical framework for the numerical determination of the electronic ground state of many–electron systems.[155] The non–interacting one electron orbitals, called Kohn-Sham (KS) orbitals (ϕ_i), make it possible to express the electron density as the sum of the squared orbitals. Thus, it means that the real system of interacting electrons is formally described through a fictitious system of non-interacting particles. In this formulation large part of eq. 2.1 can be written as:

$$E[\rho] = Ts[\rho] + J[\rho] + Ene[\rho] + Exc[\rho] \qquad (2.2)$$

Where $T_s[\rho]$ is the kinetic energy of non-interacting particles; $J[\rho]$ and $E_{ne}[\rho]$ are the classical electron–electron and electron–nuclei Coulomb interactions, respectively; and finally $E_{xc}[\rho]$ is the exchange–correlation energy containing the corrections to the non–interacting approximation. Minimizing the total energy of a determinant constructed by Kohn–Sham orbitals with respect to their shape is similar to the HF approach, and the Kohn–Sham eigenvalue equation can be written as follows:

$$\hat{h}_{ks}\phi_i(r) = \varepsilon_i\phi_i(r) \qquad (2.3)$$

where $\hat{h}_{ks}$ is the one-electron operator given in eq. 1.4, with the analytical expression for $T_s[\rho]$ and $J[\rho]$.

$$\hat{h}_{ks} = -\frac{1}{2}\boldsymbol{\nabla^2} + \boldsymbol{V_{ne}} + \int \frac{\boldsymbol{\rho(r')}}{|\boldsymbol{r}-\boldsymbol{r'}|}\boldsymbol{dr'} + \frac{\boldsymbol{\partial E_{xc}[\rho]}}{\boldsymbol{\partial \rho(r)}} \qquad (2.4)$$

If the exact form of E_{xc} was known, the exact total energy including correlation would be obtained. Thus, the accuracy of a DFT method depends on how well the exchange–correlation functional can be approximated.

Several classes of density functionals can be marked out. The simplest one is known as Local Density Approxiamtion (LDA) and Local Spin Density Approximation (LSDA) for open–shell systems. It assumed that exchange term can be formulated analytically for a uniform electron gas, but the correlation term is only estimated.[156,157] LSDA methods are capable to provide results with accuracy of HF. The further step inclusion of not only the density but also its gradient $\nabla\rho$ gives the so-called Generalized Gradient Approximation (GGA). Among the most prominent GGA functionals are the Perdew's BP86,[158] the LYP function by Lee, Yang and Parr,[159] and BLYP developed by Becke (exchange part) and Lee, Yang and Parr (correlation part). The GGA approximation describes chemical bonding markedly better than LSDA, with the accuracy similar to MP2.[160] Finally, the best methods of modern DFT are of hybrid functionals, which combine functionals of LSDA, corrections from GGA, and also a fraction of Hartree–Fork exchange $\boldsymbol{E_x^{HF}}$, calculated via KS orbitals. The dominating hybrid functional is the B3LYP functional, which has been used in the present thesis. In B3LYP the exchange–correlation functional is a linear combination of local and gradient corrected exchange and correlation and HF exchange, using a few empirical parameters.[161] The B3YLP functional can be written:

$$\boldsymbol{E_{xc}^{B3LYP}} = (\mathbf{1}-\boldsymbol{A})\boldsymbol{E_x^{Slater}} + \boldsymbol{AE_x^{HF}} + \boldsymbol{BE_x^{Becke}} + \boldsymbol{CE_c^{LYP}} + (\mathbf{1}-\boldsymbol{C})\boldsymbol{E_c^{VWN}} \qquad \textbf{(2.5)}$$

Where E_x^{Slater} is the Dirac-Slater exchange, E_x^{HF} is the Hartree-Fock exchange term, E_x^{Becke} is the gradient part of the exchange functional of Becke,[162] E_c^{LYP} is the correlation functional constructed by Lee, Yang and Parr[159] and E_c^{VWN} is the correlation functional by Vosko, Wilk and Nusair.[157] The parameters A, B and C are determinated empirically by Becke[163] by fitting them to thermochemical data, using the PW91 functional instead of the gradient part of LYP correlation functional.[164] Recently, a new family of "double-hybrid" density functionals was proposed that employs the occupied and virtual KS orbitals in second-order many-bondy theory to replace a fraction of the semi-local GGA correlation.[165] Unlike traditional KS-DFT approaches, double-hybrid DFT can perform well in both noncovalent and covalent systems. It has been well tested that the first double-hybrid functional B2-PLYP yielded high accuracy in thermochemistry as well as in the prediction of molecular structure.[165-170]

2.3 Reaction mechanism

A chemical reaction is the rearrangement of the pattern of the atomic nuclei relative to each other.[171] A reaction mechanism is an exact step-by-step description of what occurs molecularly in a given chemical reaction. Each step of the reaction mechanism is known as an elementary process, a term used to describe a moment in the reaction where one or more molecules changes geometry or is perturbed by the addition or omission of another interaction molecule. So collectively, an overall reaction and a reaction mechanism, is

usually made up of multiple elementary processes. These elementary steps are the basic building blocks of a complex reaction and cannot be broken down any further.

Because a reaction mechanism is used to describe in detail exactly what takes place at each stage of an overall chemical reaction, it also describe the reactive intermediates, and transition states. A reaction intermediate is any stable geometry configuration (i.e., that exists at a minimum of the energy) occurring during a reaction and having a lifetime longer than the period of typical molecular vibrations (on the order of $10^{-13} - 10^{-14}$). They are often free radicals or ions. Transition states (**TS**) are commonly molecular entities involving an unstable number of bonds and/or unstable geometry. They correspond to maxima on the reaction coordinate, and to saddle points on the potential energy surface (PES) for the reaction.

A complete reaction mechanism must also describe the relative rates of the reaction steps. The equation of an elementary reaction defines its corresponding rate, which at constant temperature is proportional to the products of the concentrations of the reactants. Therefore for the elementary reaction:

$aA + bB \rightarrow$ Products (2.6)

the corresponding rate equation is :

$$\frac{-d[A]}{dt} = k[A]^a[B]^b \qquad (2.7)$$

where the coefficient *k* is called the rate constant and is independent on the concentrations (and dependent on the temperature). A differential rate equation depending on concentrations and microscopic rate constants can be associated with a chemical reaction once its reaction mechanism (i.e., the sequence of elementary reactions) has been defined. To know the reaction mechanism is essential to understand which factors govern the rate of a reaction.

2.4 Transition State Theory

The subject of investigation presented in this thesis is enzymatic chemical reactions in which the reactants are transformed into products. The main approach in the theoretical study of catalyzed reaction mechanisms is to calculate the PES along the reaction coordinate, which involves locating and characterizing the minima and transition states and their relative energies. In particular, the ability to model transition states is crucial for estimating activation barriers ($\Delta G^{\ddagger}$), which is defined as the difference in the free energies of the reactant and transition state.

Transition State Theory (TST) makes the connection between the calculated data (free energy barriers) and the reaction rates, which come out form experimentally measurements. Let us consider now a bimolecular reaction with **R** (reactants **A** and **B)** and **P** (products **C**) (Figure 2.1):

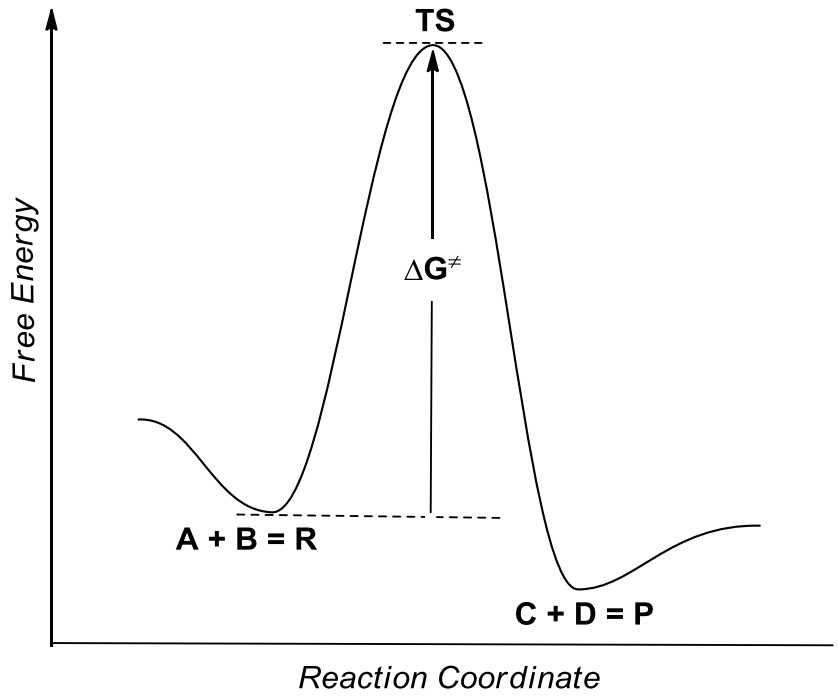

Figure 2. 1 The chart showing the PES of an elementary single-step bimolecule reaction.

$$\mathbf{A} + \mathbf{B} \rightleftharpoons \mathbf{R} \overset{K^{\neq}}{\leftrightarrow} \mathbf{TS} \overset{k'}{\rightarrow} \mathbf{P} \rightleftharpoons \boldsymbol{C} + \boldsymbol{D} \quad (2.8)$$

where the equilibrium constants $K^{\neq}$ is introduced as

$$\boldsymbol{K^{\neq}} = \frac{[\mathbf{TS}]}{[\mathbf{R}]} \quad (2.9)$$

and concentration of respective species are given in square brackets. Though **TS** occurs at an energy maximum, TST assumes that the molecular system at the transition point is in rapid equilibrium with the reactants, as reflected in eq. (2.9). This permits to introduce the free energy equilibrium constant $K^{\neq}$, following from the Maxwell-Boltzmann statistics:

$$\boldsymbol{K^{\neq}} = \boldsymbol{e^{-\Delta G^{\neq}/RT}} \quad (2.10)$$

where $\Delta G^{\neq}$ is the Gibbs free energy difference between TS and R, T is the absolute temperature, and R is the gas constant. Another important assumption of the TST states that the rate of reaction is directly proportional to the concentration [TS] of the activated complex. Since [TS] is small, its decomposition is the rate-determining process of reaction.

The first-order rate constant *k*' in eq. (1.8) is thus related to the decomposition of TS to P as follows:

$$\frac{d[P]}{dt} = k[R] = k'[TS] \quad (2.11)$$

where *k* is the first-order rate constant for reactants R procession. Evaluation of *k*' is based on a proposal by Eyring that activated complex breakdown occurs during its first vibrational excursion:

$$k' = \kappa\nu \quad (2.12)$$

where *v* is the vibrational frequency of the bond to be broken and κ, the transmission coefficient, is the probability that the immediate breakdown of TS will end in product P formation. The κ factor rarely falls outside the range 0.5-2.0 and accounts for re-crossing (when a molecular passes over the TS but is reflected back to the reactant R side, $\kappa < 1$), tunneling (when a system penetrates through the barrier from the side of R-valley on PES and appears on the P-valley side, $\kappa > 1$) and deviation from equilibrium (Blotzmann) distribution in eq.(2.10). The *v* value can be determined from Plcank's law:

$$\nu = \frac{k_B T}{h} \quad (2.13)$$

where k_B and *h* are the Boltzmann and Planck's constants, respectively. Then combines eqs.(2.10) through (2.13) yields the final expression for the rate constant *k* in the form of Arrhenius equation:

$$k = \kappa \frac{k_B T}{h} e^{-\Delta G^{\neq}/RT} \quad (2.14)$$

Examination of the eq.(2.4) formula shows that an increase of $\Delta G^{\neq}$ by 1.36 kcal/mol only leads to the reaction ten times slower (*k*/10) at the normal temperature *T* = 298.15*K*. Several important notes follow from this observation:

- The rate constant *k* can be predicted only to an order of magnitude at best when using theory, because for the majority of computational methods, an inherent accuracy of 3 kcal/mol for the relative energies is already a good value.
- The weakly varying transmission coefficient κ is usually ignored (equivalently, κ = 1).
- In case of a multistep mechanism, the reaction rate is defined by the transition state with the highest activation barrier, and the corresponding step in the rate-limiting.

Typically, a reaction in biochemistry occurs with a very high "friction" parameter when considering PES, as compared to zero "friction" of a gas phase reaction. The reason is that kinetic energy tends to dissipate very quickly in liquid medium, and frequency of interparticle collisions is much higher as compared to frequencies of kinetically

determined reaction steps. Due to this quick dissipation of kinetic energy, the $\Delta G^{\neq}$ value corresponding to the rate of a given reaction is the maximal energy difference found between any of transition states and the lowest point on the PES, preceding this particular transition state.

2.5 Solvent effects

Basic calculations in quantum chemistry are done in gas-phase manner, assuming that the interaction between the model complex and surrounding medium is negligible. However, most natural and laboratory chemistry does not occur in vacuum. There exists an interaction between solute and solvent. The solute properties as structure, stability, spectra, and reactivity depend on the solvent, particularly a polar one. To consider the solvent, a common approach is to include it as a continuum with a given dielectric permittivity constant ε and the solute is considered as contained in a cavity of this continuous medium. In the dielectric cavity methods the solvent acts as a perturbation on the gas-phase behavior of the system since the solute is subjected to the electrostatic potential created by the continuum, which in turn is polarized by the influence of the solute itself.

One of the extensively used "continuum solvation" models is the conductor-like screening model, abbreviated as COSMO. In the COSMO approach, the details of the cavity construction differ in different COSMO implementations in most cases it is constructed as an assembly of atom-centered spheres with radii approximately 20% larger than the Van der Waals radius. For the actual calculation the cavity surface is approximated by segments, e.g., hexagons, pentagons, or triangles.

COSMO derives the polarization charges of the continuum, caused by the polarity of the solute, from a scaled-conductor approximation. If the solvent were an ideal conductor the electric potential on the cavity surface must disappear. If the distribution of the electric charge in the molecule is known, e.g. from quantum chemistry, then it is possible to calculate the charge q* on the surface segments. For solvents with finite dielectric constant this charge q is lower by approximately a factor f(ε):

$q = f(\varepsilon)q^*$ (2.15)

the factor f(ε) is approximately

$$\mathbf{f}(\varepsilon) = \frac{\varepsilon - \mathbf{1}}{\varepsilon + \boldsymbol{x}} \quad (2.16)$$

where x = ½ has been found most useful based on theoretical arguments. From the thus determined solvent charges q and the known charge distribution of the molecule, the energy of the interaction between the solvent and the solute molecule can be calculated.

2.6 Chemical models

Successful applications of the B3LYP hybrid functional have proved that even transition-metal mediated reactions can be investigated by means of theoretical calculations. To date the computational power limits a quantum chemical investigation with B3LYP to a size of at most 100-200 atoms. Thus, the real enzyme systems should be reduced to a minimum-sized active site model, where those atoms undergoing chemical changes during catalysis are included. This works well as long as the activity of an enzyme depends mainly on a concentrated part, and the protein matrix can be regarded as a passive protection for the reaction center. The small part of the protein catalyzing a reaction is called the active site.

When building a model for the investigation of enzymatic catalysis, amino acid residues essential for the chemical transformation of interest can be reduced to smaller molecules. For example, the carboxylate functional group of the glutamic acid and the aspartic acid can be safely modeled as a acetate. Histidine can be modeled as an imidazole ring. In the first two parts of present thesis, the supporting ligands are further reduced to the even smaller ammonia and/or hydroxide ligand. Although these model systems are seriously truncated and might lose some minor effects on the reactivity, they are quite enough for elucidating the reaction mechanism and the comparison between the established reaction pathways. In particularly, the six model systems in chapter 4 which containing nearly identical coordination environment form a firm basis to allow us to probe the different reactivity of iron-oxo and –nitrido complexes. This investigation may offer a projection form a small molecular ensemble onto the enzymatic process.

2.7 Calculations setup

All calculations were performed with ORCA program package.[172] For geometry optimizations, the hybrid B3LYP and/or pure BP86 density functionals[159,162,163] in combination with triple-ζ quality basis sets (TZVP)[173] for key surrounding atoms involved in C-H bond activation and SVP basis sets[174] for the remaining atoms were used throughout the study. The resolution of the identity[175-177] (RI, for BP86) and RI plus chain of spheres[178] (RIJCOSX, for B3LYP) approximations were used to accelerate the calculations using the auxiliary basis set def2-SV/J.[176] All the geometries were full optimized without symmetry constraints. Harmonic vibrational frequencies were computed by two-sided numerical differentiation of analytic gradients to verify the nature of the stationary points. The minimum structures reported in this thesis have all positive eigenvalues of the Hessian matrix, whereas the transition states (TSs) have only one negative eigenvalue. The zero-point energies, thermal corrections and entropy terms for the optimized geometries were obtained from the frequency calculations.

In order to obtain single-point energies closer to the basis set limit, B3LYP calculations with the much larger def2-TZVPP basis set[179] on all elements were carried out. The energies reported in this paper refer to these calculations.

Solvent effects are taken into account via the conductor like screen model (COSMO) for all calculations. Acetonitrile (epsilon = 36.6) was chosen as the solvent. To consider dispersion forces, geometry optimizations and single point calculations were also undertaken included semi-empirical van der Waals corrections (VDW)[180-182] for diiron H-bonded system (chapter 6).

3. Analysis of Reaction Channels for Alkane Hydroxylation by Nonheme Iron(IV)oxo Complexes

3.1 Introduction

Ever since the discovery of xenobiotics degradation by cytochrome P450,[15] the functionalization of unactivated C-H bonds has been a focal point of experimental and theoretical research. Except for the well-accepted oxo-iron(IV) intermediate that presumably is the active species in cytochrome P450 as well as in some nonheme iron enzymes,[2,8,15,21] oxo-iron(V)[8,183-186] or hydroperoxo-iron(III)[5,187] intermediates might also be involved in C-H bond hydroxylation reactions. Such open-shell transition metals in high oxidation states display fascinating and highly complex reactivity patterns. The pioneering work by Schwarz, Shaik, Schröder and co-workers on the gas-phase reaction of FeO^+ with H_2 has laid out the concept of two-state reactivity as an important motif in transition metal oxidation chemistry.[112,188] It has been shown, that reaction barriers may differ dramatically on potential surfaces that are characterized by different spin multiplicities, and that the system may employ more than one such surface during the reaction.[10,189] Much progress has been made in the synthetic modeling of oxo-iron(IV).[8,51,57] Moreover, quantum chemical studies by Solomon,[5,190] Thiel,[191] Shaik,[10,114,125,189,192,193], Siegbahn,[93] Baerends,[83,194-196] de Visser[81,197,198] and their co-workers have provided a framework for the mechanistic analysis of C-H bond hydroxylation by both heme and nonheme oxo-iron(IV) complexes. A detailed mechanistic understanding of the reactivity displayed by oxo-iron(IV) centers is a prerequisite for the rational design of low-molecular weight catalysts.

Following the pioneering proposal by Groves, the alkane hydroxylation reaction by oxo-iron(IV) intermediates follows a rebound mechanism.[199] The overall mechanism in rebound chemistry is characterized by two steps: a) hydrogen atom abstraction from the substrate R-H via transition state $\mathbf{TS_H}$ leading to a hydroxyl-iron(III) weakly bound to an alkyl radical $R^\bullet$ (intermediate **I**), and b) hydroxyl back-transfer to the radical $R^\bullet$ via transition state $\mathbf{TS_{Re}}$ yielding an iron(II) centre and the hydroxylated product, R-OH.

However, there are two added layers of complexity. First, oxo-iron(IV) sites are known to exist either in triplet or quintet ground states. The majority of model complexes prefer the former,[51,57] whereas all of the identified nonheme iron enzyme active sites[21] feature the latter. More recently, model complexes with an S = 2 ground state have been synthesized.[73,200] From DFT calculations, the reactivity of quintet oxo-iron(IV) intermediates towards C-H bond hydroxylation is suggested to be much higher than the corresponding triplet species.[6,114,189,193] The second layer of complexity stems from the

geometry of the substrate approach. The cleaving C-H bond may attack the oxo-iron(IV) unit either from top (leading to an essentially linear Fe-O-H arrangement) or from an equatorial position (leading to a bent Fe-O-H geometry). Both types of reaction geometries lead to different electronic structures in the transition states and hence to different reaction pathways.

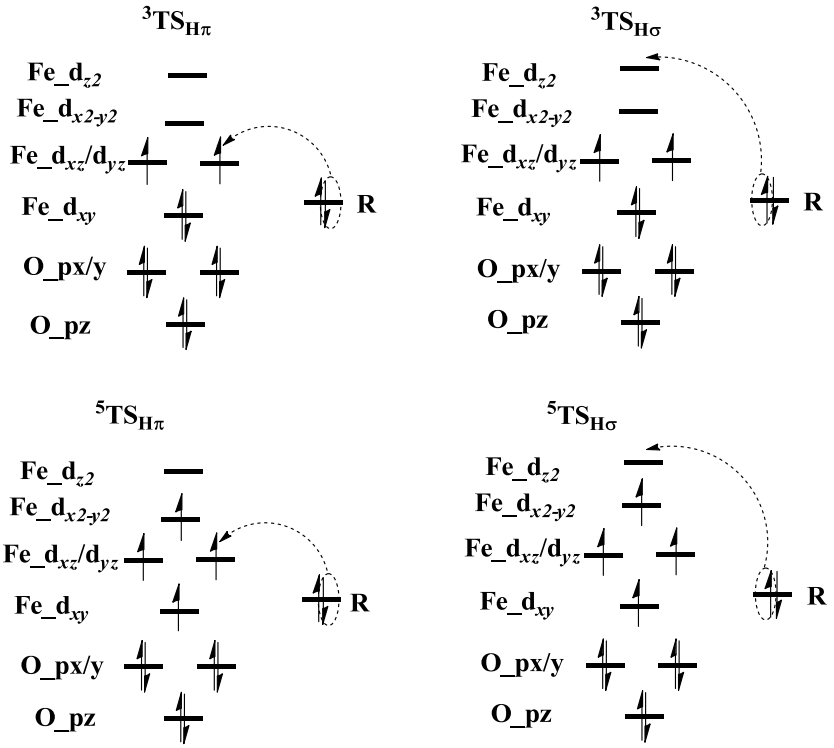

Scheme 3. 1 The feasible reaction channels for the H-atom abstraction by oxo-iron(IV) complexes.

The initial step of H-atom abstraction involves the transfer of one electron from the substrate into the metal 3d-block. Already this step is electronically complicated since it has been established that a preparatory step is needed in which the system switches from an oxo-iron(IV) to an oxyl-iron(III) on its way towards the transition state.[6] Obviously, depending on the ground state multiplicity and the geometry of C-H bond approach, several of the semi-occupied or unoccupied iron based molecular orbitals could serve as electron acceptors. In the quintet channel (Scheme 3.1, bottom right panel), the electron of the substrate is transferred into the anti-bonding σ^*(FeO) orbital (σ-mechanism). The upwards pointing lobe of the Op$_z$ orbital requires a vertical approach of the substrate and hence ^{5}**TS$_{H\sigma}$** features a nearly collinear Fe-O-H arrangement. In the triplet pathway (Scheme 3.1, top left panel), the π*(FeO) orbital accepts the electron from the substrate C-H bond (π-mechanism). The corresponding transition state ^{3}**TS$_{H\pi}$** is characterized by a bent Fe-O-H unit in order to accomplish maximum orbital overlap between the electron

donor and acceptor orbitals. In the rebound step, the C-O bond formation is accompanied with a simultaneous electron transfer from the substrate into the Fe-$d_{xz/yz}$ orbitals and the vacant Fe-d_{z2} respectively. Thus, the rebound step appears to follow a π- mechanism on the quintet state surface and a σ-mechanism on the triplet one.

Despite this already detailed understanding that has been reached through intense experimental and theoretical efforts, the picture is not yet complete. A recent study by Solomon and co-workers[201] on the benzylic hydroxylation of (4-hydroxy)mandelate synthase (HmaS) revealed a new reaction pathway on the quintet surface (Scheme 3.1, bottom left panel). Here the benzylic hydrogen approaches the electrophilic Fe-O moiety in a horizontal fashion. This leads to the transfer of a β- rather than an α-spin electron into the π*(FeO) orbital, similar to what is commonly observed for the triplet π-pathway discussed above. Thus, this study is the first one to propose a π-mechanism for H-atom transfer to an oxo-iron(IV) center on the quintet surface. However, this new channel might be regarded as a special case. First, the substrate is directly coordinated to the iron active site and hence steric encumbrance restricts it to a horizontal approach. Second, the reaction involves the abstraction of a benzylic hydrogen atom that is much weaker than aliphatic C-H bonds activated by cytochrome P450 or other nonheme iron centers.

We have thus been interested in the question, whether the quintet π-pathway is a generally competitive reaction channel for alkane hydroxylation and whether a σ-pathway is also possible on the triplet surface? (Scheme 3.1, top right panel). To this end, we have studied all four possible reaction channels with the aid of density functional theory (DFT) as well as high level coupled cluster theory with single, double and perturbative triple excitations (CCSD(T)). The chosen models resembled those previously investigated for property correlations among high-valent iron centers: $[Fe^{IV}(O)(NH_3)_5]^{2+}$ (**a**), $[Fe^{IV}(O)(OH)_{(axial)}(NH_3)_4]^{+}$ (**b**), $[Fe^{IV}(O)(OH)_{2(eq)}(NH_3)_3]$ (**c**).

3.2 Computational details

A. See **2.7 Calculations set up**

B. To obtain more accurate single-point energies, the CCSD(T) calculations for H-atom abstraction steps for all model systems were employed at the previous B3LYP geometries. The basis sets used were def2-TZVP for Fe, N, O and def2-SV(P) for H atoms.[202] The RIJCOSX approximation with def2-TZV/C basis set for Fe, N, O and SV/C for H was used to accelerate the calculations.[203] The CCSD(T) calculations were first performed on the Hartree-Fock reference orbitals. For the complexes for which the UHF equations cannot be converged to the desired state, for example, ^{3}RC, CASSCF(10,8) reference wavefunctions have been explored. Kohn-Sham orbitals obtained from B3LYP calculations are also good choice as a basis for CCSD(T) calculations. They may offer better convergence and much smaller single excitation amptitudes than Hartree-Fock orbitals.[204]

Since coupled cluster theory is known to be nearly invariant with respect to the choice of reference determinant all these choices are sensible. Indeed, the relative energies of the various species differ by less than 0.5 kcal/mol provided a qualitatively reasonable reference determinant is chosen. In order to compare the CCSD(T) energies obtained with the different reference orbitals, we also use Kohn-Sham reference orbitals for all species in system **b**. The T1 magnitudes, often taken as a diagnostic measure of multi-reference character, lie well within the range of 0.007~0.023, which indicates reliable CCSD(T) results.

3.3 Results and discussion

The calculated geometric parameters of the transition states of these systems are shown in Table 3.1 which agrees well with previous results of the same pathways.[114,125,195,205] Figure 3.1 shows the potential energy profiles of the ethane C-H bond hydroxylation by these model systems. Since the three model complexes follow the same reaction trend, we only give a detailed discussion on model system **a**.

Table 3. 1 Geometric parameters of the transition states of complexes a**,** b **and** c**.**

	Fe-O	O-H	C-H	C-O	∠FeOH	∠FeOC
$^{3}TS_{H\pi}{}^{a}$	1.78	1.21	1.33	~	118.9	~
$^{3}TS_{H\sigma}{}^{a}$	1.78	1.16	1.37	~	174.9	~
$^{5}TS_{H\sigma}{}^{a}$	1.74	1.27	1.26	~	175.8	~
$^{5}TS_{H\pi}{}^{a}$	1.76	1.21	1.33	~	123.1	~
$^{3}TS_{Re\sigma}{}^{a}$	1.91	0.97	~	2.27	~	160.0
$^{5}TS_{Re\pi}{}^{a}$	~	~	~	~	~	~
$^{5}TS_{Re\sigma}{}^{a}$	1.84	0.97	~	2.79	~	174.7
$^{3}TS_{H\pi}{}^{b}$	1.78	1.18	1.35	~	118.7	~
$^{5}TS_{H\sigma}{}^{b}$	1.80	1.24	1.28	~	148.7	~
$^{5}TS_{H\pi}{}^{b}$	1.80	1.19	1.35	~	119.9	~
$^{3}TS_{Re\sigma}{}^{b}$	1.92	0.97	~	2.19	~	153.7
$^{5}TS_{Re\pi}{}^{b}$	1.89	0.97	~	2.52	~	132.7
$^{5}TS_{Re\sigma}{}^{b}$	1.87	0.97	~	2.48	~	164.3
$^{3}TS_{H\pi}{}^{c}$	1.89	1.17	1.37	~	121.5	~
$^{5}TS_{H\sigma}{}^{c}$	1.81	1.23	1.29	~	142.7	~
$^{5}TS_{H\pi}{}^{c}$	1.80	1.16	1.40	~	117.4	~
$^{3}TS_{Re\sigma}{}^{c}$	2.02	0.97	~	2.09	~	161.5
$^{5}TS_{Re\pi}{}^{c}$	1.97	0.97	~	2.24	~	130.3
$^{5}TS_{Re\sigma}{}^{c}$	1.95	0.97	~	2.31	~	161.9

We first discuss the hydroxylation reactions based on the DFT calculations. The processes that proceed through $^{3}TS_{H\pi}{}^{a}$ and $^{5}TS_{H\sigma}{}^{a}$ represent the established pathways on the triplet

and quintet surfaces. The reactions proceeding via $^{3}TS_{H\sigma}{}^{a}$ and $^{5}TS_{H\pi}{}^{a}$ are the non-classical ones. The triplet and quintet oxo-iron(IV) reactants have very similar energy, which is consistent with previous studies.[114,125,197] Comparison of the calculated energy barriers for H-abstraction demonstrates that the quintet σ-pathway encounters by far the lowest barrier among the four alternatives. By contrast, the π-pathways on the triplet and quintet surfaces have comparable energy barriers. The barrier of the triplet σ-pathway, which could only be located for model system **a**, is much higher in energy. For the rebound step, the triplet pathway involves a higher energy barrier than the quintet one. Hence, it is clear that the hydroxylation reactivity decreases in the order $^{5}\sigma > {}^{5}\pi > {}^{3}\pi > {}^{3}\sigma$. Apart from the non-classical channels discussed here, our results are in agreement with previous studies[81,93,194-196] that demonstrate that the quintet iron(IV)-oxo species is more reactive than the corresponding triplet species.

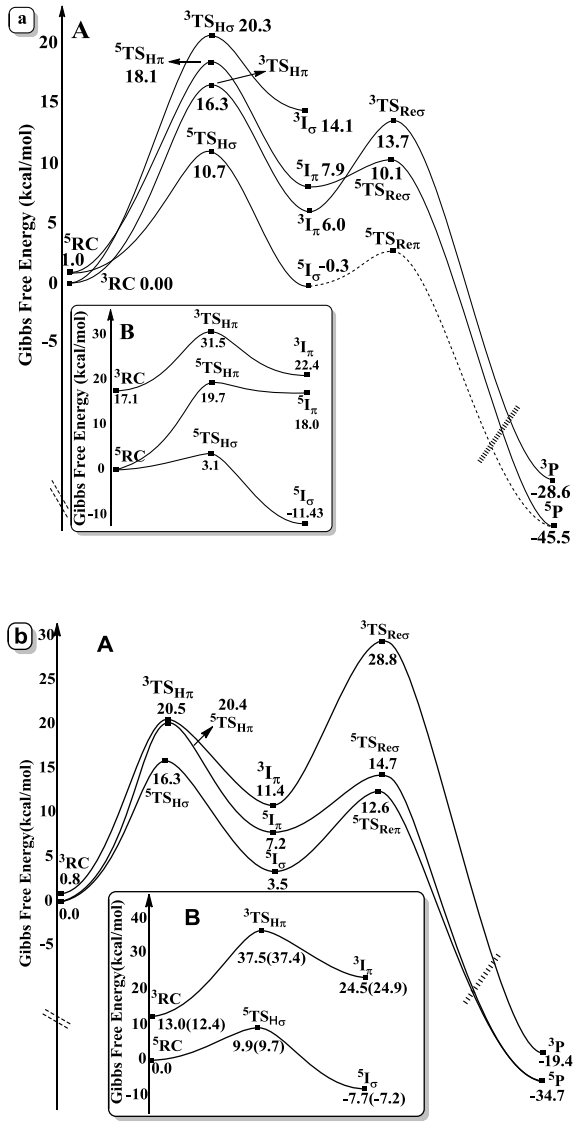

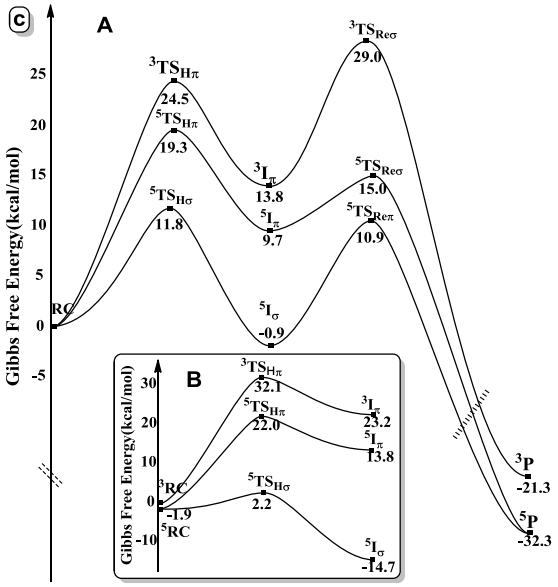

Figure 3. 1 Schematic Gibbs free energy (ΔG) energy surface for ethane hydroxylation by three model systems: (A) B3LYP/def2-TZVPP//B3LYP/TZVP, (B) CCSD(T) (def2-TZVP for Fe, N, O and def2-SV(P) for H atoms)//B3LYP/TZVP.

Since the electron transfer steps in the established triplet (π-mechanism) and quintet reaction pathways (σ-mechanism) have been well studied, our discussion will mainly focus on the π-mechanism on the quintet state surface and the σ-pathway on the triplet state. Figure 3.2 shows the schematic MO diagrams for the two non-classical pathways of system **a**. It becomes evident that in ^{5}**TS**$_{H\pi}^{a}$ a β-electron from the substrate is shifted towards the Fe-d_{xz} based orbital, consistent with a horizontal approach of the ethane molecule towards the Fe-O moiety. The key geometric parameters of ^{5}**TS**$_{H\pi}^{a}$ closely resemble those found in ^{3}**TS**$_{H\pi}^{a}$ (Table 3.1), i.e. a nearly collinear O-H-C moiety, comparable C-H and O-H bond distances and a significantly bent Fe-O-H angle. These findings may be rationalized by reference to the electronic configuration of ^{5}**TS**$_{H\pi}^{a}$. As the substrate approaches the oxo-iron(IV) unit, the Fe-O bond gradually elongates and an electron hole is generated in the O-p_x based orbital[201] (thus forming a ferric-oxyl species) which finally serves as the true electron acceptor. In order to assure the best orbital interactions between the C-H σ-bond and the O-p_x orbital, the substrates must approach the FeO core horizontally with a Fe-O-H angle of 90°; however, this orientation is only possible at the expense of a much larger Pauli repulsion than in the σ-type attack geometry.[83] Consequently, the opposing requirements of optimal orbital overlap and increasing Pauli repulsion lead to bent geometries in ^{5}**TS**$_{H\pi}^{a}$ with a Fe-O-H angle close to 120°. Compared to the reduced Pauli repulsion and the optimum orbital interaction of the vertical approach in the quintet σ-mechanism, one may readily appreciate why ^{5}**TS**$_{H\sigma}^{a}$ features the smallest barrier of the three pathways (^{5}**TS**$_{H\sigma}^{a}$, ^{5}**TS**$_{H\pi}^{a}$ and ^{3}**TS**$_{H\pi}^{a}$). Unlike ^{5}**I**$_{\sigma}^{a}$ containing a high spin ferric ion (S_{Fe} = 5/2) that is antiferromagnetically coupled to an alkyl

radical (S_C = 1/2), the H-abstraction process through the π-mechanism finally leads to an intermediate (**$^5I_\pi{}^a$**) containing an intermediate spin iron(III)-hydroxo complex (S_{Fe} = 3/2) *ferromagnetically* coupled to an ethylic radical.

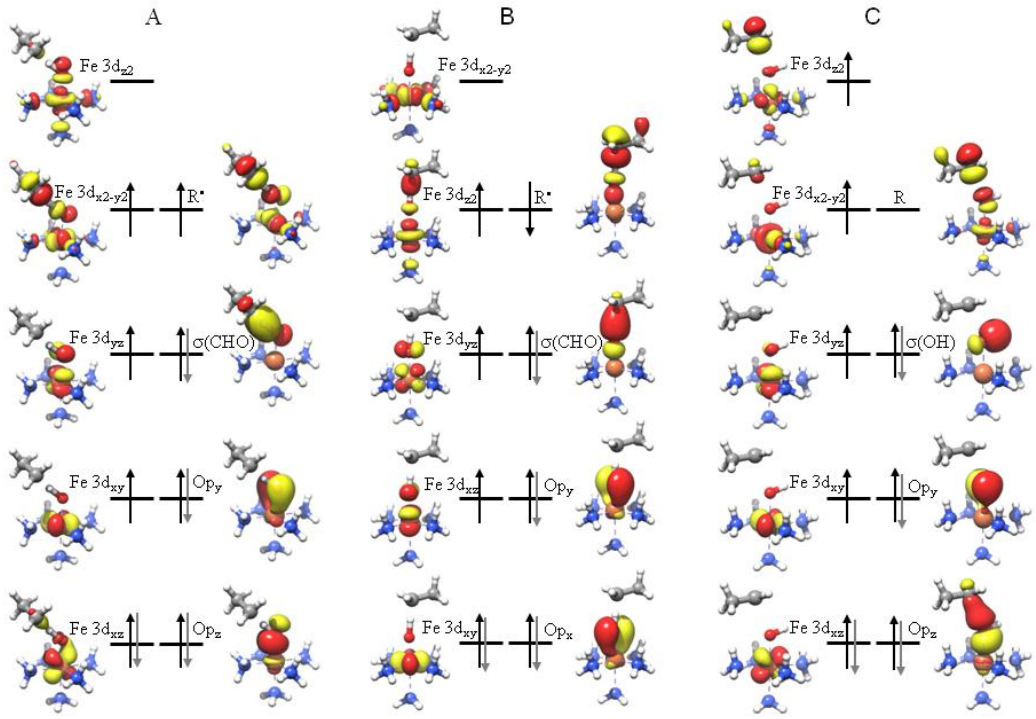

Figure 3. 2 Schematic MO diagram of $^5TS_{H\pi}$ (A), $^3TS_{H\sigma}$ (B), $^5TS_{Re\sigma}$ (C) for $[Fe^{IV}(O)(NH_3)_5]^{2+}$.

The vertical approach of ethane towards the Fe-O moiety in **$^3TS_{H\sigma}{}^a$** leads to an α-electron transfer from the substrate to the σ^*(FeO) antibonding orbital. Although the nearly collinear arrangement of Fe-O-H-C features the best orbital interactions and smallest Pauli repulsions, the LUMO+1 acceptor orbital σ^*(FeO) is much higher in energy compared to the corresponding orbital in **$^5TS_{H\sigma}{}^a$** due to the greatly reduced spin polarization.[190] The high activation energy of **$^3TS_{H\sigma}{}^a$** is also in agreement with the geometric parameters that indicate a rather 'late' transition state. The electronic structure of **$^3I_\sigma$** features antiferromagnetic coupling between an intermediate spin ferric (S_{Fe} = 3/2) and an alkyl radical (S_C = 1/2). The energies of these four intermediates of varying spin multiplicities decrease in the order **$^5I_\sigma{}^a$** (S_{Fe} = 5/2) > **$^5I_\pi{}^a$** (S_{Fe} = 3/2) ≥ **$^3I_\pi{}^a$** (S_{Fe} = 1/2) > **$^3I_\sigma{}^a$** (S_{Fe} = 3/2) consistent with the weak ligand fields arising from typical nonheme ligand frameworks.

Starting from **$^5I_\pi{}^a$**, the rebound step follows a σ-mechanism through **$^5TS_{Re\sigma}{}^a$** like in the triplet π-channel. In either case, the remaining α-electron of the substrate radical is transferred to the strongly σ-antibonding Fe-d_{z2} orbital (A schematic MO diagram of a post-**$^5TS_{Re\sigma}{}^a$** geometry with a C-O bond distance of 2.5Å is shown in Figure 3.2). As the

electron is shifted along the Fe-O axis, an almost linear Fe-O-C angle of 174.7° is calculated in $^{5}\mathbf{TS}_{\mathbf{Re}\sigma}{}^{\mathbf{a}}$. Comparison of the rebound pathways reveals that the two channels on the quintet state surface[80] have a very similar energy barrier while the triplet σ-mechanism process encounters the highest one. This trend may be ascribed to two factors: a) the nature of electron acceptor orbital and b) the spin polarization induced by the singly occupied orbitals in the metal d-block. Given the comparatively weak π-antibonding nature of the t_{2g}-derived orbitals compared to the strongly σ-antibonding nature of the Fe-d_{z2} based orbital together with the large spin-polarization of the quintet state, it becomes understandable why $^{5}\mathbf{TS}_{\mathbf{Re}\pi}{}^{\mathbf{a}}$ corresponds to the lowest energy rebound step on the three surfaces. The situation on the triplet surface is exactly opposite. Here the acceptor orbital is the strongly σ-antibonding Fe-d_{z2} orbital and triplet state spin-polarization is much less effective compared to the quintet state. An intermediate situation exists in $^{5}\mathbf{TS}_{\mathbf{Re}\sigma}{}^{\mathbf{a}}$.

The CCSD(T) level energies based on B3LYP optimized geometries predict larger triplet-quintet splittings, again consistent with other studies.[206] The CCSD(T) results are slightly biased in favour of the high spin state of oxo-iron(IV) complexes. The same behaviour is also found in the Spectroscopic Oriented Configuration Interaction (SORCI) calculations.[207] However, it is clear that there is a very large basis set dependence[204,208] and the basis set limit is difficult to reach with CCSD(T) calculations for systems of the present size. The activation energies obtained from CCSD(T) calculations for triplet and quintet pathways show a similar trend. In particular, the energy of $^{5}\mathbf{TS}_{\mathbf{H}\sigma}{}^{\mathbf{a}}$, which involves a high spin ferric iron (S_{Fe} = 5/2), is greatly reduced. The pathways involving intermediate spin iron centers (S_{Fe} = 3/2)), similar energy barriers as predicted by B3LYP calculations are obtained. This bias may disappear at the basis set limit, that is, unfortunately, not approachable with presently available computational resources. A detailed discussion of how to best obtain accurate spin state energies for transition metal complexes is beyond the scope of the present work. Nevertheless, the CCSD(T) results are broadly consistent with the B3LYP numbers for the H-atom abstraction steps, and further corroborate that the quintet σ-pathway is the most feasible channel. The CCSD(T) results also confirm that the quintet π-pathway is highly competitive.

3.4 Conclusion

In conclusion, this is the first time that all viable pathways are identified in the same system, which allows us to compare their relative reactivities. The triplet σ-pathway is higher in energy such that it may not ever be involved in actual C-H bond hydroxylations. However, the reactivity of the quintet π-channel is comparable or even higher than the classical triplet one ($^{3}\boldsymbol{\pi}$), although it is slightly higher in energy than the established quintet one ($^{5}\boldsymbol{\sigma}$). The existence of at least three energetically feasible pathways may offer, however, a new element of specificity control in C-H bond activation reactions by oxo-

iron(IV) species. The choice of σ- or π-pathways could be controlled at least in part by steric hinderance in model systems or by the restrictions of the protein pocket in metalloenzymes.[190]

4. Does a Higher Oxidation State of a Metal Center Necessarily Imply Higher Oxidizing Power? A Computational Study of C-H Bond Activation by High–Valent Iron–oxo and –nitrido Complexes

4.1 Introduction

The isoelectronic high-valent iron–oxo and –nitrido species have been considered as key intermediates in a number of important biochemical transformations. For example, heme and non-heme O_2-activating iron enzymes utilize iron–oxo species to selectively oxidize unactivated C–H bonds,[8,21,22,34,35,47-50] while iron–nitrido intermediates are the pivotal species for biological synthesis of ammonia.[136,209-212] These two kinds of reactions, however, are also extremely important industrial processes. Therefore, majority of effort has been dedicated to identify and understand key features of these isoelectronic species in both biological processes and laboratory researches.

For the iron–oxo complexes, iron(IV)oxo and iron(IV)oxo porphyrin radical (Compound I) have been spectroscopically identified as active intermediates for C–H bond oxidation in nonheme and heme systems, respectively.[8,21,22,34,35,47-50] Iron(IV)–oxo complexes have been extensively studied and some common conclusions have been reached.[5,11,21,51,57,93,189,213-215] For example, the consensus OH rebound mechanism was established for C–H bond hydroxylation by ferryl species;[80,114,193,199,216] the quintet iron(IV)-oxo species is a more aggressive oxidant than its triplet counterpart;[5,81-84] the reactivity of iron–oxo complexes can be tuned by changing the axial ligand trans to the oxo group.[55,65,121,126,195,217] All these accumulated information has provided vital insights into the mechanisms that nature uses to carry out the important biochemical transformation.

In contrast to numerous iron(IV)–oxo complexes, genuine iron(V)–oxo species are rather rare. The $Fe^{V}(O)(OH)$ species was proposed as the active oxidant responsible for the *cis*-dihydroxylation of C=C double bonds in the catalytic cycle of Rieske dioxygenases; however, only indirect proof for its existence was obtained.[8,26,30,214,218] Theoretical studies demonstrated that this putative perferryl species has rather high reactivity towards strong C–H bond activation and is able to afford large turnover numbers of epoxide and *cis*-dihydroxylation products with unprecedented efficiency.[28,33,185,219-221] The first isolated and well characterized true iron(V)–oxo complex ($[(TAML)Fe^{V}(O)]^{-}$) was reported by Collins, Que and Münck and coworkers.[77] The iron(V) oxidation state was confirmed on the basis of its characteristic Mössbauer and EPR spectrum, as well as the EXAFS evidence. The detailed reactivity studies revealed that this authentic iron(V)–oxo complex is a strong

electrophile toward the electron-rich sulfides. As in the oxygen atom transfer (OT) with organic sulfides, $[(TAML)Fe^{V}(O)]^{-}$ is established to be a high efficient oxidant and it is 4 orders of magnitude more reactive toward sulfides than its Fe^{IV} product.[222] However, this Fe^{IV} complex is a *u*-oxo-$(Fe^{IV})_2$ dimer, totally different with basic coordination environment of the iron(IV)-oxo species we mentioned above. Therefore, the direct information for the comparison of the reactivities of this iron(V)-oxo with iron(IV)-oxo complexes is still lacking. When return to the C–H bond activation we cared about, it turns out that $[(TAML)Fe^{V}(O)]^{-}$ is a sluggish oxidant, since it only reacts with the weak C–H bonds of dihydroanthracene, and no *cis*-dihydroxylation reactions have thus far been reported. Neither theoretical studies have been addressed so far.

Iron(VI)–oxo complexes are even much more rare, and the only known example is the tetrahedral $Fe^{VI}O_4^{2-}$ anion.[223-226] This may be due to its significant oxidizing power. In line with this, ferrate (FeO_4^{2-}), derived from mineral salts such as the potassium (K_2FeO_4) and barium ($BaFeO_4$) forms, can mediate oxidation of a wide variety of organic compounds such as alcohols,[227,228] amines,[228] hydrazines,[229] peroxides,[230] hydrocarbons,[231] and thiosulfates[232] with excellent selectivity.

Similar to the putative $Fe^{V}(O)(OH)$ species in Riske dioxygenases, the direct evidence for the involvement of iron-nitrido intermediates in biology remains elusive. The mechanistic postulates involving high-valent iron–nitrido moieties have nevertheless motivated the synthesis and reactivity studies of such model compounds. Till now, synthetic iron nitrides complexes have +4,[140,141,150] +5,[145,147,148,205] and +6[149,205] oxidation states. All reported terminal iron(IV) nitrido complexes possess the distorted trigonal pyramidal coordinate environment and two isolable iron(IV) nitrido complexes have been crystallographically characterized recently.[140,142,143,150] The characterization of iron(V)-nitrido complexes started from the resonance Raman detection of $[Fe^{V}(N)(TPP)]^{-}$ (TPP^{2-} = tetraphenylporphinate(2-)) complex by Nakamato and coworkers.[151] More recently, the photolysis of $[(cyclam–ac)Fe(N_3)]^{+}$ ($cyclam–ac^{-}$ = 1,4,8,11–tetraazacyclitetradecane–1–acetate) leading to the desired $[(cyclam–ac)Fe^{V}(N)]^{+}$ species was reported.[53] Later, the detailed geometric and electronic structure analysis combined by spectroscopic and theoretical approaches revealed the doublet ground state rather than the quartet spin state previously assumed.[148] Very recently, Meyer and Smith reported the synthesis of a four–coordinated iron(V) nitrido complex supported by a tripodal N–heterocyclic carbine (NHC) ligand, which also feature a low–spin (S = 1/2) ground state.[144] When it comes to the iron(VI) nitrido complex, Wieghardt and coworkers reported the second Fe(VI) compound (the first one is $[Fe^{VI}O_4]^{2+}$ as mentioned before) generated by photolysis of a stable iron(IV) azido compound, $[(Me_3–cyclam–ac)Fe^{IV}(N_3)]^{2+}$.[149] This is the first hexavalent iron compound to be synthesized in laboratory. The reactivity of these complexes has also been investigated in depth experimentally; however, most of the iron-nitrido species

exhibited to be non-catalytic, with activities falling far short of the activity of iron–oxo complexes.[142-144]

As mentioned above, intense investigations have been dedicated to clarify the property and reactivity of individual high–valent iron–oxo/nitrido complexes. However, to our knowledge systemic theoretical research on the two series is still very rare. Neese et al. have done a thorough computational study on six "hypothetic" iron–oxo/nitride model complexes (**1–6** in Chart 1).[205] This is the first time to compare the different spectroscopic properties of iron–oxo and –nitrido complexes with iron oxidation states spanning from +4 to +6. However, no reactivity trends were predicted for these complexes. We have therefore chosen to investigate the reactivity of **1 – 6**. The iron centers of the model compounds are coordinated in distorted octahedral arrangements with ammonia acting as the equatorial ligands, and hydroxyl group as the axial ligand trans to the oxo or nitrido group. The nearly identical coordination environment of **1 – 6** allows us to make more generalized comments about the relative reactivity of high-valent iron–oxo and –nitrido complexes. Clarifying the difference in reactivity between the two series may contribute to a basis for enhanced understanding of nature's redox enzymes and the matching catalyst systems to target oxidation processes.

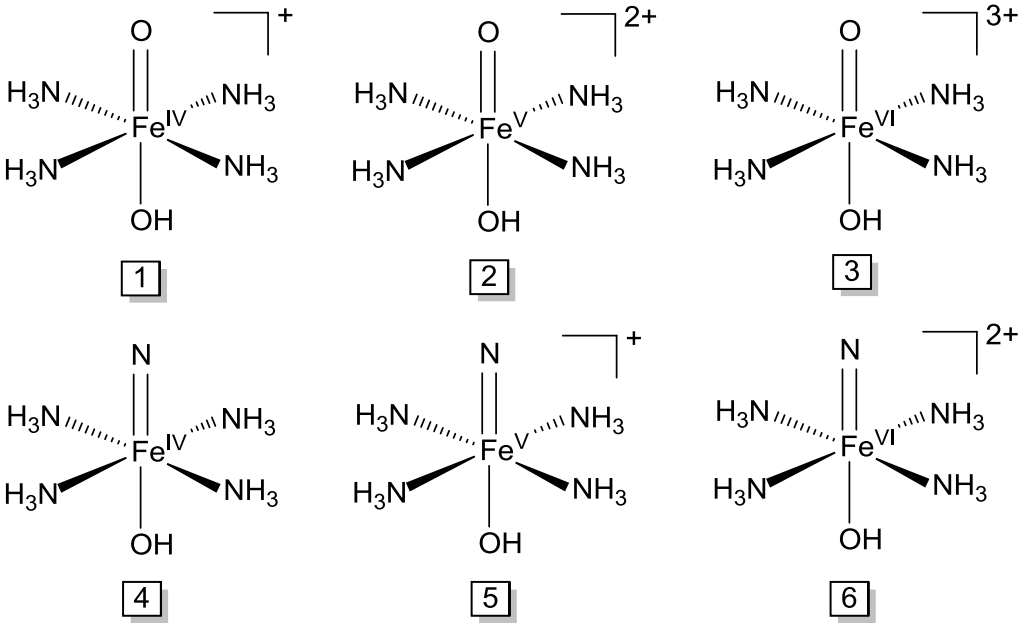

Scheme 4. 1 Six high-valent iron–oxo and –nitrido complexes

4.2 Computational details

See **2.7 Calculations set up**

4.3 Results

4.3.1 Geometry structures

In this section, we focus on the properties of Fe=O/N bond which is closely related to the ethane C–H bond activation. Table 4.1 collects the selected geometric parameters and electronic structures and Figure 4.1-4.4 presents all the schematic MO diagrams calculated by B3LYP.

4.3.1.1 Iron–oxo complexes

Calculations with the B3LYP functional of Fe(IV)–oxo species **1** has been well studied in Chapter 3[216] and the calculated Fe=O bond distance of 1.64 Å is in good agreement with experimental studies.[54]

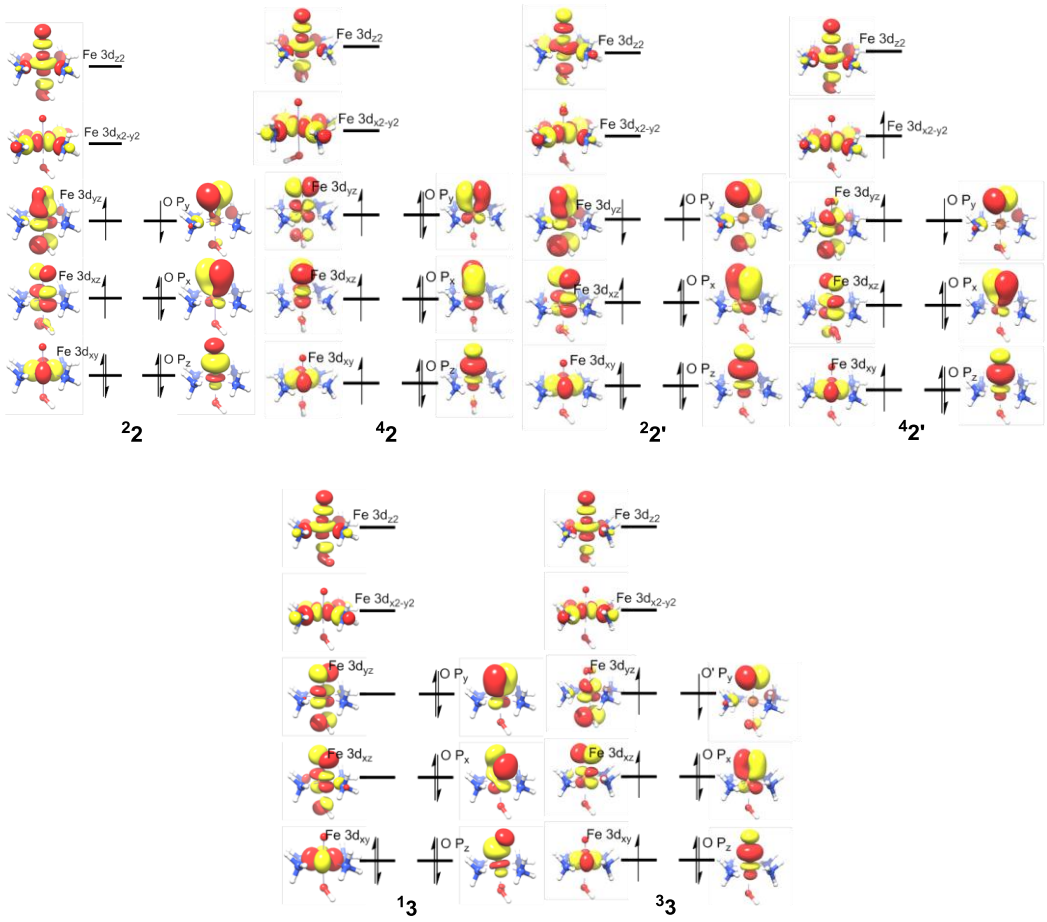

Figure 4. 1 B3LYP Calculated Schematic MO diagrams for complex 2 and 3.

.

As for the iron(V)–oxo complex **2**, there were four different electronic configurations established with the B3LYP functional, two for doublet state (^{2}**2**, and ^{2}**2**′), and two for quartet state (^{4}**2**, and ^{4}**2**′). As shown in Table 4.1, ^{2}**2** is the ground state and is favored by 5.0, 2.8, and 14.8 kacl/mol over the ^{2}**2**′, ^{4}**2**, and ^{4}**2**′ states. The optimized Fe–O bond distances with B3LYP functional are 1.72 (1.65 Å), 1.68Å (1.75 Å) for ^{2}**2** (^{2}**2**′) and ^{4}**2** (^{4}**2**′), respectively, in agreement with other calculated iron(V)oxo complexes, $[(tpa)Fe^{V}(O)(OH)]^{2+}$ (1.69 Å), for example.[183] While the values are dramatically different from that found in the well–characterized iron(V)oxo complex, $[FeO(TAML)]^{-}$ (1.60 Å) and even longer than that calculated for the iron(IV)oxo analog **1** (1.64 Å).[77] The extremely longer Fe=O bond distance in the current model may be rationalized by its distinct electronic configurations predicted with B3LYP functional. As shown in Figure 4.1, only ^{4}**2** contains a genuine Fe(V) center among the four electron configurations calculated using B3LYP. The other three electron configurations (^{2}**2,** ^{2}**2**′, and ^{4}**2**′) are best described as consisting of an intermediate-spin iron(IV) center that is antiferromagtically or ferromagnetically coupled to an oxyl radical. This special electron configuration slightly reduces the Fe=O bond order and thereby lengthening the Fe=O bond in **2**.

With the highest iron oxidation state, the hypothetic iron(VI)oxo complex **3** has two low–lying electronic state, singlet and triplet. B3LYP calculations predict the triplet ground state with the singlet state lying 10.8 kcal/mol above it. The calculated Fe=O bond lengths of ^{1}**3** is 1.53 Å, which is greatly shorter than those in **1** and **2**. By contrast, ^{3}**3** possess an elongated Fe=O bond (1.72 Å) which is interestingly comparable to the Fe–O_{OH} (1.79 Å) bond distance, reflecting a delocalized O=Fe=O unit generated by the greater Fe–O π-bonding to both axial ligands. Electronically, the expectedly remarkable short Fe=O bond in ^{1}**3** may be attributed to the triple bond formed between the iron center and oxo group. As shown in Figure 4.1, the B3LYP result indicates that ^{1}**3** indeed contains a genuine Fe(VI) center with two paired electrons residing in the nonbonding d_{xy} orbital and hence implies a bond order of 3 for the Fe and oxo interaction. While ^{3}**3**, in fact, consists of a high spin Fe(V) center that is antiferromagneitcally coupled to an oxyl radical, hence resulting in a longer Fe=O bond relative to ^{1}**3.**

4.3.1.2 Iron–nitrido complexes

The Fe(IV)–nitrido complexes **4** has the quintet ground state and the triplet state is about 6.3 kcal/mol higher in energy. The geometry description of **4** is somewhat more complicated. In contrast to the remarkably short Fe=N distance and distorted structure predicted previously,[205] our B3LYP calculations proposed a slightly distorted octahedral geometry with a relatively long Fe=N bond distance (~1.72 Å) for both spin states. ^{3,5}**4** possess analogous electronic structures to those of the corresponding oxo counterpart, the remarkable difference is that an inverted bonding situation is observed for the nitrido species.

The much higher energy of ^{4}**5** compared to that of ^{2}**5** rendered us safely rule out the existence of ^{4}**5**, and therefore our discussion here is only focus on the doublet state. The key geometric and electronic characters for the ground state ^{2}**5** closely resemble those found in ^{2}**2**. For example, B3LYP predicts a rather longer Fe=N bond (1.70 Å) and the similar broken symmetry solution leads to a formal iron(V) center in ^{2}**5**.

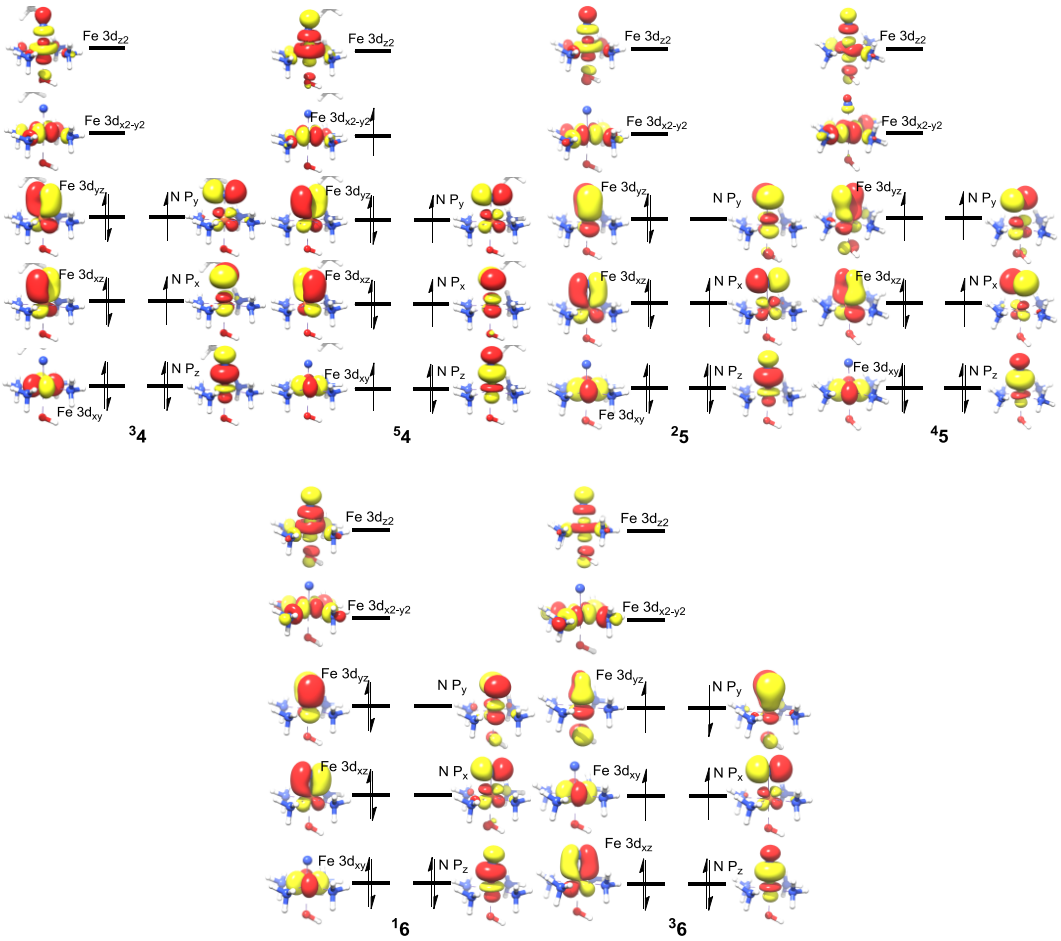

Figure 4. 2 B3LYP Calculated Schematic MO diagrams for complexes 4, 5 and 6.

The discussion of ^{3}**6** can also be excluded due to its extremely high energy (Table 4.1). Much as found in ^{1}**3**, ^{1}**6** has a very short Fe=N bond distance, 1.51 Å, and a slightly longer Fe–O_{OH} bond which indicates the stronger *trans* effects of nitrido relative to oxo. The schematic MO diagrams for complex ^{1}**6** possess a $d_{xy}^{2}d_{xz}^{2}d_{yz}^{2}$ electronic configuration on Fe center and the empty N P_y and P_x orbitals resulting in an electronic description of LS–$Fe^{II}N^{+}$ in which the Fe=N unit approaches a triple bond in agreement with a very short distance calculated for ^{1}**6**.

Table 4. 1 Calculated Energies and Selected Geometric Parameters and electronic structures for the high-valent Iron–Oxo and –Nitrido Complexes predicted by B3LYP calculations (Energy in kcal/mol and Bond Distances in Angstroms).

		Energy	Fe=E (E=O or N)	Electronic structure
1	^{3}**1**	0.0	1.64	$Fe^{IV}O^{2-}$
	^{5}**1**	3.6	1.64	$Fe^{IV}O^{2-}$
2	^{2}**2**(^{2}**2′**)	0.0(2.8)	1.72(1.65)	$Fe^{IV}O^{\bullet-}$
	^{4}**2**(^{4}**2′**)	5.0(14.8)	1.68(1.75)	$Fe^{V}O^{2-}$
3	^{1}**3**	10.8	1.53	$Fe^{VI}O^{2-}$
	^{3}**3**	0.0	1.72	$Fe^{V}O^{\bullet-}$
4	^{3}**4**	6.3	1.72	$Fe^{IV}N^{3-} \leftrightarrow Fe^{II}N^{\bullet\bullet-}$
	^{5}**4**	0.0	1.69	$Fe^{IV}N^{3-} \leftrightarrow Fe^{II}N^{\bullet\bullet-}$
5	^{2}**5**	0.0	1.70	$Fe^{V}N^{3-} \leftrightarrow Fe^{III}N^{\bullet\bullet-}$
	^{4}**5**	13.0	1.90	$Fe^{V}N^{3-} \leftrightarrow Fe^{III}N^{\bullet\bullet-}$
6	^{1}**6**	0.0	1.51	$Fe^{VI}N^{3-} \leftrightarrow Fe^{II}N^{+}$
	^{3}**6**	25.6	1.70	$Fe^{VI}N^{3-} \leftrightarrow Fe^{IV}N^{\bullet\bullet-}$

4.3.2 Reactivity

As the well-established hydrogen atom transfer (HAT) mechanism for the C-H bond activation by iron(IV)-oxo complexes,[85,189,216,233,234] here too, all the B3LYP calculations pointed toward an initial HAT from a C-H bond in ethane to the iron-oxo or -nitrido group of oxidants **1** – **5**, except for iron(VI)-nitrido complex **6** (*vide infra*). These reactions can be written schematically as in the following equation:

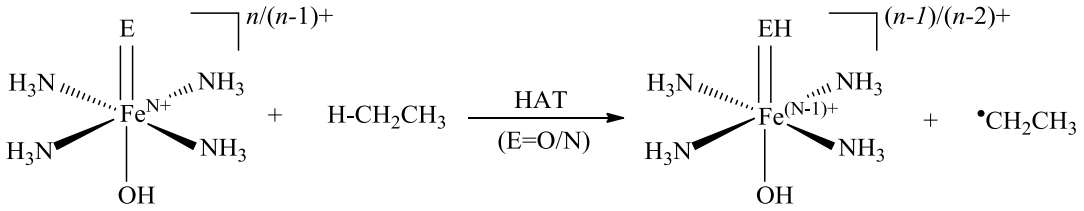

Clearly, in contrast to the classic organic HAT reactions which use a p-block radical $X^{\bullet}$ such as t-butoxyl as an abstraction group, addition of $H^{\bullet}$ to the iron-oxo and –nitrido complexes typically results in protonation of oxo and nitride ligands and reduction of the iron center.

4.3.2.1 Iron–oxo complexes

Figure 4.3 shows the potential energy surfaces (PES) of the ethane H–atom abstraction by complexes **1** and **2** and Figure 4.4 demonstrates the electronic structures of transition state. Table 4.2 shows the key geometric parameters of the critical points along these reaction pathways. Since the B3LYP calculated C–H bond activation by complex **1** has been

discussed in Chapter 3,[216] we only put the PES and geometric parameter here for comparison and start our detailed research from complex **2**.

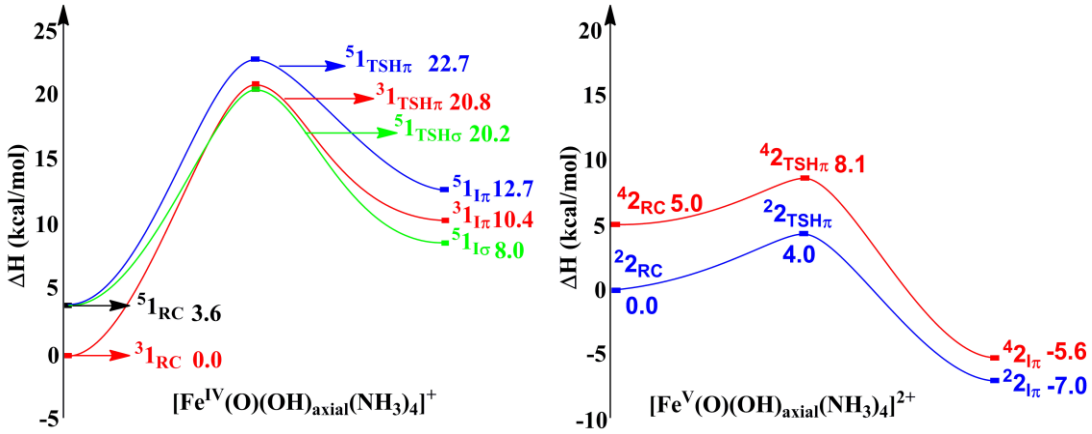

Figure 4. 3 Schematic energy profiles (ΔH) for the ethane hydroxylation by complexes 1 ([Fe^{IV}O(OH)(NH$_3$)$_4$]$^+$) and 2 ([Fe^{V}O(OH)(NH$_3$)$_4$]$^{2+}$).

As might have been expected from the higher oxidation state, complex **2** is a stronger oxidant than **1** as evidenced by the corresponding lower barriers. As shown in Figure 4.3, comparison of the calculated energy barriers for hydrogen–atom abstraction demonstrates that the doublet and quartet state pathways encounter similar energy barriers (~4 kcal/mol) which is much lower than those calculated for the reaction with **1** (17.8 kcal/mol). In accord with the much lower energy barriers for **2**, very early transition states are predicted on both doublet and quartet state surfaces. As shown in Table 4.2, relatively short C–H bonds (1.18 Å) and significantly long O–H bonds (1.48 Å) are estimated in both transition states. The C–H bond activation by ^{2,4}**2** both follows the π–mechanism. For doublet state, the antiferromagnetically coupled intermediate spin Fe(IV) metal center and oxyl radical in reactant already electronically resemble the "real" oxidant that is required for the hydroxylation by iron(IV)oxo species.[6,216] The oxyl radical character makes ^{2}**2** to be more reactive than **1** due to its higher electrophilicity. Indeed, based on the changes in the electronic structure along the reaction pathway, one may easily view the hydrogen atom abstraction process in doublet state as the transformation of an iron(IV)–oxyl species into an iron(IV)–hydroxy complex. As shown in Figure 4.5, in contrast to the β–electron transfer in the π–pathway for ^{3}**1**, the α–hole in the oxyl ligand induces an α–electron shift from the substrate to the $(FeO)^{3+}$ unit in the reaction of ^{2}**2**. For the quartet state, there is no significant interaction achieved between the substrate and the Fe=O active center which is in good agreement with the very early geometry structure described above. The electronic structure change for ^{4}**2** is similar to the preparatory stage found for the H–atom abstraction by ^{3}**1**, that is, upon approaching TS, ^{4}**2** evolve to a species that is best characterized as a Fe(IV)–oxyl species, generating an electron hole on the oxygen atom. Consequently, an equatorial approach of the substrate towards the Fe–

O unit for both spin states leads to $^{2}\mathbf{2}_{TSH\pi}$ and $^{4}\mathbf{2}_{TSH\pi}$ with a significantly bent Fe–O–H angle (~120°). Thermodynamically, the exothermic rather than the moderate endothermic character of the reactivity indicate that **2** has much larger driving force than **1**, in good agreement with the higher reactivity of **2** compared to that of **1**.

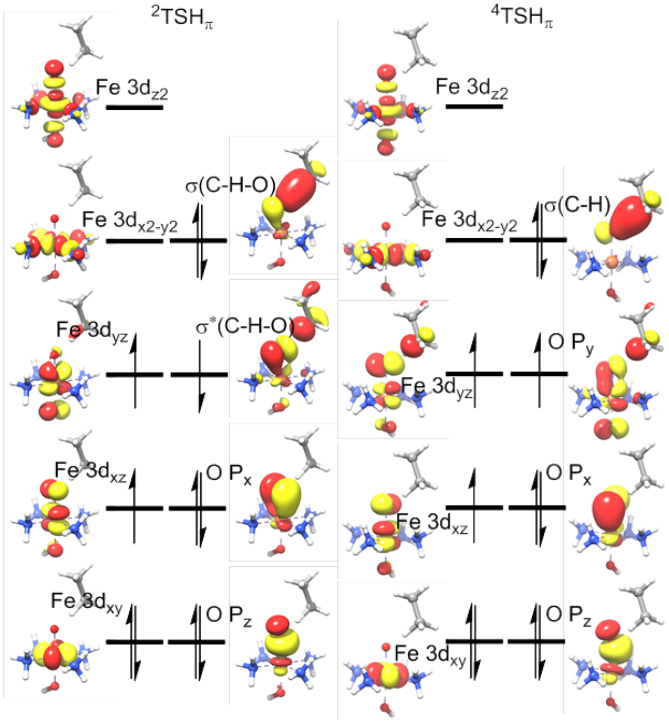

Figure 4. 4 Schematic MO diagram of $^{2}TSH_{\pi}$ and $^{4}TSH_{\pi}$ for complex 5 $[Fe^{V}O(OH)(NH_3)_4]^{2+}$. C grey, N blue, O red, Fe orange.

Table 4. 2 Selected Key Geometric Parameters of Transition States for C-H Bond Activation by the high-valent Iron Oxo and Nitrido Complexes (Bond Distances in Angstrom, Angles in Degree).

		Fe=E(E=O or N)	E-H(E=O or N)	C-H	∠FeOH
		B3LYP	B3LYP	B3LYP	B3LYP
1	$^{3}\mathbf{1}_{TSH\pi}$	1.78	1.18	1.35	118.7
	$^{5}\mathbf{1}_{TSH\sigma}$	1.80	1.24	1.28	148.7
	$^{5}\mathbf{1}_{TSH\pi}$	1.80	1.19	1.35	119.9
2	$^{2}\mathbf{2}_{TSH\pi}$	1.73	1.47	1.18	121.2
	$^{4}\mathbf{2}_{TSH\pi}$	1.79	1.48	1.18	122.0
4	$^{3}\mathbf{4}_{TSH\pi}$	1.77	1.12	1.74	117.0
	$^{5}\mathbf{4}_{TSH\sigma}$	1.77	1.17	1.49	155.8
	$^{5}\mathbf{4}_{TSH\pi}$	1.77	1.13	1.65	115.0
5	$^{2}\mathbf{5}_{TSH\pi}$	1.72	1.16	1.51	122.2
	$^{4}\mathbf{5}_{TSH\pi}$	1.87	1.25	1.37	116.0

Much as found in the experiments that it is very challenging to isolate and characterize iron(VI)oxo complexes, complex **3** displays the highest reactivity of all iron–oxo complexes under investigation. Based on our B3LYP calculations, the hydroxylation of ethane by complex **3** is completely barrierless. We carried out careful relaxed-surface scan calculations in which the distance between the oxo and H–atom in the cleaving C–H bond is stepwisely decreased to let the substrate gradually approach to the Fe=O active center. However, it turned out that the H–atom from the second CH_3 group of the substrate can be directly abstracted even when the target O–H bond has a rather long distance (1.42 Å) and the rebound step can take place immediately after the abstraction. Therefore no transition states and intermediates can be located for this process.

4.3.2.2 Iron–nitrido complexes

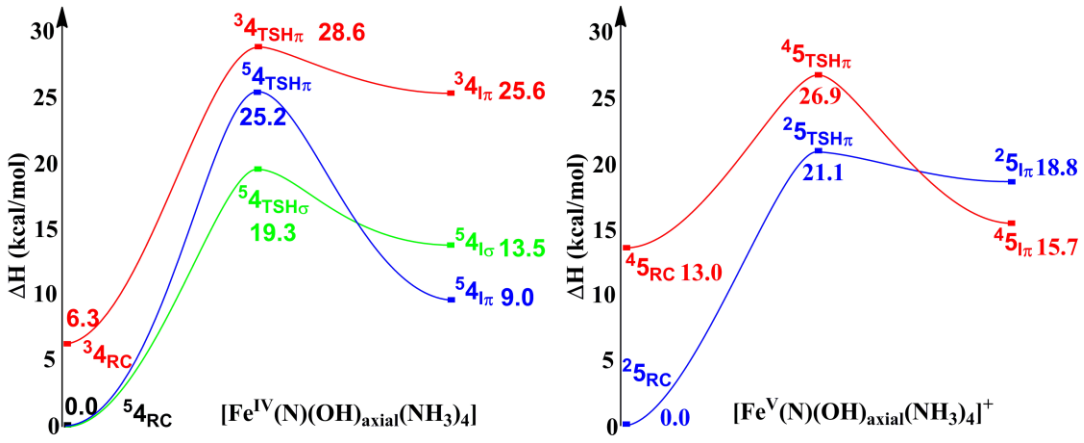

Figure 4. 5 Schematic Gibbs free energy (ΔG) surfaces for the ethane C-H bond activation by the [Fe^{IV}N(OH)(NH$_3$)$_4$] (4) and [Fe^{V}N(OH)(NH$_3$)$_4$]$^+$ (5) systems.

For the reaction with complex **4**, three reaction pathways have been established for **4**, one π–mechanism pathway for triplet and quintet state respectively and one σ–mechanism for quintet state. The calculated energy barriers for hydrogen–atom abstraction demonstrated the similar trends found in the corresponding processes of complex **1**, that quintet σ–pathway encounters by far the lowest barrier among the three alternatives, and the π–pathways on the triplet and quintet surfaces have comparable energy barriers. As the same electron transfer steps established for the three pathways in complex **1**, here too, the two π–pathways involve a β–electron transfer from the substrate to the Fe–d_{xz} based orbital, which is consistent with a horizontal approach of the ethane molecule towards the Fe–N moiety as indicated by a significant bent Fe–O–H angle close to 120° computed for ^{3}**4**$_{TSH\pi}$ and ^{5}**4**$_{TSH\pi}$ (Figure 4.6). While for the quintet σ–mechanism, the antiferromagnetically coupled HS Fe(III) ion (S_{Fe} = 5/2) and the three–center C–H–N radical (S_{CHN} = 1/2) clearly demonstrate an α–electron transfer from the substrate to the virtual d_{z2} orbital.

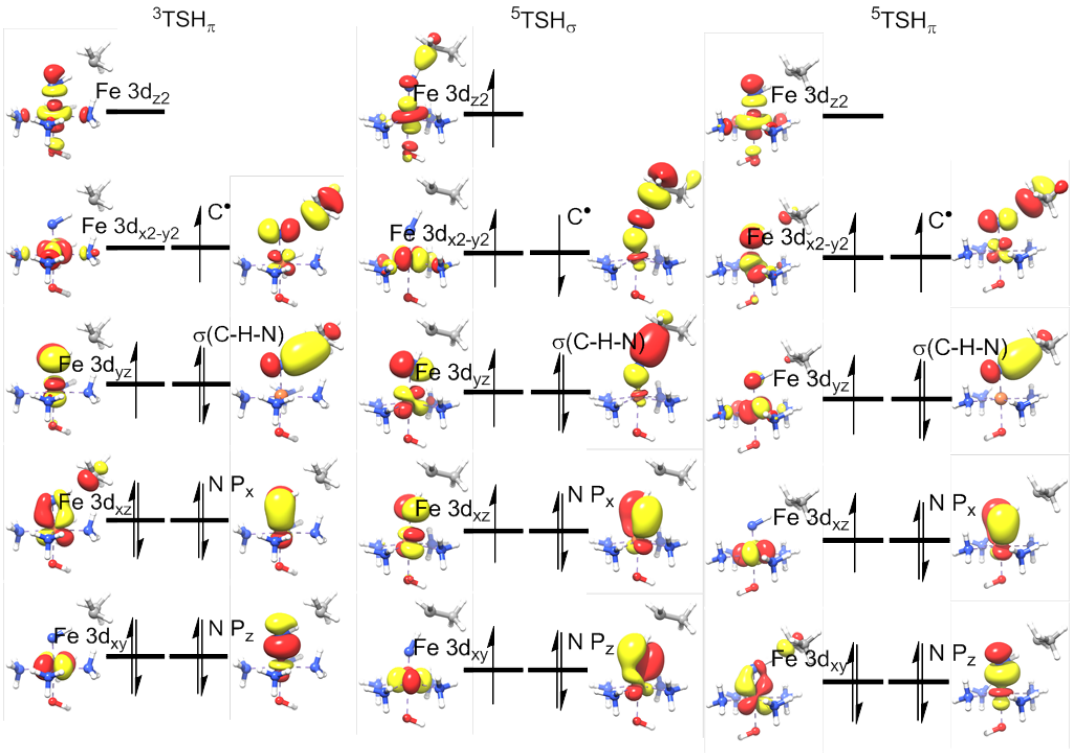

Figure 4. 6 Schematic MO diagram of $^3TSH_\pi$, $^5TSH_\sigma$ and $^5TSH_\pi$ for $[Fe^{IV}N(OH)(NH_3)_4]$ (4). C grey, N blue, O red, Fe orange.

The computed energy profile of C–H bond activation by complex **5** is also shown in Figure 4.5. All the energy are quoted relative to the *S* = 1/2 spin ground state. The quartet state lies about 13 kcal/mol above the doublet congener. Therefore, this species cannot be prepared in laboratory, in agreement with the experimental finding that all reported Fe(V)N complexes have doublet ground states.[148] Surprisingly, unlike the reactivity enhancement from complex **1** to **2** with the increasing oxidation state of the metal center from IV to V, DFT calculations suggest very sluggish reactivity of complex **5** compared with **2** which is evidenced by both unfavorable kinetic and thermodynamic characteristics of the reaction. The reaction requires activation energy of 21.1 kcal/mol and is endergonic by 18.8 kcal/mol on doublet state surface, far more away from the much lower energy barrier (4.0 kcal/mol) and exothermic property (–7.0 kcal/mol) of the reaction with complex **2**. The hydrogen-atom abstraction also associates with a linear transition state, but occurs very late. In $^2\mathbf{5}_{TSH\pi}$, the C–H bond is essentially broken (r(C–H) =1.51 Å), while the N–H bond is very close to their normal bond length (r(N–H) =1.16 Å). The H–atom abstraction step also follows the π–mechanism as established for the iron(V)oxo analog. As shown in Figure 4.6, it is an α–electron from the substrate shifted towards the π*(FeN) antibonding orbital. Again, the calculated geometric structures also support this, i.e., relatively smaller Fe–O–H angles (~120°) are found in the transition states $^2\mathbf{5}_{TSH\pi}$.

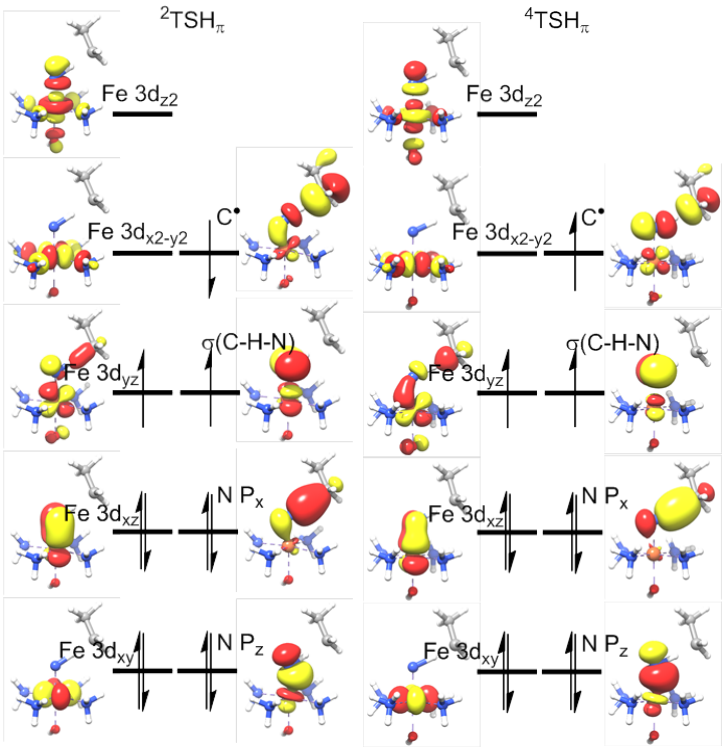

Figure 4. 7 Schematic MO diagram of $^2TSH_\pi$ and $^4TSH_\pi$ for $[Fe^VN(OH)(NH_3)_4]^+$ (5). C grey, N blue, O red, Fe orange.

Unlike the powerful oxidation ability of iron(VI)–oxo complex **3** which leads to the conversion of ethane to ethanol barrierless, the corresponding iron(VI)–nitrido complex **6** appears uncapable of ethane oxidation. First, singlet is the ground state and the triplet state ^{3}**6** lies in very high level energy relative to ^{1}**6** (25.6 kcal/mol). Second, there is no reaction detected for the ground state ^{1}**6** by our B3LYP calculation. Relaxed surface scan indicated that the H–atom is quite reluctant to get close to the Fe=N active center and the energy for the approach to the $(FeN)^{3+}$ unit keeps rising. All attempts to locate the transition state also failed and revealed that the H–atom back transfer to the $CH_3CH_2^\bullet$, even when the N–H bond distance is very short (1.10 Å) in the initial structure.

To well understand the different reactivity of these iron-oxo and –nitrido complexes, we summarized the most feasible pathway of ethane H-tom abstraction by complexes **1** – **6** in Figure 4.8. Clearly, the energy barriers for C–H bond activation by **1** – **6** exhibit interesting trends. First, iron–nitrido complexes are not as reactive as their oxo counterpart. For instance, the H-atom abstraction by complex **4** undergoes a much higher energy barrier than the corresponding one by **1,** the same holds true for the comparison of the reactivity between complex **5** and **2** (Figure 4.8). Second, quite opposite reactivity trend are observed for iron–oxo and –nitrido series upon increasing the iron oxidation state from IV to VI. For the oxo complexes **1** – **3**, the reactivity is enhanced as the oxidation state of the

iron center increases and show the following trend: **1** < **2** << **3**. As shown in Figure 4.8, the energy barrier for complex **2** is lowered by 12.6 kcal/mol compared to that of **1**. Moreover, complex **3** undergoes the barrierless H-atom abstraction process and hence displays the highest reactivity of all iron complexes. This is in good agreement with the experimental results that it is very challenging to isolate and characterize iron(VI)oxo complexes.[223,224,229] However, turning now on the reactivites of the iron–nitrido series, an opposite trend was observed displaying the following order: **4** ≥ **5** > **6**. Unlike the iron-oxo complex **1** – **3**, the iron-nitrido congeners **4** – **6** demonstrate comparable reactivity between **4** and **5** and extremely reduced reactivity for complex **6**. It turns out that complex **6** appears to be incapable of oxidizing ethane.

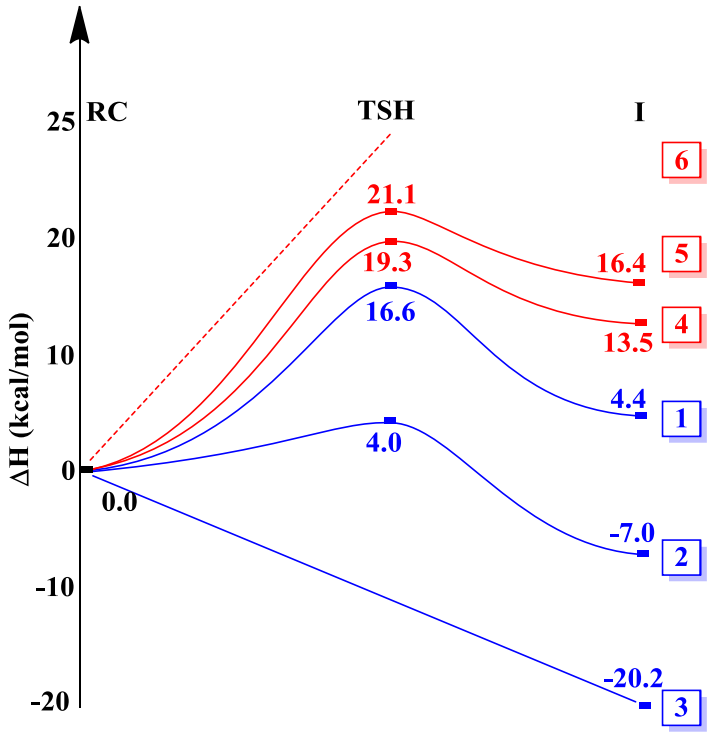

Figure 4. 8 Schematic energy profiles (ΔH) for most feasible pathway of ethane H-tom abstraction by complexes 1 – 6.

4.4 Discussion

As established for iron(IV)-oxo complexes, the real active species toward C-H bond activation is Fe^{III}-$O^{\bullet-}$ which carries a radical character on the abstracting oxygen atom.[85,216] In the iron-nitrido series, due to the inverted bonding character the Fe=N moiety would closely resemble the reactive species found in iron(IV)-oxo complexes. We would therefore expect a higher reactivity of iron-nitrido series. However, this is not the case. Moreover, we might also expect an increased reactivity upon going from **4** to **6** from our

perceptual intuition since the increased formal charge would result in a more powerful electrophlies. In fact, the opposite trend was observed again. Then the questions arise: why do the iron-nitrido complexes exhibit much lower reactivity compared with that of iron-oxo analogues? What drives the quite different reactivities of H-atom abstraction between the two series?

Table 4. 3 B3LYP Calculated Reaction Energies (kcal/mol) and Bond Dissociation Energies (kca/mol) for the Most Feasible Reaction Pathway of Iron-Oxo and -Nitrido Complexes.

	ΔH	$BDE_{FeE-H(E=O/N)}$	ΔBDE_{FeE-H}
1	4.4	94.7	0.0
2	-7.0	110.2	15.5
3	-20.2	123.9	29.2
4	13.5	86.0	-8.7
5	16.4	85.6	-9.1
6	~	86.8	-7.9

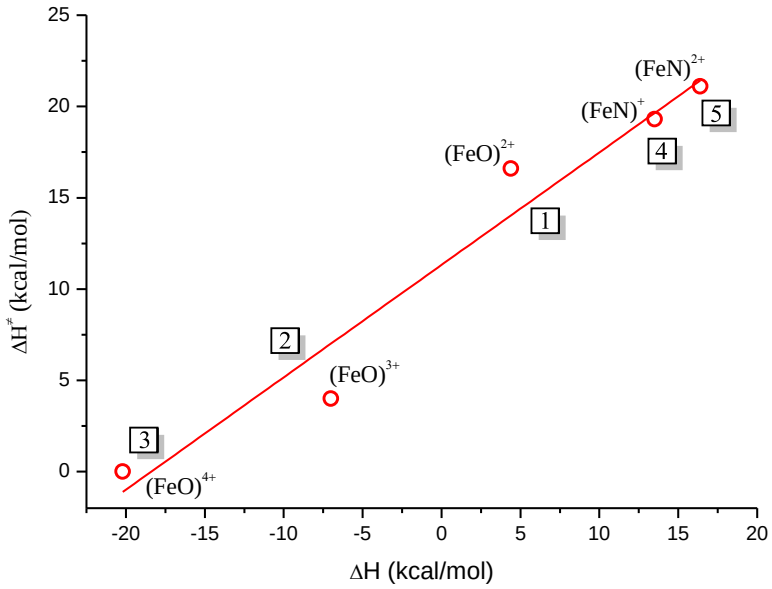

Figure 4. 9 Plots of the reaction energy barrier ($\Delta H^{\ddagger}$) for the reaction with 1 – 5 as a function of the driving force (ΔH).

A direct clue from the PESs is the dramatically different thermodynamic driving force of the reaction. We collected the reaction energies for the most feasible reaction pathways of title reactions in Table 4.3. Note that the six oxidants shown in Table 4.3 span a range of almost 40 kcal/mol differences in the driving force, indicating that the driving force is indeed a quite important factor for modulating the reactivity. Remarkably, we also found a rather good correlation (R^2 = 0.94) between the driving force and the energy barrier for

the most feasible pathway of **1** – **5**, viz. the calculated barrier heights for H–atom abstraction increases roughly linearly with the decreasing driving forces (Figure 4.9).[132,235] This is in good agreement with the previous research that Polanyi analysis can be applied not only to the one abstractor with a series of substrates but also to one substrate with a series of "similar" abstractors.[236]

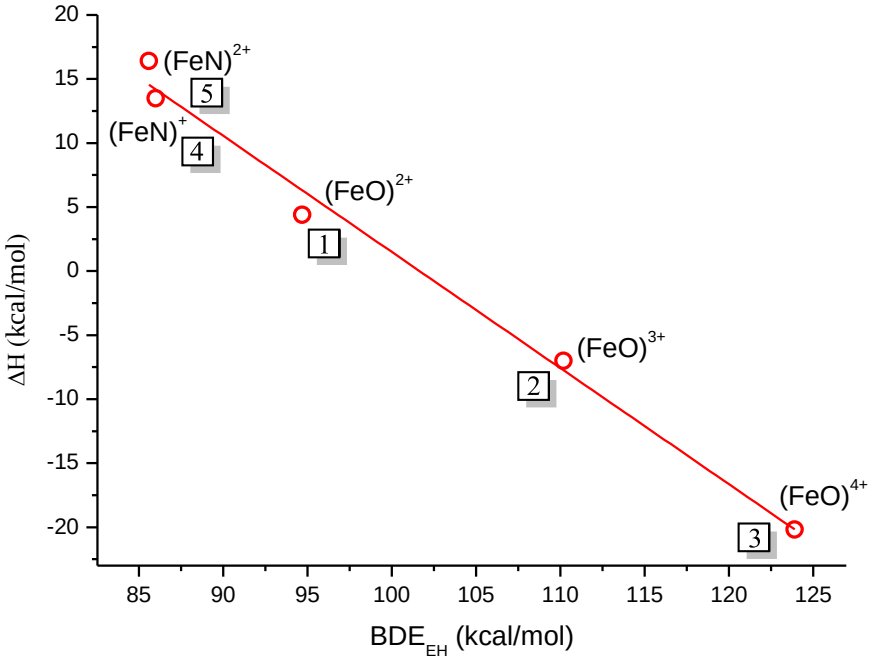

Figure 4. 10 Correlation between reaction exothermicity with BDE$_{EH}$.

In the current research, since the substrate is the same, the underlying factors for the dramatic different driving force must be due to the differences in the relative stability of the FeE–H (E = O, N) products with respect to their Fe=E reactants. Indeed a plot of the reaction energy (ΔH) for formation of the radical intermediates from the reactants gives a linear correlation with BDE$_{EH}$ (Figure 4.10) with a slope close to unity and a correlation of R^2 = 0.98. In the case of iron–oxo complexes **1** – **3**, the increased oxidation state of iron center induces to form strong O–H bonds in the Fe–OH products as evidenced by the enhanced BDE$_{OH}$ values. Compared with the energy required for the C–H bond rupture of the substrate, –104.3 kcal/mol, the reaction of H–atom abstraction catalyzed by **1** is moderately endothermic, while those by **2** and **3** are highly exothermic. Thus, different thermodynamic driving force nicely explains the observed relative reactivity of iron–oxo complexes (**1** – **3**) towards C–H bond cleavage. However, in the iron–nitrio series N–H bonds in the FeN–H products were predicted to be rather weak. The calculated BDE$_{NH}$ values are nearly identical (~86 kcal/mol) irrespective of the oxidation state of the metal center. This value is much lower than the corresponding BDE$_{OH}$ value for iron–oxo series, especially for the Fe^{V}N and Fe^{VI}N compounds. More importantly, the calculated BDE$_{NH}$ values for **4** – **6** are by far lower than the BDE$_{C–H}$ value of the substrate. Therefore, the

energy gained from the N–H bond formation cannot compensate the energy penalty for the target C–H bond scission, thereby rendering the reactions with the iron–nitrido complexes strongly endothermic.

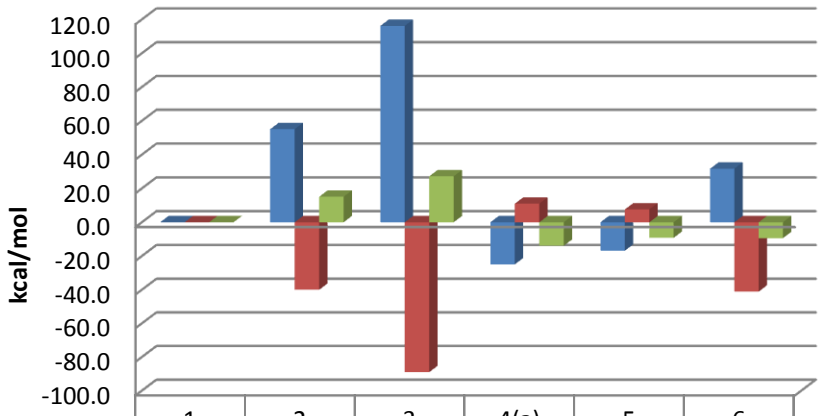

	1	2	3	4(a)	5	6
EA	0.0	55.1	116.2	-24.9	-16.8	31.7
PA	0.0	-40.0	-89.0	11.0	7.6	-41.1
H· affinity	0.0	15.1	27.2	-13.9	-9.2	-9.4

(a) the EA calculation for quintet state of **4** proved problematic. The model complex falls apart when transfer one electron to its d_{z2} orbital. Therefore, we put the calculated EA and PA values for triplet state for comparison. Based on the information of triplet and quintet state for complex **1** (EA: -19.2 *vs* 0, PA 13.6 *vs* 0 for triplet and quintet respectively), we deduced that quintet state should have relatively lager EA and smaller PA values than its triplet counterpart.

Figure 4. 11 B3LYP Calculated Relative Adiabatic Electron and Proton Affinity for most feasible reaction pathways of Iron-Oxo and -Nitrido Complexes.

Although the Polanyi correlation provides a rationale for the observed reactivity, that is, iron-oxo complexes are reactive because they can form a strong bond to a hydrogen atom, while iron-nitrido complexes react several orders of magnitude slower than iron–oxo complexes because the rather weak N-H bonds were formed, the original factor that responsible for the bond strength of Fe_{E-H} variation still hung in the air. To quantitatively understand the questions mentioned above, the first parameter that should be considered is the thermochemical affinity of the oxidant for $H^{\bullet}$.[134] This is most easily obtained from its electron and proton affinity component. Figure 4.11 collects the calculated relative adiabatic electron affinities of Fe^{n+}=E (E=O,N) and proton affinities of its reduced form $[Fe^{(n-1)+}=E]^{-}$. First, the calculated EA and PA values demonstrate the quite different properties of oxo and nitrido complexes. For the same oxidation state of the iron center, e.g. **1** *vs* **4**, oxo species has much higher oxidizing power than its nitrido counterpart and moderately decreased basicity for its one-electron reduced form. This

can be readily ascribed to the one unit positive charge decrease in iron-nitrido series by replacing the oxo group with nitrido moiety. This leads to much stronger O–H bond than the corresponding N–H bond. For the species with same formal charges, i.e **1** *vs* **5** or **2** *vs* **6**, the same holds true. As shown in Figure 4.11, the EA values for **5** and **6** are still below those for **1** and **2**, respectively. We attribute this to the inverted bonding character in iron-nitrido series which renders complexes **4** – **5** do not contain high-valent iron, but rather more "mundane" oxidation state for iron.

Second, the calculated different BDE_{FeE-H} values for the two series can be understood by these two tunable parameters. For the two series, an increased EA value concomitant with a decreased PA value for its reduced form is found upon the iron oxidation state increasing from IV to VI. That's to say, the increased iron oxidation state not only increases the oxidation power of oxidant Fe^{n+}=E, but also significantly decreases the basicity of its reduced form $[Fe^{(n-1)+}=E]^{-}$. Therefore, the final $H^{\bullet}$ affinity is determined by the interplay between these two factors. For the iron-oxo series, the increase of the EA value far exceeds the extent for PA decreasing, that is $|\Delta\Delta EA| >> |\Delta\Delta PA|$. Therefore, a strengthening O-H bond in the iron-oxo series is formed upon the increased iron oxidation state, i.e $BDE_1 < BDE_2 < BDE_3$. In other words, the large increase in BDE_{OH} of iron-oxo series must arise from a substantial increase in electron affinity of Fe^{n+}=O upon increasing the iron oxidation state from IV to VI. For the nitride series, however, although generally the same EA and PA variation trends are found as in oxo series, the degree of the increase in EA and decrease in PA is roughly equal, i.e $|\Delta\Delta EA| \approx |\Delta\Delta PA|$, and therefore leading to BDE_{NH} of nirtido series close to a constant, $BDE_4 \approx BDE_5 \approx BDE_6$.

Overall, this stepwise analysis, which corresponds to sequential movement of electron and proton, provides a basis for enhanced understanding of nature's BDE_{EH} in iron–oxo and –nitrido complexes. The over-reduced oxidation power together with moderate increased basicity well rationalize the weaker N–H bond formed in nitrido series compared to the O–H bond in oxo complexes.

4.5 Conclusions

Six "hypothetic" iron complexes have been studied to investigate the determinant factor for controlling the oxidative C-H bond cleavage by iron–oxo and –nitrido complexes. DFT calculations demonstrated that although quite opposite reactivity is obtained for these two series, a good correlation between the driving force and the energy barrier is established, in close agreement with the Polanyi principle. More importantly, a close inspection of the thermochemical $H^{\bullet}$ affinity, which determined by its electron and proton affinity component, showed that the iron–oxo and –nitrido complexes have quite different properties. The oxo complexes have significant stronger oxidation power than their nitrido counterpart, while the nitrido complexes have relatively larger basicity

inverse. Additionally, the counterintuitive reactivity of these two series also can be well understood by the separate EA and PA analysis. The gradually increased reactivity in oxo series is ascribed to the substantial increase in oxidation power, while the offset of the EA and PA functions in nitrido series leads to BDE_{NH} to be a constant.

5. Differences in and Comparison of the C-H Bond Oxidation Activity by Diiron Complexes with Diamond Core or Open Core Structures: A DFT Study

5.1 Introduction

The functionalization of unactivated C–H bonds is fundamentally important to life and immensely useful in industry.[3,87,127,237] In biology, a range of metalloenzymes achieve this challenging task using dioxygen as a "green" oxidant.[3,8,13,34,51,238] These enzymes have evolved to efficiently perform these transformations under ambient conditions. More importantly, metalloenzyme-catalyzed oxidation exhibits exquisite substrate specificity as well as regioselectivity and/or stereoselectivity. Therefore, unveiling the nature of active species and the mechanistic details of reactions catalyzed by metalloenzymes might allow us to gain atomic level insights into the reactivity of enzymes, and could also shed light on synthesizing new reagents that can modify target C–H bonds with high efficiency and specificity.

Of O_2-activating metalloenzymes, soluble methane monooxygenase (sMMO) deserves a particular attention,[34,86] because this enzyme oxidizes methane, which has the strongest C-H bond of all hydrocarbons, to methanol.[239] In the reaction circle, the intermediate called **Q** prior to methane oxidation has been trapped and characterized with various spectroscopic methods.[240-244] The experimental findings suggest that intermediate **Q** contains a di(μ-oxo)diiron(IV) diamond core, in which two high-spin (S = 2) Fe^{IV}=O units are antiferromagnetically coupled.[41] Related diiron(IV) intermediates have also been proposed as key oxidants in the catalytic circle of fatty acid desaturases and other diiron enzymes.[245-247]

However, the mechanism for the hydroxylation of methane by intermediate **Q** is not yet fully understood. In light of the recent studies of model systems, the proposed geometric structure of **Q** may need to be reconsidered.[34,248] Experiment revealed that although the oxidizing power of the diamond core model complex [Fe^{IV}–$(O)_2$–Fe^{IV}] (**2** in Scheme 1) is slightly higher than its one-electron reduced form [Fe^{III}–$(O)_2$–Fe^{IV}] (**1** in Scheme 1) toward 9,10–dihydroanthrocene (DHA) C–H oxidation, it is far below that of the related mononuclear S = 1 ferryl complex.[40,78] In line with this, the open core analogue [OH–Fe^{IV}–O–Fe^{IV}=O] (**3** in Scheme 1) with a terminal S = 1 Fe(IV)=O moiety exhibits C–H bond activation reactivity that is approximately 3 order of magnitude higher than complex **2**.[249] The latest synthesized open core analogue [OH–Fe^{III}–O–Fe^{IV}=O] featuring an S = 2

Fe(IV)=O unit (**4** in Scheme 1) displays even higher reactivity toward C–H bond oxidation.[250] This is consistent with the theoretical predication that the quintet ferryl species is more aggressive oxidant than its triplet counterpart. By contrast, experimentally intermediate **Q** was found to be extremely reactive towards alkane C–H bond activation, but no self-oxidation damage to the protein has been detected. Thus, one might suggest that intermediate **Q** may first adopt a more thermodynamically stable geometry in the absence of the substrate, such as a "diamond core", to protect the enzyme from self-destruction and then transform to an open core structure to effect C–H bond activation. Experiment also provides the support for this notion. In the reaction of cyclohexane hydroxylation by a stable Fe^{III}–O–Fe^{III} species, the spectroscopic evidence showed that C-H bond oxidation is in fact carried out by a $Fe^{II}Fe^{IV}$=O intermediate with a terminal Fe^{IV}=O motif, which is generated by isomerization of the original diiron(III) reactant upon substrate approaching.[251-253] In another example, Xue et. al have also demonstrated that the sluggish diamond core [$Fe^{III}Fe^{IV}(\mu\text{-}O)_2$] oxidant can be activated by binding of hydroxide or methoxide to form an open core [X–Fe^{III}–O–Fe^{IV}=O] adduct which exhibits reactivity rapidity of 3.6×10^7-fold higher.[248]

Density functional theory (DFT) calculations have also raised the possibility of isomerization of **Q**. Siegbahn and Crabtree's study demonstrated that the highly asymmetric Fe^{IV}–$(O)_2$–Fe^{IV} bridges may easily open up to a key Fe^{III}–O–Fe^{V}=O intermediate that is shown to be capable of reacting with methane via a lower-energy transition state.[254] In a QM/MM study, Friesner and co-workers suggested that the electronic structure of **Q** is particularly sensitive to the chemical environment and a diiron(III,V) core is likely to coexist with the diiron(IV) unit in protein environments.[255] Quantum chemical studies have also contributed to the understanding of the mechanism of methane hydroxylation by sMMO.[34,86-90] However, due to the lack of unambiguous structure for the active site of intermediate **Q**, different models have been proposed in the mechanistic study.[88-97] The first model was proposed by Yoshizawa in which the catalytically active diiron center is treated as analogue to the $Fe{=}O^+$ ion.[88-90] Mechanistically, the modeling follows a nonradical mechanism in which the coordinately unsaturated iron center is a direct participator in C–H bond activation.[99,256,257] The other three models, Morocuma-Basch,[91] Siegbahn,[92-94] and Friesner-Lippard,[95-97,258] are known that the C–H bond oxidation takes place at the bridging oxo ligand and follow the typical oxygen rebound mechanism. All these studies have provided vital insights into the mechanisms of catalysis and a precise molecular-level picture of intermediate and transition-state structures, their energies, and electronic details of the mechanism. In the present study, we carry out detailed theoretical study on the reactivity of four biomimetic complexes shown in Scheme 1. Our main aim is to explore the different reactivity of complexes **1** – **4**. Clarifying the factors that dictate the different reactivity of these complexes will provide a

comprehensive theoretical framework in which the preference of the terminal Fe^{IV}=O unit and the high-spin state of iron(IV) center in C–H activation can be appreciated. The insights obtained are then used to understand the reactivity of intermediate **Q**.

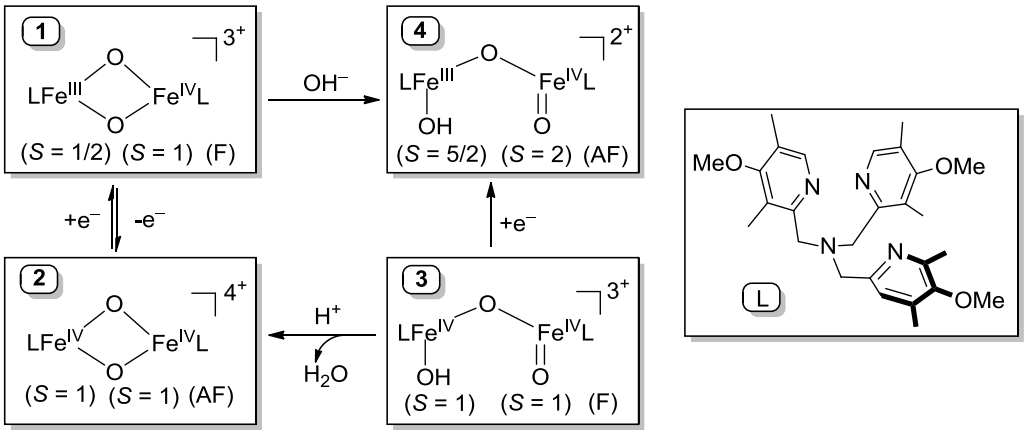

Scheme 5. 1 Scheme 5.1. Core structures and supporting ligand of complexes 1–4, F, ferromagnetic; AF antiferromagnetic.

5.2 Computational details

A. See **2.7 Calculations set up**

5.3 Results and discussion

5.3.1 Geometric and Electronic Structures of Complexes 1 – 4.

To understand the different C-H bond oxidation reactivity of complexes **1** – **4**, one has to analyze their geometric and electronic structures into some detail. The computed geometries of complexes **1** – **4** are shown in Figure 5.1, along with the spin population of the key atoms in the core structure. In order to save computational time, the OMe substituents on the TPA ligand (TPA = tris(2-pyridylmethyl)amine) (Scheme 5.1) were replaced by H-atoms. Geometrically, the iron sites of **1** – **4** are bridged by two (**1** and **2**) or one (**3** and **4**) oxo ligands and adopt approximately a pseudooctahedral local coordination geometry. For **1** and **2**, the diamond core structure results in relatively compressed Fe-O-Fe angles (94.5 – 97.0°) and short Fe···Fe distances (~2.74 Å). The optimized geometry of **1** overall matches the crystal structure of $[Fe^{III,IV}_2(\mu\text{-O})_2(5\text{-Et}_3\text{-TPA})_2]^{3+}$.[259] B3LYP calculations predict two different sets of the Fe–μ-O bond lengths for the two iron center (1.79 and 2.02 Å for Fe1 vs. 1.70 and 1.86 Å for Fe2). This indicates that **1** is a valence-localized mixed valence complex with the two ferromagnetically coupled iron sites (S_{Fe1} = 1/2, S_{Fe2} = 1), in contrast to the valence-delocalized diiron core suggested by Mössbauer

spectroscopy.[260] The calculated structure of **2** exhibits an approximately centrosymmetric $Fe_2(\mu\text{-}O)_2$ rhomb core, in consistent with its electronic structure description of an antiferromagnetically coupled pair of intermediate-spin iron(IV) centers. The calculated Fe–oxo bond and Fe···Fe distances are in reasonable agreement with the EXAFS-derived value for complex **2**.[40] In the case of the open core complexes **3** and **4**, the calculated Fe–μ-O–Fe angles and Fe···Fe distances are substantially greater than those computed for **1** and **2**,[261,262] a consequence of breaking the rigid diamond core structure. The predicted terminal Fe-oxo bond distances are essentially identical irrespective of the spin state of the iron(IV) center,[207] and are comparable with those found in the crystal structures of mononuclear ferryl model complexes.[6,85,114,125,195,205,216] The bridging oxo ligand in **3** mediates a ferromagnetic interaction between the two intermediate-spin Fe^{IV} sites, while its one electron reduced form, **4**, possesses high-spin Fe^{III} and Fe^{IV} sites that are antiferromagnetically coupled.

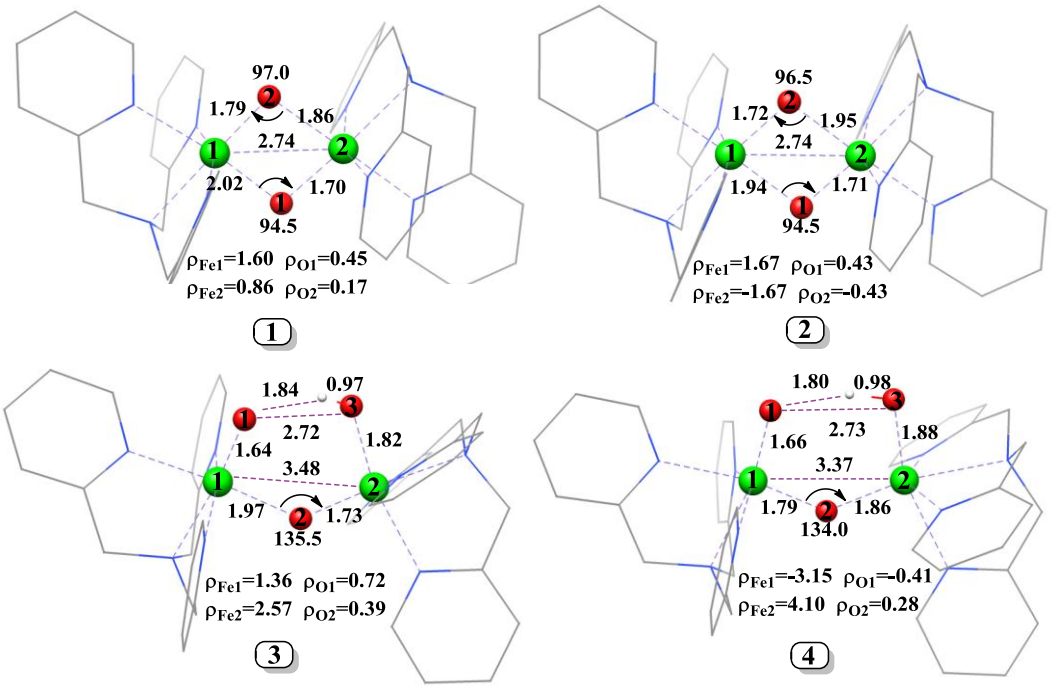

Figure 5. 1 B3LYP optimized structures and spin populations of key atoms in core structure for complexes 1 – 4. Fe green, O red, N blue, C grey, H white.

5.3.2 Reactivity

Figure 5.2 demonstrates the potential energy surfaces (PES) of DHA C–H bond activation by complexes **1** – **4** (Figure 5.2a), and the comparison between the calculated and experimental rate constants (Figure 5.2b). Our calculations generally well reproduce the reactivity trend observed experimentally, progressing from complex **1** to **4**, the computed

barrier decreases and follows the order **1** < **2** < **3** < **4**.[250] Specifically, the activation energy for complex **2** is 2.3 kcal/mol lower than that of its congener **1**, in reasonable agreement with the experimental finding that **2** is ~10 times more reactive than **1** in oxidizing weak C-H bonds. Likewise, there is a decrease of 4.1 kcal/mol in the energy barrier for **3** relative to **2**, this value also corresponds well to the 300-fold difference in their reaction rates. However, our calculations may underestimate the reaction barrier for **4** and hence predict much higher reactivity as compared with experiment (Figure 5.2b).

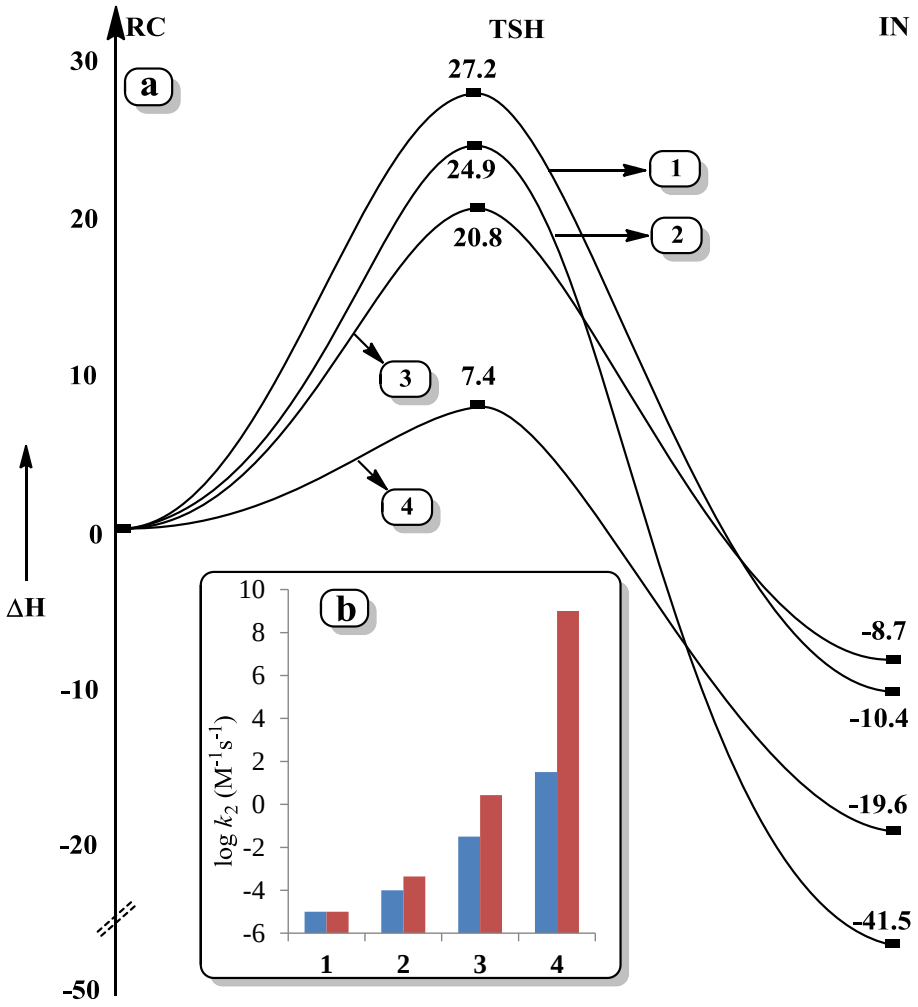

Figure 5. 2 Potential energy surfaces for DHA C–H bond oxidation by complexes 1 – 4, and the comparison of rate constants obtained from experiments and DFT calculations. The blue bars represent experimental reaction rates, whereas the red bars correspond to the calculated relative rate constants using 1 as reference.

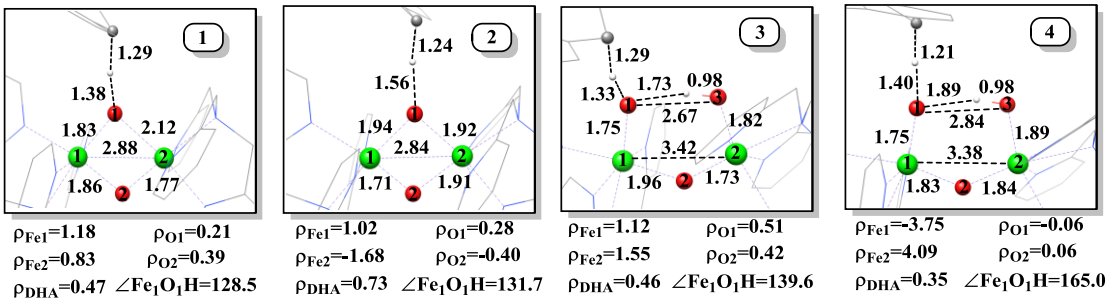

Figure 5. 3 B3LYP calculated transition state structures and spin populations for the key atoms. Fe green, O red, N blue, C grey, H white.

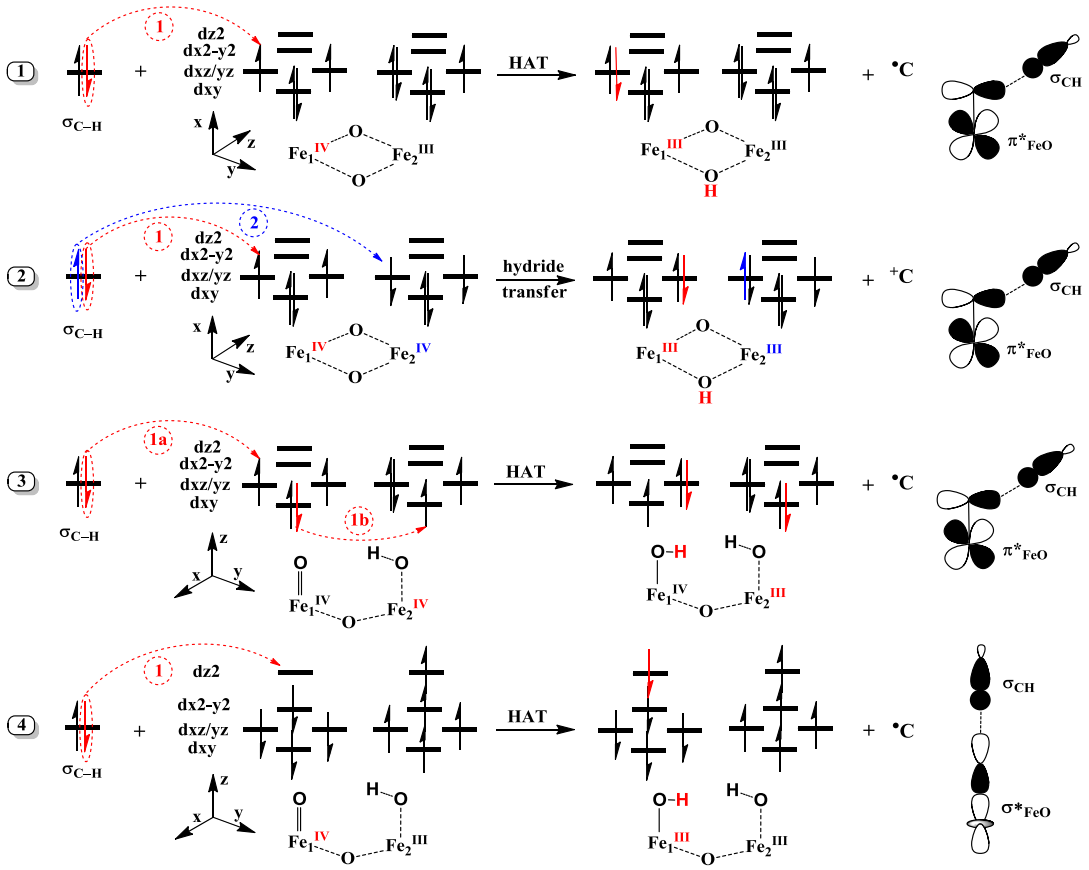

Scheme 5. 2 Orbital occupancy-evolution diagrams during C-H bond oxidation and the corresponding orbital-selection rules for predicting transition state structures.

In fact, the mechanisms by which complexes **1** – **4** oxidize C-H bond are different. The reactions mediated by **1**, **3**, and **4** only involve $1e^-$ and $1H^+$ transfer in a single kinetic step, characteristic of an H-atom transfer (HAT). By contrast, in total a hydride transfer pathway is operative for the reaction with **2** (Scheme 5.2). By comparison of the spin populations of the substrate in the transition states of complexes **1** – **4** (Figure 5.3), one can easily appreciate that the electron transfer has been nearly completed for **2**, while only partial

electron transfer occurs for the other systems. The decay of the transition state of **2** is accompanied with the second electron transfer to the other Fe^{IV} center (Figure 5.4). The difference in the reaction mechanism can be ascribed to the fact that complex **2** has the highest electron affinity of all systems and contains two antiferromagnetically coupled ferryl centers. For the latter, otherwise, the second electron transfer is spin forbidden. For **3,** the H-atom abstraction by the terminal Fe^{IV}=O unit is concomitant with the electron transfer between the two iron centers (Scheme 5.2 and Figure 5.5). This reflects that the potential electron accepting orbitals at the Fe^{IV}–OH site are lower in energy than those at the Fe^{IV}=O moiety. In line with this, the additional electron for the one-electron reduced form of **3** was found to reside at the Fe-OH unit. Thus, both iron(IV) centers of **3** involve in the HAT, Fe^{IV}=O functions as a proton accepting site, and Fe^{IV}–OH as an electron accepting site. We also investigated the reaction where the C-H bond oxidation takes place at the Fe^{IV}–OH site. It turned out the transition state is ~3 kcal/mol higher in energy than that with the Fe^{IV}=O moiety acting as the reactive unit. As for C-H bond activation by mononuclear ferryl complexes, the Fe-O-H angle in the transition state is a good structural marker for differentiating different reaction pathways.[6,84,85,89,198,201,216] The bent Fe_1O_1H angles (< 140°) computed for the transition states of complexes **1**, **2** and **3** (Figure 5.3) suggest that the reactions of C–H bond activation by them follow a π–mechanism, in which a spin-down electron in the $\sigma_{C\text{-}H}$ of the substrate is shifted to the half–filled $\pi^*_{(Fe-O)}$ orbital of Fe^{IV}. By contrast, the reaction by complex **4** proceeds with a σ–channel, as indicated by a nearly collinear arrangement of Fe_1O_1H (165.0°). This reaction pathway involves an electron transfer from the substrate to the empty $\sigma^*_{(Fe-O)}$ orbital, in consistent with the considerably increased spin population on the reactive iron center.

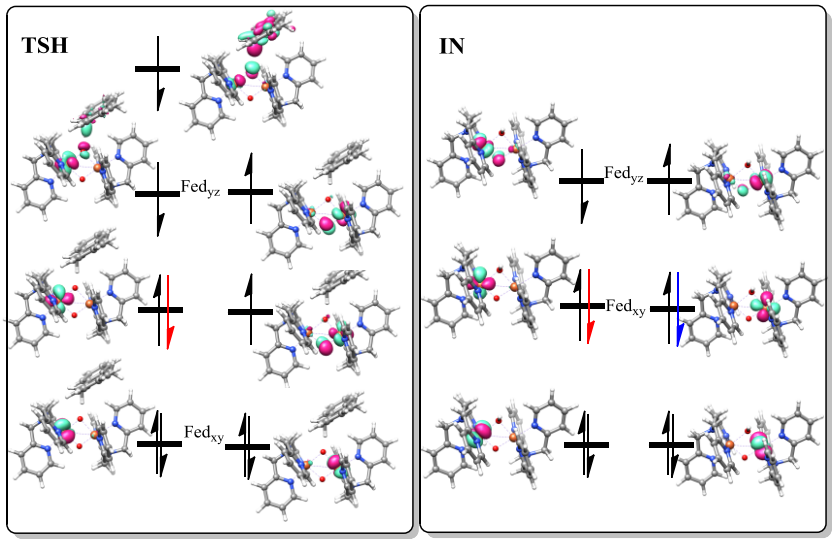

Figure 5. 4 Orbital occupancy-evolution diagrams for C–H bond activation by 2.

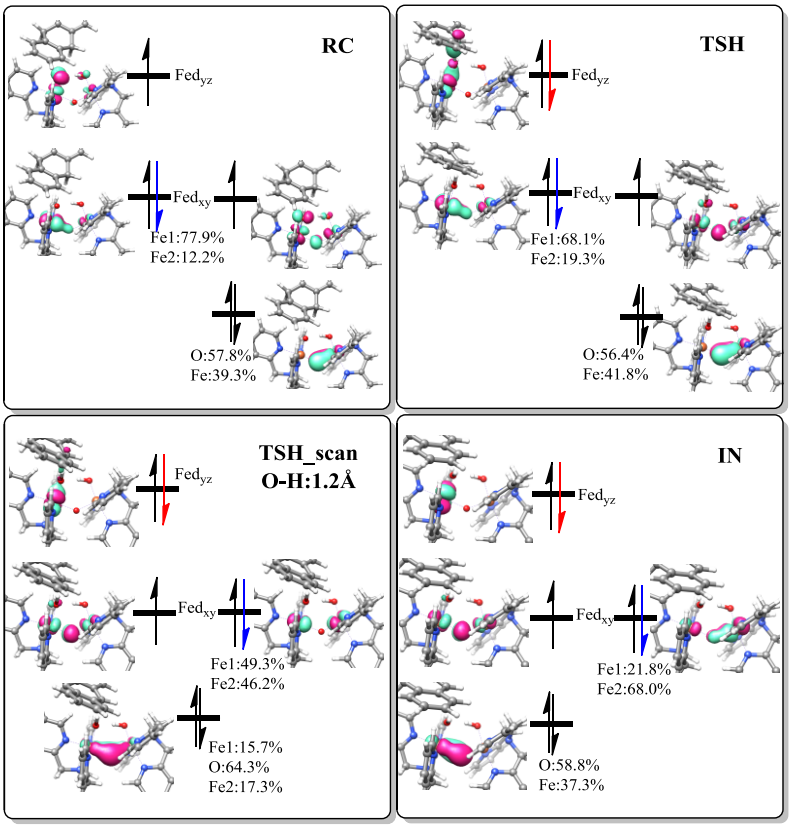

Figure 5. 5 Orbital occupancy-evolution diagrams for C–H bond activation by 3.

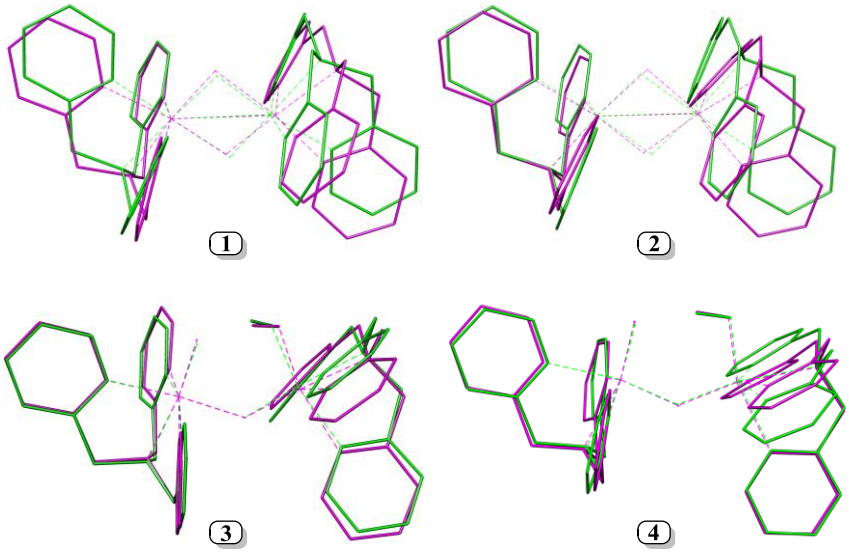

Figure 5. 6 Overlays of the geometries of complex 1 – 4 (green line) and their corresponding transition state (magenta line). For clarity, all hydrogen atoms and the substrate in the transition states are not shown.

5.4 Discussion

As complexes **1 – 4** differ in total charge and geometric and electronic structure, and more importantly, follow different reaction pathways towards C–H bond activation, there could be several factors accounting for their different reactivity. Mayer, however, offered a possible assumption that the distinct reactivity of **1 – 4** may result from differences in the reaction driving force (ΔG°_{HAT}) and/or the intrinsic barrier (λ_{HAT}).[236] In the following discussion, we will firstly analyze the thermodynamic properties of the reactions and then discuss the kinetic considerations with respect to the energetic contributions to the computed reaction barriers.

5.4.1 Reaction driving force.

The thermodynamic driving force is usually assumed to be one of the determinant factors in modulating the reactivity of HAT by metal–oxo catalysts, especially for the mononuclear iron-oxo complexes.[45,65,119,126,134,263,264] However, in the current study, there is no clear correlation between the activation barriers and the reaction energies (Figure 5.2), presumably due to the fact that the different reaction pathways are operative for C-H bond oxidation by complexes **1 – 4.** Even though, analysis of the reaction driving forces sheds some important insights into the reaction mechanism.

Above all, thermochemistry can successfully explain why the C-H bond oxidation by complex **2** favors the hydride transfer channel. As demonstrated in Scheme 5.3, the HAT reaction mediated by complex **2** is exothermic by –14.0 kcal/mol, while the hydride transfer releases much higher energy (41.5 kcal/mol). Therefore, there is a thermodynamic preference of 27.5 kcal/mol for the hydride transfer pathway, this energy renders the second electron transfer occur without any barrier during the decay of **TSH_2**.

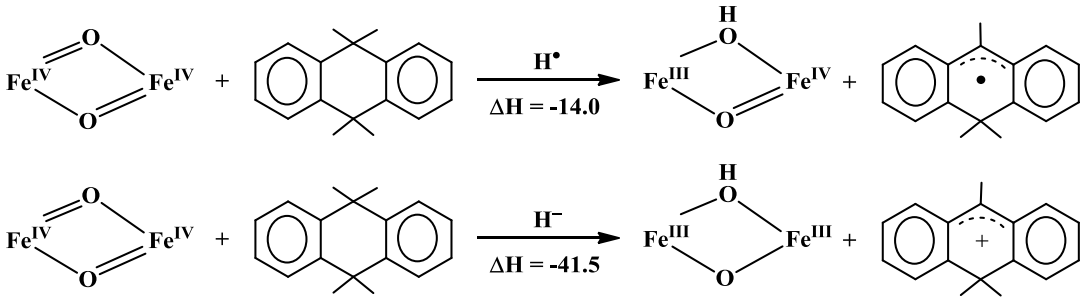

Scheme 5. 3 Comparison of the reaction driving forces of DHA C-H bond oxidation by complex 2 with the different reaction pathways.

For the HAT reactions, the thermodynamic driving force varies with respect to the energy difference between the MO–H bond being formed and the C–H bond being broken. In the

current study, the substrate is the same; therefore, the key parameter that is responsible for the thermochemistry of DHA C–H bond cleavage is the bond dissociation energy (BDE) of the O–H bond in the intermediates (IN). This property is also equivalent to the H-atom affinity of metal-oxo reagents, which is a function of both the redox potential of the M^{N+}=O oxidant and the pK_a of the $M^{(N-1)+}$–OH reduction product based on a thermochemical cycle developed by Bordwell et. al.[133] and others[265-267]. Thus, the oxidizing power of complexes **1** – **4** should be discussed not only within the context of their redox potentials but also the basicity of their reduced form. To address this question directly, we have calculated the relative electron and proton affinity (EA and PA) for complexes **1** – **4** and the BDE_{O-H} values for all INs of HAT choosing **1** as the reference (Figure 5.7).

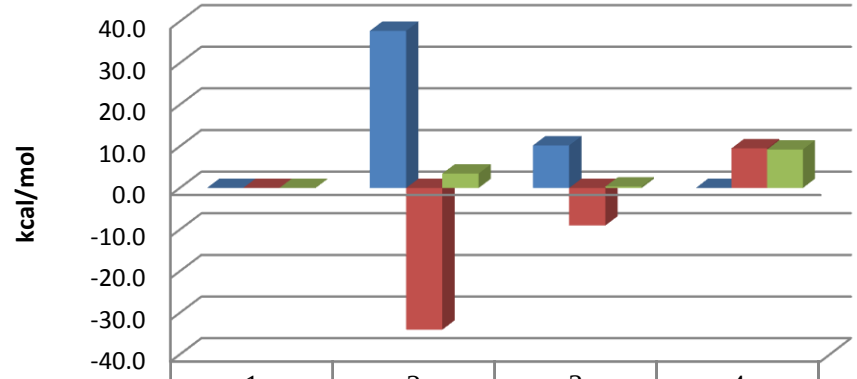

	1	2	3	4
EA	0.0	37.8	10.2	0.0
PA	0.0	-34.0	-9.0	9.5
BDE(O-H)	0.0	3.5	0.3	9.3

Figure 5. 7 B3LYP Calculated Relative Adiabatic Electron Affinities for Complexes 1 – 4, Proton Affinities for Their One-Electron Reduced Form and Bond Dissociation Energies for the O-H Bond of Their Intermediates.

Unexpectedly, the IN of complex **4** is predicted to have the strongest O-H bond among this series. Since complex **4** has the lowest number of the positive charges, one may anticipate that it should have the lowest EA value and the highest PA value of its reduced form. Indeed, the calculations confirm the highest PA value of its reduced form. However, the computed EA value for **4** is identical to that for **1**, although they are differing by 1 unit of the total charge. This can be attributed to the consequence of the enhanced exchange-stability of the high-spin Fe^{III} state.[6,84,85,216] The overall larger BDE_{O-H} of **4** reflects that the basicity of oxo ligands in metal-oxo complexes has important effects on HAT reactivity.[122,135,236] As expected, complex **2** has the highest EA value; however, the dominantly compensating PA value makes its BDE_{O-H} values only ~3 kcal/mol higher than that for **1**. This value is in excellent agreement with the predicted reaction energy of the

HAT by **2** relative to **1** (14.0 kcal/mol for **2** vs. 10.4 kcal/mol for **1**). The computed relative BDE_{O-H} for **3** is comparable to **1,** consistent with their reaction energies (Figure 5.2). The estimated higher EA of **3** relative to **1** may result from their different reorganization energies required for the redox change. As aforementioned, the C–H bond activation by complex **3** finally leads to the reduction of the Fe^{IV}–OH unit rather than the Fe^{IV}=O moiety. It follows that the H-atom affinity of **3** is composed by the redox potential of the Fe^{IV}–OH unit and the proton affinity of the Fe^{IV}=O moiety. Consequently, the calculated reduced basicity in Figure 3 is for Fe^{IV}=O, not for its reduced form Fe^{III}–O. The offset of the EA and PA values finally leads to the essentially equal H-atom affinity between **1** and **3**. However, the HAT reactions by **1** and **3** proceed at vastly different rates; **3** reacts at least 1000 times faster than **1**.

In short summary, thermochemistry has nicely explained the hydride transfer behavior of **2**. Considering the thermodynamics of HAT in term of its component step, i.e., electron and proton transfer, has provided insights into the factors that drive the reaction. Our analysis highlights the importance of both the redox potential and proton affinity in HAT reaction. High redox potential does not necessarily mean high reactivity in HAT (in case of complex **2**) and the strong basicity of oxo ligands may render the metal-oxo complexes being able to oxidize C–H bonds with relative low redox potentials (in case of complex **4**).

5.4.2 Kinetic considerations

More important insights into the distinctive HAT reactivity of complexes **1** – **4** can be gained by dividing the reaction barrier into three energetic contributions: (1) the reorganization of the diiron reagents to accommodate the incoming substrate and the bonding alteration arising from the redox change, (2) the lengthening of the target C–H bond, and (3) the interaction between these two fragments, consisting of the orbital interaction and the Pauli repulsion between them. Figure 5.8 demonstrates the three energetic contributions to the reaction barrier of DHA C–H bond activation by complexes **1** – **4**, as well as the energy barrier calculated with electronic energy (blue line). In the following discussion, we will focus on the electronic energy only, because the corrections originating from the zero-point energy, thermal corrections and entropy term are nearly identical for all systems

Let us first look at the reorganization energy of diiron complexes. The salient feature of this contribution is that the diamond core reagents **1** and **2** are suffered more energetic penalty than the open core complexes **3** and **4** upon redox processes, in line with the transition state geometric distortion discussed above. Specifically, the reorganization energy of **1** is ~5 kcal/mol higher than those for open core complexes, and the structural arrangements of the more rigid diamond core in complex **2** needs much more energy (~8

kcal/mol than those for **3** and **4**). According to Figure 5.8, it is the different reorganization energy between **1** and **3** that leads to their different HAT reactivity. More importantly, the counterintuitive sluggish reactivity of **2** is also ascribed to the highest energetic cost required for the diamond core rearrangements.

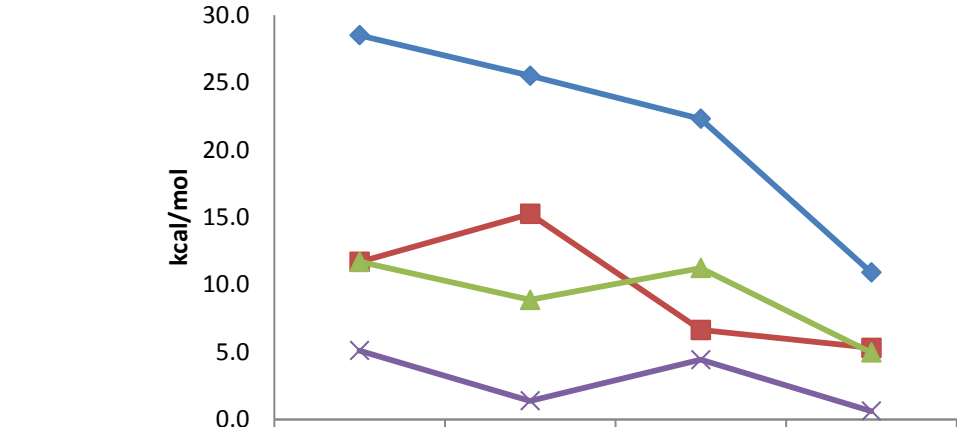

	1	2	3	4
energy barrier E	28.5	25.5	22.3	10.9
diiron reagent	11.7	15.2	6.6	5.3
DHA C-H	11.7	8.9	11.2	5.0
interaction energy	5.1	1.4	4.4	0.6

Figure 5. 8 Three energetic contributions to the reaction barriers for DHA C-H bond oxidation by complexes 1 – 4.

We next consider the distortion energy of the substrate and the interaction energy between the two reagents. These two contributions are closely related to the properties of the transition state. The earlier transition states exhibit relatively less stretched C–H bonds and hence possess lower degree of the substrate distortion. The calculated C–H bond lengths in the transition states follow the order **1** ≈ **3** > **2** > **4**, in good agreement with the computed reorganization energies of DHA (Figure 5.8). Moreover, in the early transition states, $\mathbf{TSH_2}$ and $\mathbf{TSH_4}$, the orbital interaction nearly cancels off the Pauli repulsion, thereby leading to a negligible contribution of the interaction energy to the reaction barrier. While in the case of $\mathbf{TSH_1}$ and $\mathbf{TSH_3}$, the Pauli repulsion outweighs the orbital interaction and raise the energy barrier by 4 – 5 kcal/mol. The highest kinetic facility of **4** stems from the lowest reorganization energy of the diiron core and the substrate. Thus, the quintet σ–pathways are favored not only by the exchange enhanced stability in thermochemistry,[6,81-83,125,190,193,198,216,268] but also a favorable stereochemistry in the kinetic aspect.

To sum up, the kinetic considerations have nicely interpreted the difference in the computed reaction barrier. The larger reorganization energies required for the diamond core structure compared to those for the open core complexes make a primary contribution to their different reactivity. The highest efficiency of the HAT by complex **4** originates from the lowest reorganization energy both for the diiron reagent and for the substrate.

In conclusion, the thermodynamic combined kinetic analysis has nicely rationalized the different reactivity observed for complexes **1 – 4**. Given the high energetic cost arising from the geometry reorganization for the diamond core, the diamond core complexes exhibit reactivities that fall far short of that associated with open core ones. Based on this information, it is very likely that the detected diamond structure **Q** is a resting state in the absence of substrate and then it collapses to a more powerful oxidant, such as an "open core", to proceed the following effective C–H bond activation. This might be one direct theoretical evidence for the notation of core isomerization of **Q**.

5.3.3 The relevance to Marcus Theory

Marcus-Hush theory and its extensions have been remarkably successful in understanding a wide range of electron transfer (ET) processes.[269] Recently, Mayer *et. al*. has elegantly described the use of Marcus framework to evaluate the ability of metal–oxo complexes to cleavage C–H bond, and accuracy in describing HAT reactions is remarkable.[236] The success of the Marcus framework indicates that HAT reaction barriers ($\Delta G^{\neq}$) are primarily determined by two parameters: the reaction driving force (ΔG°) and the intrinsic barrier λ. In the current research, the reaction driving force has been nicely discussed based on the two functions of BDE_{O-H}, i.e., the electron and proton affinity of the metal–oxo diiron complexes. However, the intrinsic barrier λ is not illustrated in the way developed by Marcus,[270] and we have to take the second best to better understand the magnitudes of λ_{HAT}. As noted from extensive experimental database of organic HAT reactions, λ_{HAT} is dominated by the inner-sphere reorganization (within the reactants) and the solvent reorganization is little if any solvent influence on the actual HAT step. Viewed from this perspective, our study is focused on the factors that affect the inner–sphere reorganization energies. Our kinetic discussion showed that the quite different kinetic reactivity of diamond core complexes relative to the open core ones can be ascribed to the different distortion energy of diiron reagent. The diamond core structure is supposed to suffer more energetic cost to rearrange the rhomb accompanying the redox process. We would, therefore, expect similar bonding changes in their self–exchange reactions and it would appear then that there may be larger intrinsic barriers for diamond core complexes than for the open core ones. If the bonding changes in our kinetic analysis can be considered analogous to, or partially reflect the reorganization energy in self–exchange

reactions, then the analogy between the present study and explorations of the Marcus cross-relation is evident. Therefore, this can be considered as one example of the success of Marcus theory in exploring HAT reactions.

5.4 Conclusion

We have performed a systematic DFT study on the DHA oxidation by complexes **1** – **4**. Our studies show that the DHA oxidation by complexes **1**, **3** and **4** follow the HAT mechanism while a hydride transfer pathway is established for **2**. The greatly enhanced reactivity from complex **1** to **4** can be understood with respect to the thermodynamic (BDE_{O-H}) and kinetic consideration (three energetic contributions to TS). First, switching from the diamond core to the open core structure greatly reduces the geometric changes upon redox process thereby lowering the energetic cost required for the transition states. Second, the high-spin state of Fe(IV)=O center enables complex **4** to follow a quintet σ–pathway that is favored not only by the exchange enhanced stability in thermochemistry but also by a favorable stereochemistry in the kinetic aspect. Our analysis reflects the importance of driving force and differences in reorganization energies in understanding hydrogen atom transfer reactivity. Given the high energetic cost resulted from the geometry reorganization of the diamond core, our study suggest that as the consequence of substrate binding and/or carboxylate shift the diamond structure **Q** may collapse to a more powerful oxidant, such as an “open core”, to proceed the following C–H bond activation. If the kinetic consideration in our discussion can partially reflect the intrinsic barrier mentioned in Marcus theory, then our study can be considered as one example of the success of Marcus theory in exploring HAT reactions.

6. Hydrogen Bonding Effects on the Reactivity of [X-Fe^{III}–O–Fe^{IV}=O] (X = OH, F) Complexes towards C–H Bond Cleavage

6.1 Introduction

The controlled oxidation unactivated C–H bonds such as those of methane is one of the great challenges in synthetic chemistry and typically requires catalysts by transition metals.[271] Iron is the most common metal center used in nature to oxidize C-H bonds by dioxygen activation mechanisms, in which high-valent oxoiron species are often postulated or demonstrated to act as the actual oxidizing species. Of these O_2-activating metalloenzymes, soluble methane monooxygenase (sMMO) deserves a particular attention,[34,86] because this enzyme oxidize methane, which has the strongest C–H bond of all hydrocarbons, to methanol.[239] In the catalytic circle, the intermediate called **Q** prior to methane oxidation has been trapped and characterized with various spectroscopic methods.[240-244] The experimental finding suggest that intermediate **Q** has a di(μ-oxo)diiron(IV) diamond core, in which two high-spin (S = 2) Fe(IV)=O units are antiferromagnetically coupled.[41] Related diiron(IV) intermediates have also been proposed as key oxidants in the catalytic circle of fatty acid desaturases and other diiron enzymes.[245-247]

The mechanism of methane hydroxylation by sMMO-**Q**, however, is not yet fully understood. For example, there is an ongoing debate issue about the isomerization of proposed structure **Q** during the oxidation process. This notion originates from the fact that **Q** has extremely high reactivity towards unactivated C–H bond activation but no self-oxidation to the protein was detected. Indeed, some DFT calculations have raised the possibility that [Fe^{III}–O–Fe^{V}=O] or [$Fe^{III}(\mu\text{-}O)_2Fe^{V}$] isomers of the [$Fe_2^{IV}(\mu\text{-}O)_2$] diamond core may be involved in methane oxidation. The reactivity patterns of several synthetic diiron complexes also suggest reconsideration of the proposed structure of **Q**. In the work of Caradonna and Rybak-Akimova on a diiron(II) catalyst for efficient hydroxylation of cyclohexane with ROOH as oxidant, the spectroscopic evidence showed that the relative stable [Fe^{III}–O–Fe^{III}] reagent isomerizes to a more reactive oxidant [$Fe^{II}Fe^{IV}$=O] that has a terminal Fe(IV)=O unit upon substrate approaching.[251-253] In a series work of Que and coworkers, they have characterized the first examples of complexes with [$Fe^{III}(\mu\text{-}O)_2Fe^{IV}$] (**1** in Scheme 1) and [$Fe_2^{IV}(\mu\text{-}O)_2$] core structures, proving synthetic precedents for the [$Fe_2^{IV}(\mu\text{-}O)_2$] core proposed for **Q**. However, these model complexes exhibit C–H bond oxidation reactivities that are far below those of a closely related mononuclear oxoiron(IV) complex and a more recently synthesized open core complex [HO–Fe^{IV}–O–Fe^{IV}=O] (**2** in

Scheme 6.1). These comparison suggests that an oxidant with a terminal Fe(IV)=O unit might be more effective for C–H bond cleavage than one having an oxo-bridged Fe–O–Fe center and indicate that further structural characterization of **Q** is necessary to understand better how this intermediate hydroxylates methane.

The high reactivity of the open core complexes are confirmed by Que's later work. The new synthesized valence-localized high-spin [HO–Fe^{III}–O–Fe^{IV}=O] complex (**1**-OH) cleaves strong C–H bonds a million-fold more rapidly than its [$Fe^{III}(\mu\text{-}O)_2Fe^{IV}$] analogue. More recently, they have also been able to obtain by treatment of **1** with fluoride the related open core complex **1**-F, which has a [F–Fe^{III}–O–Fe^{IV}=O] core that is closely related to that of **1**-OH. The reactivity study demonstrates that **1**-F is a more powerful oxidant than **1**-OH for C–H bond activation. Similar reactivity differences are also observed for **1**-OCD_3, with a [CH_3O–Fe^{III}–O–Fe^{IV}=O]. Que have suggested that the higher reactivity of **1**-F and **1**-OCD_3 is due to the lack of H-bond to the terminal oxoiron(IV) moiety. The presence of H-bond in **1**-OH and its absence in **1**-F and **1**-OCD_3 would be expected to result in the attenuation of the H-atom abstracting capability of **1**-OH. Borovik has also elegantly demonstrated the significance of intramolecular hydrogen bonds in stabilizing the first crystallographically characterized, synthetic oxoiron(III) complex.[5] Oxidizing the oxoiron(III) center to its iron(IV) counterpart significantly weakens H-bonds to the Fe^{IV}=O center,[6] but how this affects reactivity has not been determined. In the present chapter, we carry out detailed theoretical study on the reactivity of 1-**OH** and 1-**F** complexes shown in Scheme 6.1. Clarifying the factors that how H-bond affects the reactivity of 1-**OH** will provide a comprehensive theoretical framework in which the presence of the H-bond in modulating the C–H bond oxidation reactivity.

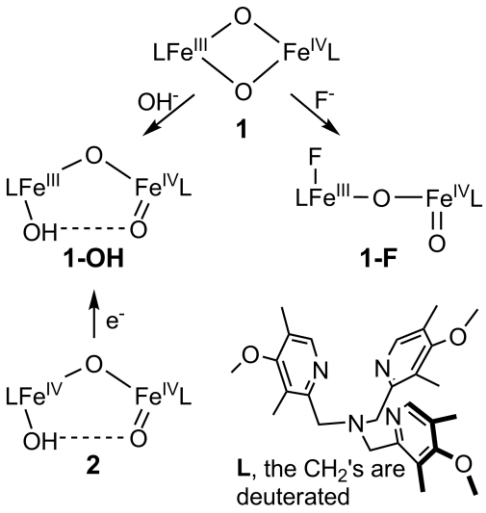

Scheme 6. 1 Structures of high-valent diiron complexes.

6.2 Computational details

A. See **2.7 Calculations set up**

6.3 Results and discussion

6.3.1 Geometric structure

DFT calculations were performed on **1**-OH_{cis} proposed above. Below the results obtained with the B3LYP functional are documented. Very similar results were obtained with the BP86 functional (Appendix). The computed key geometrical parameters (Figure 6.1) are in good agreement with the previous theoretical results (Figure 6.2).[262] The optimized structure of **1**-OH_{cis} features an open core structure of $[OH\text{-}Fe^{III}\text{-}O\text{-}Fe^{IV}=O]^{2+}$, similar to its one-electron oxidized diiron(IV) analog.[249] As shown in Figure 6.1, the calculated bond distances of O_1–H_1 (1.78 Å) and O_1–O_3 (2.73 Å) clearly indicate the presence of a weak hydrogen bond between the terminal oxo and hydroxyl groups, consistent with the van der Waals radii of the H- (1.20 Å) and O-atoms (1.52 Å).[272] Formation of the hydrogen bond is facilitated by the proximity of the Fe=O and Fe-OH units. Consequently, a relatively short Fe–Fe distance of 3.34 Å and a bent Fe_1-O_2-Fe_2 angle of 131.9° are obtained in **1**-OH_{cis}. For comparison, we also computationally investigated the *trans* conformer where the oxo and hydroxo groups are in a *trans* configuration. A nearly isoenergetic structure (**1**-OH_{trans}) resulted that is only about 2.4 kcal/mol higher in energy than **1**-OH_{cis}. Due to the loss of the cyclic H-bond, **1**-OH_{trans} shows a nearly linear $Fe_1O_2Fe_2$ arrangement of 174.5°, thereby leading to the longer Fe···Fe distance of 3.62 Å compared to **1**-OH_{cis}.

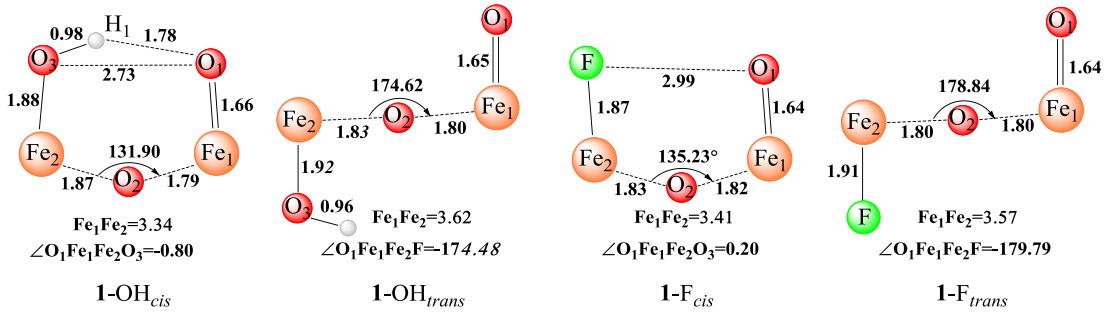

Figure 6. 1 Optimized Core structures of 1-OH and 1-F. Bond lengths are in angstroms, angles in degrees. Atom color scheme: H, white; O, red; Fe, orange; F, green.

Both *cis* and *trans* conformations were also calculated for the complex **1**-F. The computed *cis* conformer **1**-F_{cis}, that most closely resembles **1**-OH_{cis}, represents a local minimum. It is calculated to be 5.2 kcal/mol higher in energy than the *trans* conformer, **1**-F_{trans}. Thus, in agreement with experiment, the calculations confirm that, the *trans* configuration is

energetically slightly favorable. Our calculated key geometric parameters for **1**-F_{trans} match the experimental EXAFS data reasonably well (Figure 6.1) as well as previous DFT calculations (Figure 6.2).[262] The absence of the hydrogen bond in **1**-F_{cis} results in a loose "pocket" as evidenced by the rather long F–O_1 bond distance (2.99 Å) and the slightly larger Fe_1–O_2–Fe_2 angle (135.2°) compared to **1**-OH_{cis}. The calculated Fe-oxo bond length is 1.64 Å, which is comparable to **1**-OH_{cis} (1.66 Å) and **1**-OH_{trans} (1.65 Å). **1**-F_{trans} features a linear $Fe_1O_2Fe_2$ arrangement with a long $Fe_1\cdots Fe_2$ distance of 3.57 Å, similar to that calculated for **1**-OH_{trans}. **1**-OH_{cis} and **1**-F_{cis} contain bent $Fe_1O_2Fe_2$ cores and hence display relatively short $Fe_1\cdots Fe_2$ distances (Figure 6.1).

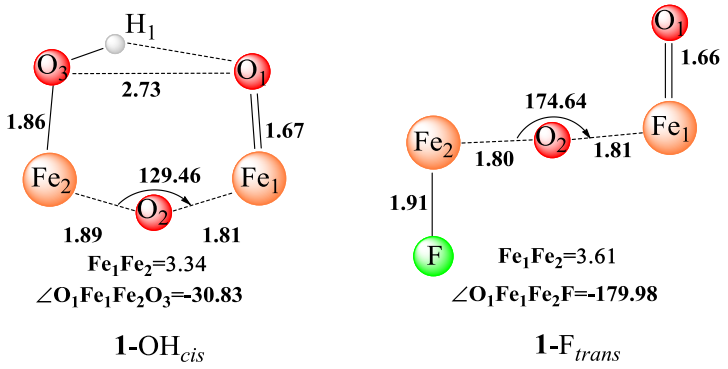

Figure 6. 2 The geometric data from previous theoretical results for 1-OH_{cis} and 1-F_{trans}.[262]

6.3.2 Reactivity

The incredible oxidizing ability of **1**-OH_{cis} towards C–H bond oxidation has previously been demonstrated by the million-fold activity enhancement compared to its one-electron oxidized form.[250] Under the same reaction conditions, the fluoride substituted complex **1**-F_{trans} displays even higher C-H bond cleavage reactivity towards DHA (the reaction rate turns out to be 10-fold faster than that of **1**-OH_{cis}). Herein, the reactivities of **1**-OH_{cis} and **1**-F_{trans} were theoretically modeled. In the following study, we only focus on the rate-determining H-atom abstraction step. Table 6.1 lists the selected structural parameters from the B3LYP optimized geometries, and Figure 6.3 shows the Gibbs free energy profiles of the DHA C-H bond activation by **1**-$OH_{cis,}$ **1**-OH_{trans} and **1**-F_{trans} systems.[273] The DFT results nicely reproduce the experimental findings. As shown in Figure 6.3, the energy barrier of H-atom abstraction by **1**-OH_{cis} is calculated to be 6.7 and 3.3 kcal/mol at the B3LYP and B3LYP + VDW levels of theory, respectively, a few kcal/mol higher than that calculated for the **1**-F_{trans} system (4.3 and 2.5 kcal/mol). This is in good agreement with the rate enhancement observed experimentally that corresponds to a decrease in the activation energy by ~1 kcal/mol.

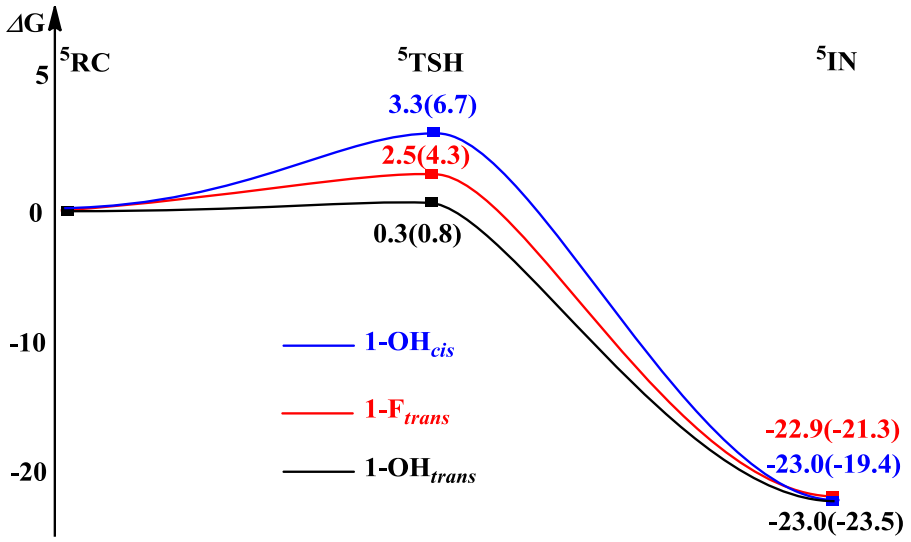

Figure 6. 3 Calculated Schematic Gibbs free energy (ΔG) surfaces for DHA C-H bond activation by 1-OH_{cis}, 1-F_{trans} and 1-OH_{trans}. In parentheses, energies without inclusion of VDW effects are given.

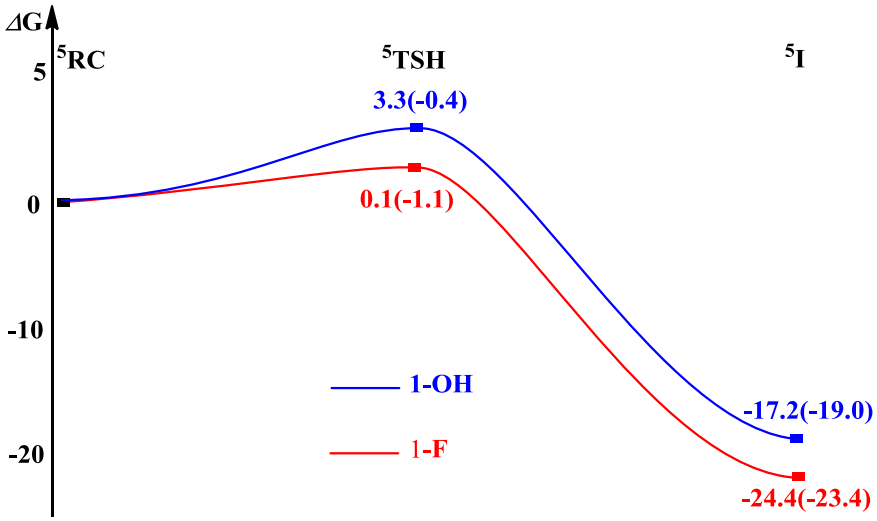

Figure 6. 4 BP86 Calculated Schematic Gibbs free energy (ΔG) surfaces for DHA C-H bond activation by 1-OH_{cis} and 1-F_{trans}. In parentheses energies with inclusion of VDW effects are given.

In fact, the process of C-H bond oxidation by the two complexes follows the same reaction mechanism. As expected, the reaction takes place at the Fe^{IV}=O unit and follows the typical σ-mechanism that has been well established for *S* = 2 mononuclear iron(IV)oxo complexes.[198,201,215,216,274] The electrophilic attack of the substrate on the high spin Fe^{IV}=O center involves the transfer of one spin-up electron from the substrate into the σ*(Fe-oxo) antibonding orbital (Scheme 6.2). During this process, the oxidation state of the diiron

core changes from a mixed valence state of Fe^{IV}-Fe^{III} in the reaction complexes (RC) to a Fe^{III}-Fe^{III} state in the intermediates (IN). As the two complexes are supported by the same ligand and, more importantly, share the similar open core structure $[X\text{-}Fe^{III}\text{-}O\text{-}Fe^{IV}{=}O]^{3+}$ the main question is why **1**-F_{tran} may have stronger oxidizing ability than **1**-OH_{cis}.

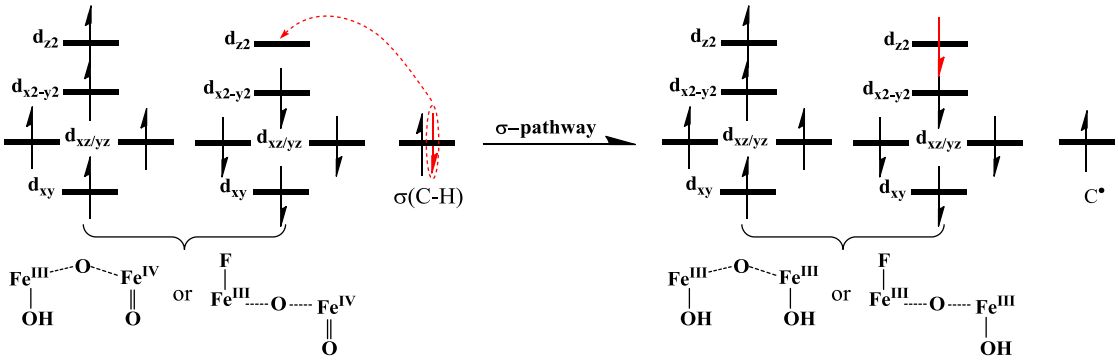

Scheme 6.2 Orbital occupancy-evolution diagrams for C–H bond activation by **1**-OH and **1**-F.

6.3.3 Discussion

There could be several factors accounting for the different reactivities upon going from system **1**-OH_{cis} to **1**-F_{trans}. The first factor might be the changes in the electronic properties of the Fe^{IV}-oxo reactive center that directly involved in the reaction. As shown in Table 6.1, the estimated Fe=O bond distance in **1**-OH_{cis} is marginally longer than that in **1**-F_{trans}. Moreover, the calculated Fe=O bond order of 1.7 for **1**-OH_{cis} is slightly lower than that for **1**-F_{trans} (1.8), which is consistent with the computed Fe=O stretching frequencies (834 cm^{-1} for **1**-OH_{cis} vs. 867 cm^{-1} for **1**-F_{trans}). Therefore, the hydrogen bond slightly weakens the Fe=O bond in **1**-OH_{cis}. This will tend to lower the barrier for H-atom abstraction rather than increasing it, because lengthening of the Fe=O bond is a key reaction coordinate.[7,114,193,216] However, nearly identical Fe_1-O_1, C-H_2 and O_1-H_2 bond distances were found in TSH(**1**-OH_{cis}) and TSH(**1**-F_{trans}) (Table 6.1), indicating that the hydrogen bond in **1**-OH_{cis} does not lead to significant changes in the electrophilicity of the Fe^{IV}-oxo motif.

The second reason for the increased reactivity of **1**-F_{trans} over **1**-OH_{cis} could be different steric hindrances encountered in the two systems. In fact, as shown in Figure 6.4, the reaction center (terminal oxo) in **1**-F_{trans} system is partially shielded by the pyridine group which has a *cis* orientation with respect to the terminal oxo group. Therefore, it is easier for the substrate to approach the reactive center in **1**-OH_{cis} system than in **1**-F_{trans}. Consequently, we would expect higher reactivity of **1**-OH_{cis} compared to that of **1**-F_{trans} from such an analysis. However, both experiment and theoretical calculations

demonstrated the opposite trend for the reactivity of the two complexes. Thus, the underlying reason for these intriguing reactivity differences must lie in other factors.

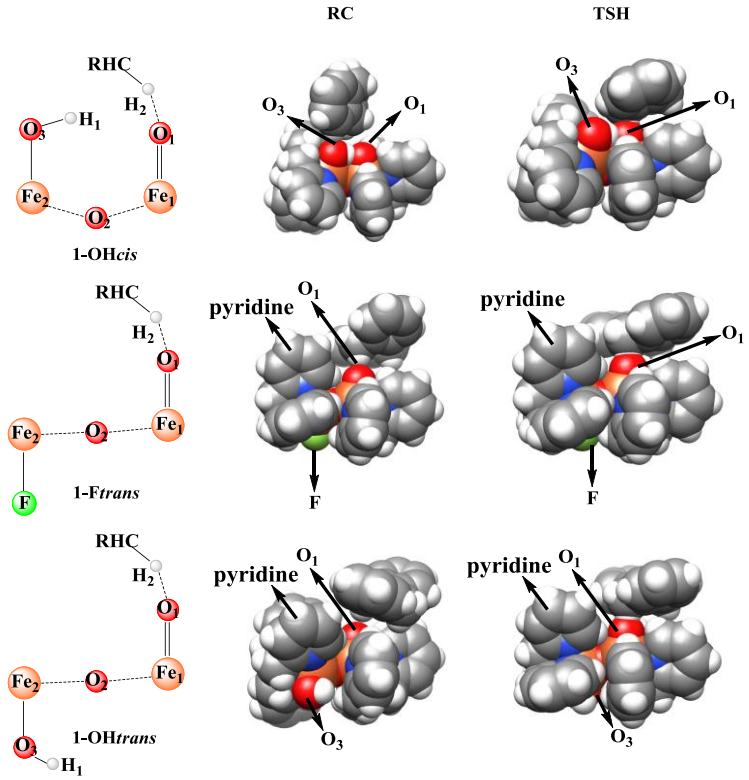

Figure 6. 5 Space-filling models of reaction complexes (RCs) and transition states (TSHs) for 1-F_{trans}, 1-OH_{cis} and 1-OH_{trans}. Atom color scheme: C, gray; H, white; N, blue; O, red; Fe, orange; F, green.

In the H-atom abstraction process by mononuclear iron-oxo complexes, the key reaction coordinates are lengthening of the target C-H bond of the substrate with a simultaneous increase of the Fe=O bond distance.[7,114,193,216] Indeed, for the reaction with **1**-F_{trans}, we have not observed any other coordinates to undergo significant changes towards approach of the transition state. Interestingly, a third coordinate undergoes significant changes during the reaction with **1**-OH_{cis}. This motion involves lengthening of the hydrogen bond between the hydroxide and terminal oxo groups. As shown in Table 6.1, comparison of the structures of RC(**1**-OH_{cis}) and TSH(**1**-OH_{cis}) clearly demonstrates weakening of the hydrogen bond during the reaction process, especially for the absence of the VDW correction. This is readily ascribed to the changes in the electronic structure of the Fe^{IV}=O unit along the reaction coordinate. As discussed elsewhere, as the Fe-oxo bond lengthens, the Fe^{IV}-oxo intermediate evolves to a species that is best characterized as Fe^{III}oxyl.[85] This should result in a geometric adjustment of the hydrogen bond length (O1–H1) because of the lower electron donating capability of the oxyl group relative to the

more negatively charged oxo ligand. As a consequence of the hydrogen bond lengthening, more energy may be required en route to the transition state for **1**-OH_{cis} due to the larger geometric distortion compared to **1**-F_{trans}. To test this hypothesis, we have theoretically investigated the same reaction with the *trans* conformer **1**-OH_{trans}. It turns out that **1**-OH_{trans} is more efficient in C-H bond activation than **1**-OH_{cis} and **1**-F_{trans} (Figure 6.5). This indicates that partially breaking the hydrogen bond indeed slows down the reaction for **1**-OH_{cis} and explains the higher energy barrier encountered by **1**-OH_{cis} than that for **1**-F_{trans}.

6.4 Conclusion

In summary, our calculations revealed that the hydrogen bond between the oxo and hydroxo group in 1-OH_{cis} does not significantly change the electrophilicity of the reactive Fe^{IV}=O unit. However, during the reaction of C-H bond oxidation, this hydrogen bond has to be partially broken. This leads to the slightly higher barrier for **1**-OH_{cis} relative to **1**-F_{trans}, which has similar open-core structure but no hydrogen bond.

Table 6. 1 Selected Geometry Parameters for the Key Points along the Reaction Pathways. Normal, with VDW effect. In parentheses, values without VDW effect are given.

	Fe_1-O_1	Fe_1-Fe_2	∠$Fe_1O_2Fe_2$(°)	∠$O_1Fe_1Fe_2O_3$(F)	O_1-O_3	O_1-H_1	O_1-H_2	C-H_2
RC(**1**-OH_{cis})	1.66(1.66)	3.34(3.37)	133.34(134.04)	2.59(0.02)	2.73(2.74)	1.79(1.80)	~	1.10(1.10)
TSH(**1**-OH_{cis})	1.73(1.75)	3.33(3.38)	131.90(134.31)	-5.55(-15.53)	2.77(2.84)	1.82(1.89)	1.40(1.40)	1.20(1.21)
IN(**1**-OH_{cis})	1.88(1.89)	3.33(3.39)	132.25(135.71)	1.42(0.96)	2.75(2.79)	1.80(1.84)	0.96(0.96)	2.41(2.59)
RC(**1**-F_{trans})	1.64(1.65)	3.59(3.61)	176.00(178.79)	-174.10 (-178.58)	~	~	2.45(2.42)	1.10(1.10)
TSH(**1**-F_{trans})	1.72(1.73)	3.59(3.63)	172.79(175.92)	173.44(172.99)	~	~	1.39(1.41)	1.20(1.20)
IN(**1**-F_{trans})	1.86(1.88)	3.60(3.62)	167.86(166.38)	175.29(170.65)	~	~	0.96(0.96)	2.51(3.12)
RC(**1**-OH_{trans})	1.65(1.65)	3.58(3.60)	171.04(166.68)	-151.00(-143.79)	~	~	2.29(2.50)	1.10(1.10)
TSH(**1**-OH_{trans})	1.72(1.73)	3.59(3.64)	176.02(178.25)	-172.54(172.92)	~	~	1.38(1.40)	1.21(1.22)
IN(**1**-OH_{trans})	1.88(1.87)	3.63(3.64)	174.06(174.13)	-178.27(178.94)	~	~	0.96(0.96)	2.58(3.04)

Table 6. 2 BP86 Calculated Geometry Parameters for the Key Points along the Reaction Pathways. Normal, with VDW effect. In parentheses, without VDW effect.

	Fe1-O1	Fe1-Fe2	∠$Fe_1O_2Fe_2$(°)	∠$O_1Fe_1Fe_2O_3$(F) (°)	O_1-O_3	O1-H1	O1-H2	C-H2
RC(**1**-OH_{cis})	1.68(1.69)	3.23(3.32)	126.94(131.71)	-31.41(-5.62)	2.67(2.60)	1.69(1.61)	~	1.11(1.11)
TSH(**1**-OH_{cis})	1.76(1.77)	3.24(3.33)	127.62(132.98)	-25.39(-19.00)	2.68(2.74)	1.71(1.76)	1.20(1.23)	1.34(1.35)
IN(**1**-OH_{cis})	1.89(1.91)	3.21(3.34)	127.34(134.09)	-36.21(-21.97)	2.85(2.88)	1.94(1.93)	0.98(0.98)	3.33(2.48)
RC(**1**-F_{trans})	1.67(1.67)	3.55(3.53)	173.68(146.45)	-177.18(132.97)	~	~	~	1.11(1.11)
TSH(**1**-F_{trans})	1.74(1.75)	3.54(3.60)	165.60(168.28)	177.79(165.55)	~	~	1.21(1.21)	1.33(1.35)
IN(**1**-F_{trans})	1.87(1.87)	3.55(3.57)	163.54(162.23)	173.25(168.34)	~	~	0.98(0.97)	2.30(5.50)

7. Conclusion

In the present Ph.D thesis, the C–H bond activation by different high-valent iron–oxo or –nitrido complexes are addressed.

1. In the C–H bond activation by four different mononuculear iron(IV)oxo complexes, we have first characterized all viable pathways in the same system, which allows us to compare their relative reactivities. The new established triplet σ-pathway is higher in energy such that it may not ever be involved in actual C-H bond hydroxylations. However, the reactivity of the quintet π-channel is comparable or even higher than the classical triplet one ($^3\boldsymbol{\pi}$), although it is slightly higher in energy than the established quintet one ($^5\boldsymbol{\sigma}$). The existence of at least three energetically feasible pathways may offer, however, a new element of specificity control in C-H bond activation reactions by oxo-iron(IV) species. The choice of σ- or π-pathways could be controlled at least in part by steric hinderance in model systems or by the restrictions of the protein pocket in metalloenzymes.

2. Six "hypothetic" iron complexes have been studied to investigate the determinant factor for controlling the oxidative C-H bond cleavage by iron–oxo and –nitrido complexes. DFT calculations demonstrated that although quite opposite reactivity is obtained for these two series, a good correlation between the driving force and the energy barrier is established, in close agreement with the Polanyi principle. More importantly, a close inspection of the thermochemical $H^{\bullet}$ affinity, which determined by its electron and proton affinity component, showed that the iron–oxo and –nitrido complexes have quite different properties. The oxo complexes have significant stronger oxidation power than their nitrido counterpart, while the nitrido complexes have relatively larger basicity inverse. Additionally, the counterintuitive reactivity of these two series also can be well understood by the separate EA and PA analysis. The gradually increased reactivity in oxo series is ascribed to the substantial increase in oxidation power, while the offset of the EA and PA functions in nitrido series leads to BDE_{NH} to be a constant.

3. We have performed a systematic DFT study on the DHA oxidation by four diiron complexes, two with diamond core structure, (Fe^{III}–$(O)_2$–Fe^{IV}, **1** and Fe^{IV}–$(O)_2$–Fe^{IV} **2**) and two with open core structure (OH–Fe^{IV}–O–Fe^{IV}=O, **3** and OH–Fe^{III}–O–Fe^{IV}=O, **4**). Our studies show that the DHA oxidation by complexes **1**, **3** and **4** follow the HAT mechanism while a hydride transfer pathway is established for **2**. The greatly enhanced reactivity from complex **1** to **4** can be understood with respect to the thermodynamic (BDE_{O-H}) and kinetic consideration (three energetic contributions to TS). First, switching from the diamond core to the open core structure greatly reduces the geometric changes upon redox process thereby lowering the energetic cost required for the transition states. Second, the high-spin state of Fe(IV)=O center enables complex **4** to follow a quintet σ–pathway that is

favored not only by the exchange enhanced stability in thermochemistry but also by a favorable stereochemistry in the kinetic aspect. Our analysis reflects the importance of driving force and differences in reorganization energies in understanding hydrogen atom transfer reactivity. Given the high energetic cost resulted from the geometry reorganization of the diamond core, our study suggest that as the consequence of substrate binding and/or carboxylate shift the diamond structure **Q** may collapse to a more powerful oxidant, such as an "open core", to proceed the following C–H bond activation. If the kinetic consideration in our discussion can partially reflect the intrinsic barrier mentioned in Marcus theory, then our study can be considered as one example of the success of Marcus theory in exploring HAT reactions.

4. Of the H-bond effect in modulating C–H bond activation, there could be several factors accounting for the different reactivities upon going from system **1**-OH_{cis} to **1**-F_{trans}. Our results revealed that the hydrogen bond between the oxo and hydroxo group in 1-OH_{cis} does not significantly change the electrophilicity of the reactive Fe^{IV}=O unit. However, during the reaction of C-H bond oxidation, this hydrogen bond has to be partially broken. This leads to the slightly higher barrier for **1**-OH_{cis} relative to **1**-F_{trans}, which has similar open-core structure but no hydrogen bond.

Bibliography

1. A. S. Borovik, M. K. Zart and P. J. Zinn, *Activation of Small Molecules: Organometallic and Bioinorganic Perspectives*, Wiley-VCH, Weinheim, 2006.
2. E. I. Solomon, T. C. Brunold, M. I. Davis, J. N. Kemsley, S. K. Lee, N. Lehnert, F. Neese, A. J. Skulan, Y. S. Yang and J. Zhou, *Chem. Rev.*, 2000, **100**, 235-349.
3. K. L. Stone and A. S. Borovik, *Curr. Opin. Chem. Biol.*, 2009, **13**, 114-118.
4. D. L. Harris, *Curr. Opin. Chem. Biol.*, 2001, **5**, 724-735.
5. E. I. Solomon, S. D. Wong, L. V. Liu, A. Decker and M. S. Chow, *Curr. Opin. Chem. Biol.*, 2009, **13**, 99-113.
6. S. Ye and F. Neese, *Curr. Opin. Chem. Biol.*, 2009, **13**, 89-98.
7. M. M. Abu-Omar, A. Loaiza and N. Hontzeas, *Chem. Rev.*, 2005, **105**, 2227-2252.
8. M. Costas, M. P. Mehn, M. P. Jensen and L. Que, Jr., *Chem. Rev.*, 2004, **104**, 939-986.
9. I. G. Denisov, T. M. Makris, S. G. Sligar and I. Schlichting, *Chem. Rev.*, 2005, **105**, 2253-2277.
10. S. Shaik, D. Kumar, S. P. de Visser, A. Altun and W. Thiel, *Chem. Rev.*, 2005, **105**, 2279-2328.
11. B. Meunier, S. P. de Visser and S. Shaik, *Chem. Rev.*, 2004, **104**, 3947-3980.
12. S. Shaik, S. Cohen, Y. Wang, H. Chen, D. Kumar and W. Thiel, *Chem. Rev.*, 2010, **110**, 949-1017.
13. M. Sono, M. P. Roach, E. D. Coulter and J. H. Dawson, *Chem. Rev.*, 1996, **96**, 2841-2887.
14. J. T. Groves, *Proc. Natl. Acad. Sci. USA.*, 2003, **100**, 3569-3574.
15. P. R. Ortiz de Montellano (Ed), *Cytochrome P450: Structure, Mechanism and Biochemistry*, Kluwer Academic/Plenum, New York 2004.
16. P. R. O. de Montellano, *Chem. Rev.*, 2010, **110**, 932-948.
17. S. P. de Visser and D. Kumar, *Iron-Containing Enzymes: Versatile Catalysts of Hydroxylation Reaction in Nature*, RSC Publishing, Cambridge, U.K., 2011.
18. R. Davydov, T. M. Makris, V. Kofman, D. E. Werst, S. G. Sligar and B. M. Hoffman, *J. Am. Chem. Soc.*, 2001, **123**, 1403-1415.
19. T. S. Dowers, D. A. Rock, D. A. Rock and J. P. Jones, *J. Am. Chem. Soc.*, 2004, **126**, 8868-8869.
20. J. Rittle and M. T. Green, *Science.*, 2010, **330**, 933-937.
21. C. Krebs, D. G. Fujimori, C. T. Walsh and J. M. Bollinger, Jr., *Acc. Chem. Res.*, 2007, **40**, 484-492.
22. W. Nam, *Acc. Chem. Res.*, 2007, **40**, 465-465.
23. L. J. Higgins, F. Yan, P. H. Liu, H. W. Liu and C. L. Drennan, *Nature*, 2005, **437**, 838-844.
24. O. W. Choroba, D. H. Williams and J. B. Spencer, *J. Am. Chem. Soc.*, 2000, **122**, 5389-5390.
25. F. Fukumori and R. P. Hausinger, *J. Biol. Chem*, 1993, **268**, 24311-24317.
26. X. P. Shan and L. Que, Jr., *J. Inorg. Biochem.*, 2006, **100**, 421-433.
27. S. V. Kryatov, E. V. Rybak-Akimova and S. Schindler, *Chem. Rev.*, 2005, **105**, 2175-2226.
28. M. D. Wolfe, J. V. Parales, D. T. Gibson and J. D. Lipscomb, *J. Biol. Chem*, 2001, **276**, 1945-1953.
29. M. D. Wolfe and J. D. Lipscomb, *J. Biol. Chem*, 2003, **278**, 829-835.

30. S. Chakrabarty, R. N. Austin, D. Y. Deng, J. T. Groves and J. D. Lipscomb, *J. Am. Chem. Soc.*, 2007, **129**, 3514-3515.
31. E. P. Talsi, O. Y. Lyakin, K. P. Bryliakov and G. J. P. Britovsek, *J. Am. Chem. Soc.*, 2009, **131**, 10798-+.
32. J. Yoon, S. A. Wilson, Y. K. Jang, M. S. Seo, K. Nehru, B. Hedman, K. O. Hodgson, E. Bill, E. I. Solomon and W. Nam, *Angew. Chem. Int. Ed.*, 2009, **48**, 1257-1260.
33. I. Prat, J. S. Mathieson, M. Güell, X. Ribas, J. M. Luis, L. Cronin and M. Costas, *Nature Chem.*, 2011, **3**, 788-793.
34. C. E. Tinberg and S. J. Lippard, *Acc. Chem. Res.*, 2011, **44**, 280-288.
35. S. Friedle, E. Reisner and S. J. Lippard, *Chem. Soc. Rev.*, 2010, **39**, 2768-2779.
36. J. Colby and H. Dalton, *Biophys. J.*, 1978, **171**, 461-468.
37. B. G. Fox, W. A. Froland, J. E. Dege and J. D. Lipscomb, *J. Biol. Chem*, 1989, **264**, 10023-10033.
38. A. C. Rosenzweig, C. A. Frederick, S. J. Lippard and P. Nordlund, *Nature*, 1993, **366**, 537-543.
39. A. C. Rosenzweig, P. Nordlund, P. M. Takahara, C. A. Frederick and S. J. Lippard, *Chem Biol*, 1995, **2**, 409-418.
40. G. Q. Xue, D. Wang, R. De Hont, A. T. Fiedler, X. P. Shan, E. Munckt and L. Que, Jr., *Proc. Natl. Acad. Sci. USA.*, 2007, **104**, 20713-20718.
41. L. Shu, *Science.*, 1997, **275**, 515-518.
42. T. M. Makris, K. von Koenig, I. Schlichting and S. G. Sligar, *J. Inorg. Biochem.*, 2006, **100**, 507-518.
43. I. Schlichting, J. Berendzen, K. Chu, A. M. Stock, S. A. Maves, D. E. Benson, B. M. Sweet, D. Ringe, G. A. Petsko and S. G. Sligar, *Science.*, 2000, **287**, 1615-1622.
44. Y. M. Goh and W. W. Nam, *Inorg. Chem.*, 1999, **38**, 914-920.
45. Y. Kang, H. Chen, Y. J. Jeong, W. Lai, E. H. Bae, S. Shaik and W. Nam, *Chem. Eur. J.*, 2009, **15**, 10039-10046.
46. B. Meunier, A. Robert, G. Pratviel and J. Bernadou, *The Porphyrin Handbook*, 2000.
47. J. T. Groves, R. C. Haushalter, M. Nakamura, T. E. Nemo and B. J. Evans, *J. Am. Chem. Soc.*, 1981, **103**, 2884-2886.
48. H. Fujii, *Coord. Chem. Rev*, 2002, **226**, 51-60.
49. J. T. Groves, *J. Inorg. Biochem.*, 2006, **100**, 434-447.
50. C. Jung, *Bba-Proteins Proteom*, 2011, **1814**, 46-57.
51. W. Nam, *Acc. Chem. Res.*, 2007, **40**, 522-531.
52. Z. Gross and S. Nimri, *Inorg. Chem.*, 1994, **33**, 1731-1732.
53. C. A. Grapperhaus, B. Mienert, E. Bill, T. Weyhermuller and K. Wieghardt, *Inorg. Chem.*, 2000, **39**, 5306-5317.
54. J. U. Rohde, J. H. In, M. H. Lim, W. W. Brennessel, M. R. Bukowski, A. Stubna, E. Münck, W. Nam and L. Que. Jr, *Science.*, 2003, **299**, 1037-1039.
55. C. V. Sastri, M. J. Park, T. Ohta, T. A. Jackson, A. Stubna, M. S. Seo, J. Lee, J. Kim, T. Kitagawa, E. Munck, L. Que, Jr. and W. Nam, *J. Am. Chem. Soc.*, 2005, **127**, 12494-12495.
56. A. Decker, J. U. Rohde, L. Que, Jr. and E. I. Solomon, *J. Am. Chem. Soc.*, 2004, **126**, 5378-5379.
57. L. Que, Jr., *Acc. Chem. Res.*, 2007, **40**, 493-500.
58. J. Kaizer, E. J. Klinker, N. Y. Oh, J. U. Rohde, W. J. Song, A. Stubna, J. Kim, E. Münck, W. Nam and L. Que. Jr, *J. Am. Chem. Soc.*, 2004, **126**, 472-473.

59. M. S. Hill, P. B. Hitchcock and R. Pongtavornpinyo, *Angew. Chem. Int. Ed.*, 2005, **44**, 4231-4235.
60. S. O. Kim, C. V. Sastri, M. S. Seo, J. Kim and W. Nam, *J. Am. Chem. Soc.*, 2005, **127**, 4178-4179.
61. M. R. Bukowski, K. D. Koehntop, A. Stubna, E. L. Bominaar, J. A. Halfen, E. Munck, W. Nam and L. Que, Jr., *Science.*, 2005, **310**, 1000-1002.
62. M. J. Park, J. Lee, Y. Suh, J. Kim and W. Nam, *J. Am. Chem. Soc.*, 2006, **128**, 2630-2634.
63. C. V. Sastri, K. Oh, Y. J. Lee, M. S. Seo, W. Shin and W. Nam, *Angew. Chem. Int. Ed.*, 2006, **45**, 3992-3995.
64. K. Nehru, M. S. Seo, J. Kim and W. Nam, *Inorg. Chem.*, 2007, **46**, 293-298.
65. C. V. Sastri, J. Lee, K. Oh, Y. J. Lee, J. Lee, T. A. Jackson, K. Ray, H. Hirao, W. Shin, J. A. Halfen, J. Kim, L. Que, Jr., S. Shaik and W. Nam, *Proc. Natl. Acad. Sci. USA.*, 2007, **104**, 19181-19186.
66. M. Martinho, F. Banse, J. F. Bartoli, T. A. Mattioli, P. Battioni, O. Horner, S. Bourcier and J. J. Girerd, *Inorg. Chem.*, 2005, **44**, 9592-9596.
67. A. E. Anastasi, P. Comba, J. McGrady, A. Lienke and H. Rohwer, *Inorg. Chem.*, 2007, **46**, 6420-6426.
68. J. Bautz, P. Comba, C. L. de Laorden, M. Menzel and G. Rajaraman, *Angew. Chem. Int. Ed.*, 2007, **46**, 8067-8070.
69. M. H. Lim, J. U. Rohde, A. Stubna, M. R. Bukowski, M. Costas, R. Y. N. Ho, E. Munck, W. Nam and L. Que, Jr., *Proc. Natl. Acad. Sci. USA.*, 2003, **100**, 3665-3670.
70. C. V. Sastri, M. S. Seo, M. J. Park, K. M. Kim and W. Nam, *Chem Commun*, 2005, 1405-1407.
71. M. R. Bukowski, P. Comba, A. Lienke, C. Limberg, C. L. de Laorden, R. Mas-Balleste, M. Merz and L. Que, Jr., *Angew. Chem. Int. Ed.*, 2006, **45**, 3446-3449.
72. O. Pestovsky, S. Stoian, E. L. Bominaar, X. Shan, E. Münck, L. Que, Jr. and A. Bakac, *Angew. Chem. Int. Ed.*, 2006, **45**, 340-340.
73. J. England, M. Martinho, E. R. Farquhar, J. R. Frisch, E. L. Bominaar, E. Münck and L. Que, Jr., *Angew. Chem. Int. Ed.*, 2009, **48**, 3622-3626.
74. J. England, Y. S. Guo, E. R. Farquhar, V. G. Young, E. Münck and L. Que, Jr., *J. Am. Chem. Soc.*, 2010, **132**, 8635-8644.
75. M. P. Hendrich, D. C. Lacy, R. Gupta, K. L. Stone, J. Greaves, J. W. Ziller and A. S. Borovik, *J. Am. Chem. Soc.*, 2010, **132**, 12188-12190.
76. J. P. Bigi, W. H. Harman, B. Lassalle-Kaiser, D. M. Robles, T. A. Stich, J. Yano, R. D. Britt and C. J. Chang, *J. Am. Chem. Soc.*, 2012, **134**, 1536-1542.
77. F. T. de Oliveira, A. Chanda, D. Banerjee, X. P. Shan, S. Mondal, L. Que, E. L. Bominaar, E. Munck and T. J. Collins, *Science.*, 2007, **315**, 835-838.
78. Y. H. Dong, H. Fujii, M. P. Hendrich, R. A. Leising, G. F. Pan, C. R. Randall, E. C. Wilkinson, Y. Zang, L. Que, B. G. Fox, K. Kauffmann and E. Munck, *J. Am. Chem. Soc.*, 1995, **117**, 2778-2792.
79. J. T. Groves, G. A. Mcclusky, R. E. White and M. J. Coon, *Biochem. Biophys. Res. Commun.*, 1978, **81**, 154-160.
80. S. Shaik, S. Cohen, S. P. de Visser, P. K. Sharma, D. Kumar, S. Kozuch, F. Ogliaro and D. Danovich, *Eur. J. Inorg. Chem.*, 2004, 207-226.
81. S. P. de Visser, *J. Am. Chem. Soc.*, 2006, **128**, 9813-9824.
82. D. Janardanan, Y. Wang, P. Schyman, L. Que, Jr. and S. Shaik, *Angew. Chem. Int. Ed.*, 2010, **49**, 3342-3345.

83. C. Michel and E. J. Baerends, *Inorg. Chem.*, 2009, **48**, 3628-3638.
84. S. Shaik, H. Chen and D. Janardanan, *Nature Chem.*, 2011, **3**, 19-27.
85. S. Ye and F. Neese, *Proc. Natl. Acad. Sci. USA.*, 2011, **108**, 1228-1233.
86. M. H. Baik, M. Newcomb, R. A. Friesner and S. J. Lippard, *Chem. Rev.*, 2003, **103**, 2385-2419.
87. D. Balcells, E. Clot and O. Eisenstein, *Chem. Rev.*, 2010, **110**, 749-823.
88. K. Yoshizawa, *Acc. Chem. Res.*, 2006, **39**, 375-382.
89. K. Yoshizawa, *Coord. Chem. Rev*, 2002, **226**, 251-259.
90. K. Yoshizawa, *J. Biol. Inorg. Chem.*, 1998, **3**, 318-324.
91. M. Torrent, D. G. Musaev, H. Basch and K. Morocuma, *J. Comput. Chem.*, 2002, **23**, 59-76.
92. P. E. M. Siegbahn and M. R. A. Blomberg, *Chem. Rev.*, 2000, **100**, 421-437.
93. P. E. M. Siegbahn and T. Borowski, *Acc. Chem. Res.*, 2006, **39**, 729-738.
94. M. R. A. Blomberg and P. E. M. Siegbahn, *J. Phys. Chem. B*, 2001, **105**, 9375-9386.
95. R. A. Friesner and B. D. Dunietz, *Acc. Chem. Res.*, 2001, **34**, 351-358.
96. V. Guallar, B. F. Gherman, S. J. Lippard and R. A. Friesner, *Curr. Opin. Chem. Biol.*, 2002, **6**, 236-242.
97. R. A. Friesner, M. H. Baik, B. F. Gherman, V. Guallar, M. Wirstam, R. B. Murphy and S. J. Lippard, *Coord. Chem. Rev*, 2003, **238**, 267-290.
98. K. Yoshizawa, T. Ohta, T. Yamabe and R. Hoffmann, *J. Am. Chem. Soc.*, 1997, **119**, 12311-12321.
99. D. Schroder and H. Schwarz, *Angew Chem Int Edit*, 1995, **34**, 1973-1995.
100. F. Bonati and Minghett.G, *Journal of Organometallic Chemistry*, 1970, **22**, 5-&.
101. D. Schroder and H. Schwarz, *Proc. Natl. Acad. Sci. USA.*, 2008, **105**, 18114-18119.
102. M. Newcomb and P. H. Toy, *Acc. Chem. Res.*, 2000, **33**, 449-455.
103. Y. Nishida, T. Wiemann, V. Sinnwell and J. Thiem, *J. Am. Chem. Soc.*, 1993, **115**, 2536-2537.
104. Y. Nishida, T. Wiemann and J. Thiem, *Tetrahedron Lett*, 1992, **33**, 8043-8046.
105. M. Newcomb, R. Shen, S. Y. Choi, P. H. Toy, P. F. Hollenberg, A. D. N. Vaz and M. J. Coon, *J. Am. Chem. Soc.*, 2000, **122**, 2677-2686.
106. M. Newcomb, F. H. Letadicbiadatti, D. L. Chestney, E. S. Roberts and P. F. Hollenberg, *J. Am. Chem. Soc.*, 1995, **117**, 12085-12091.
107. M. Newcomb, M. H. Letadic, D. A. Putt and P. F. Hollenberg, *J. Am. Chem. Soc.*, 1995, **117**, 3312-3313.
108. M. Newcomb, R. N. Shen, Y. Lu, M. J. Coon, P. F. Hollenberg, D. A. Kopp and S. J. Lippard, *J. Am. Chem. Soc.*, 2002, **124**, 6879-6886.
109. S. P. de Visser, F. Ogliaro, N. Harris and S. Shaik, *J. Am. Chem. Soc.*, 2001, **123**, 3037-3047.
110. D. Schroder, S. Shaik and H. Schwarz, *Acc. Chem. Res.*, 2000, **33**, 139-145.
111. S. Shaik, D. Danovich, D. Schröder and H. Schwarz, *Helv Chim Acta*, 1995, **78**, 1393-1407.
112. S. Shaik, M. Filatov, D. Schroder and H. Schwarz, *Chem. Eur. J.*, 1998, **4**, 193-199.
113. F. Ogliaro, N. Harris, S. Cohen, M. Filatov, S. P. de Visser and S. Shaik, *J. Am. Chem. Soc.*, 2000, **122**, 8977-8989.
114. H. Hirao, D. Kumar, L. Que, Jr. and S. Shaik, *J. Am. Chem. Soc.*, 2006, **128**, 8590-8606.
115. M. Filatov and S. Shaik, *J. Phys. Chem. A*, 1998, **102**, 3835-3846.

116. D. Kumar, S. P. de Visser, P. K. Sharma, S. Cohen and S. Shaik, *J. Am. Chem. Soc.*, 2004, **126**, 1907-1920.
117. D. Kumar, S. P. de Visser and S. Shaik, *Chem. Eur. J.*, 2005, **11**, 2825-2835.
118. M. T. Green, *J. Am. Chem. Soc.*, 2001, **123**, 9218-9219.
119. M. T. Green, *Curr. Opin. Chem. Biol.*, 2009, **13**, 84-88.
120. D. Kumar, G. N. Sastry and S. P. de Visser, *Chemistry (Weinheim an der Bergstrasse, Germany)*, 2011, **17**, 6196-6205.
121. Y. K. Choe and S. Nagase, *J. Comput. Chem.*, 2005, **26**, 1600-1611.
122. M. T. Green, J. H. Dawson and H. B. Gray, *Science (New York, N.Y.)*, 2004, **304**, 1653-1656.
123. K. Czarnecki, S. Nimri, Z. Gross, L. M. Proniewicz and J. R. Kincaid, *J. Am. Chem. Soc.*, 1996, **118**, 2929-2935.
124. Z. Gross, *J. Biol. Inorg. Chem.*, 1996, **1**, 368-371.
125. H. Hirao, L. Que, Jr., W. Nam and S. Shaik, *Chem. Eur. J.*, 2008, **14**, 1740-1756.
126. T. A. Jackson, J. U. Rohde, M. S. Seo, C. V. Sastri, R. DeHont, A. Stubna, T. Ohta, T. Kitagawa, E. Munck, W. Nam and L. Que, Jr., *J. Am. Chem. Soc.*, 2008, **130**, 12394-12407.
127. K. A. Gardner and J. M. Mayer, *Science.*, 1995, **269**, 1849-1851.
128. J. M. Mayer, *Annu. Rev. Phys. Chem.*, 2004, **55**, 363-390.
129. M. G. Evans and M. Polanyi, *T Faraday Soc*, 1935, **31**, 0875-0893.
130. M. G. Evans and M. Polanyi, *T Faraday Soc*, 1936, **32**, 1333-1359.
131. M. G. Evans and M. Polanyi, *T Faraday Soc*, 1937, **33**, 0448-0452.
132. M. G. Evans and M. Polanyi, *T Faraday Soc*, 1938, **34**, 0011-0023.
133. F. G. Bordwell, J. P. Cheng, G. Z. Ji, A. V. Satish and X. M. Zhang, *J. Am. Chem. Soc.*, 1991, **113**, 9790-9795.
134. J. M. Mayer, *Acc. Chem. Res.*, 1998, **31**, 441-450.
135. A. S. Borovik, *Chem. Soc. Rev.*, 2011, **40**, 1870-1874.
136. K. M. Lancaster, M. Roemelt, P. Ettenhuber, Y. L. Hu, M. W. Ribbe, F. Neese, U. Bergmann and S. DeBeer, *Science.*, 2011, **334**, 974-977.
137. O. Einsle, F. A. Tezcan, S. L. A. Andrade, B. Schmid, M. Yoshida, J. B. Howard and D. C. Rees, *Science.*, 2002, **297**, 1696-1700.
138. J. C. Peters and M. P. Mehn, *In Activation of Small Molecules*, Wiley-VCH, 2006.
139. H. P. Hersleth, U. Ryde, P. Rydberg, C. H. Gorbitz and K. K. Andersson, *J. Inorg. Biochem.*, 2006, **100**, 460-476.
140. T. A. Betley and J. C. Peters, *J. Am. Chem. Soc.*, 2004, **126**, 6252-6254.
141. J. U. Rohde, T. A. Betley, T. A. Jackson, C. T. Saouma, J. C. Peters and L. Que, Jr., *Inorg. Chem.*, 2007, **46**, 5720-5726.
142. C. Vogel, F. W. Heinemann, J. Sutter, C. Anthon and K. Meyer, *Angew. Chem. Int. Ed.*, 2008, **47**, 2681-2684.
143. J. J. Scepaniak, M. D. Fulton, R. P. Bontchev, E. N. Duesler, M. L. Kirk and J. M. Smith, *J. Am. Chem. Soc.*, 2008, **130**, 10515-10517.
144. K. Meyer, J. J. Scepaniak, C. S. Vogel, M. M. Khusniyarov, F. W. Heinemann and J. M. Smith, *Science.*, 2011, **331**, 1049-1052.
145. K. Meyer, E. Bill, B. Mienert, T. Weyhermuller and K. Wieghardt, *J. Am. Chem. Soc.*, 1999, **121**, 4859-4876.

146. T. Petrenko, S. D. George, N. Aliaga-Alcalde, E. Bill, B. Mienert, Y. Xiao, Y. Guo, W. Sturhahn, S. P. Cramer, K. Wieghardt and F. Neese, *J. Am. Chem. Soc.*, 2007, **129**, 11053-11060.
147. W. D. Wagner and K. Nakamoto, *J. Am. Chem. Soc.*, 1988, **110**, 4044-4045.
148. M. Aliaga-Alcalde, S. D. George, B. Mienert, E. Bill, K. Wieghardt and F. Neese, *Angew. Chem. Int. Ed.*, 2005, **44**, 2908-2912.
149. J. F. Berry, E. Bill, E. Bothe, S. D. George, B. Mienert, F. Neese and K. Wieghardt, *Science.*, 2006, **312**, 1937-1941.
150. M. P. Hendrich, W. Gunderson, R. K. Behan, M. T. Green, M. P. Mehn, T. A. Betley, C. C. Lu and J. C. Peters, *Proc. Natl. Acad. Sci. USA.*, 2006, **103**, 17107-17112.
151. K. Nakamoto, *Coord. Chem. Rev*, 2002, **226**, 153-165.
152. P. Hohenberg and W. Kohn, *Phys. Rev. B*, 1964, **136**, B864-&.
153. W. Kohn and L. J. Sham, *Phys Rev*, 1965, **140**, 1133-&.
154. K. Raghavachari, *Theor. Chem. Acc.*, 2000, **103**, 361-363.
155. W. Kohn and L. J. Sham, *Phys Rev*, 1965, **137**, 1697-&.
156. D. M. Ceperley and B. J. Alder, *Phys Rev Lett*, 1980, **45**, 566-569.
157. S. H. Vosko, L. Wilk and M. Nusair, *Can J Phys*, 1980, **58**, 1200-1211.
158. J. P. Perdew, *Phys. Rev. B*, 1986, **33**, 8822-8824.
159. C. T. Lee, W. T. Yang and R. G. Parr, *Phys. Rev. B*, 1988, **37**, 785-789.
160. N. Oliphant and R. J. Bartlett, *J. Chem. Phys*, 1994, **100**, 6550-6561.
161. A. D. Becke, *J. Chem. Phys*, 1993, **98**, 1372-1377.
162. A. D. Becke, *Phys. Rev. A*, 1988, **38**, 3098-3100.
163. A. D. Becke, *J. Chem. Phys*, 1993, **98**, 5648-5652.
164. J. P. Perdew and Y. Wang, *Phys. Rev. B*, 1992, **45**, 13244-13249.
165. S. Grimme, *J. Chem. Phys*, 2006, **124**.
166. T. Schwabe and S. Grimme, *Phys. Chem. Chem. Phys.*, 2006, **8**, 4398-4401.
167. F. Neese, T. Schwabe and S. Grimme, *J. Chem. Phys*, 2007, **126**.
168. T. Benighaus, R. A. DiStasio, R. C. Lochan, J. D. Chai and M. Head-Gordon, *J. Phys. Chem. A*, 2008, **112**, 2702-2712.
169. T. Schwabe and S. Grimme, *Phys. Chem. Chem. Phys.*, 2007, **9**, 3397-3406.
170. K. Sharkas, J. Toulouse and A. Savin, *J. Chem. Phys*, 2011, **134**.
171. K. Denbigh, *The Principles of Chemical Equilibrium*, Cambridge University Press, Cambridge, 1991.
172. F. Neese, in *An Ab Initio, Density Functional and Semiempirical Program Package*, Bonn University, Germany, Version 2.8 edn., 2010.
173. A. Schafer, C. Huber and R. Ahlrichs, *J. Chem. Phys*, 1994, **100**, 5829-5835.
174. A. Schafer, H. Horn and R. Ahlrichs, *J. Chem. Phys*, 1992, **97**, 2571-2577.
175. R. A. Kendall and H. A. Fruchtl, *Theor. Chem. Acc.*, 1997, **97**, 158-163.
176. K. Eichkorn, O. Treutler, H. Ohm, M. Haser and R. Ahlrichs, *Chem. Phys. Lett.*, 1995, **240**, 283-289.
177. K. Eichkorn, F. Weigend, O. Treutler and R. Ahlrichs, *Theor. Chem. Acc.*, 1997, **97**, 119-124.
178. F. Neese, F. Wennmohs, A. Hansen and U. Becker, *Chem. Phys*, 2009, **356**, 98-109.
179. F. Weigend, M. Haser, H. Patzelt and R. Ahlrichs, *Chem. Phys. Lett.*, 1998, **294**, 143-152.
180. S. Grimme, J. Antony, S. Ehrlich and H. Krieg, *J. Chem. Phys*, 2010, **132**.
181. S. Grimme, *J. Comput. Chem.*, 2004, **25**, 1463-1473.

182. S. Grimme, *J. Comput. Chem.*, 2006, **27**, 1787-1799.
183. P. Comba, M. Maurer and P. Vadivelu, *J. Phys. Chem. A*, 2008, **112**, 13028-13036.
184. A. Bassan, M. R. A. Blomberg, P. E. M. Siegbalm and L. Que, Jr., *Chem. Eur. J.*, 2005, **11**, 692-705.
185. K. Chen and L. Que, Jr., *J. Am. Chem. Soc.*, 2001, **123**, 6327-6337.
186. E. G. Kovaleva and J. D. Lipscomb, *Nat. Chem. Biol*, 2008, **4**, 186-193.
187. A. Decker, M. S. Chow, J. N. Kemsley, N. Lehnert and E. I. Solomon, *J. Am. Chem. Soc.*, 2006, **128**, 4719-4733.
188. D. Danovich and S. Shaik, *J. Am. Chem. Soc.*, 1997, **119**, 1773-1786.
189. S. Shaik, H. Hirao and D. Kumar, *Acc. Chem. Res.*, 2007, **40**, 532-542.
190. A. Decker, J. Rohde, E. J. Klinker, S. D. Wong, L. Que, Jr. and E. I. Solomon, *J. Am. Chem. Soc.*, 2007, **129**, 15983-15996.
191. J. C. Schöneboom, S. Cohen, H. Lin, S. Shaik and W. Thiel, *J. Am. Chem. Soc.*, 2004, **126**, 4017-4034.
192. S. Shaik, D. Kumar and S. P. de Visser, *J. Am. Chem. Soc.*, 2008, **130**, 10128-10140.
193. D. Kumar, H. Hirao, L. Que, Jr. and S. Shaik, *J. Am. Chem. Soc.*, 2005, **127**, 8026-8027.
194. L. Bernasconi and E. J. Baerends, *Eur. J. Inorg. Chem.*, 2008, 1672-1681.
195. L. Bernasconi, M. J. Louwerse and E. J. Baerends, *Eur. J. Inorg. Chem.*, 2007, 3023-3033.
196. B. Ensing, F. Buda, M. C. M. Gribnau and E. J. Baerends, *J. Am. Chem. Soc.*, 2004, **126**, 4355-4365.
197. S. P. de Visser, *J. Am. Chem. Soc.*, 2006, **128**, 15809-15818.
198. R. Latifi, M. Bagherzadeh and S. P. de Visser, *Chem. Eur. J.*, 2009, **15**, 6651-6662.
199. J. T. Groves and G. A. Mcclusky, *J. Am. Chem. Soc.*, 1976, **98**, 859-861.
200. O. Pestovsky, S. Stoian, E. L. Bominaar, X. P. Shan, E. Munck, L. Que, Jr. and A. Bakac, *Angew. Chem. Int. Ed.*, 2005, **44**, 6871-6874.
201. M. L. Neidig, A. Decker, O. W. Choroba, F. Huang, M. Kavana, G. R. Moran, J. B. Spencer and E. I. Solomon, *Proc. Natl. Acad. Sci. USA.*, 2006, **103**, 12966-12973.
202. F. Weigend and R. Ahlrichs, *Phys. Chem. Chem. Phys.*, 2005, **7**, 3297-3305.
203. F. Weigend and M. Haser, *Theor. Chem. Acc.*, 1997, **97**, 331-340.
204. J. Olah and J. N. Harvey, *J. Phys. Chem. A*, 2009, **113**, 7338-7345.
205. J. F. Berry, S. Debeer. George and F. Neese, *Phys. Chem. Chem. Phys.*, 2008, **10**, 4361-4374.
206. A. Ghosh, E. Tangen, H. Ryeng and P. R. Taylor, *Eur. J. Inorg. Chem.*, 2004, 4555-4560.
207. F. Neese, *J. Inorg. Biochem.*, 2006, **100**, 716-726.
208. N. Strickland and J. N. Harvey, *J. Phys. Chem. B*, 2007, **111**, 841-852.
209. D. J. Lowe and R. N. F. Thorneley, *Biophys. J.*, 1984, **224**, 877-886.
210. D. J. Lowe and R. N. F. Thorneley, *Biophys. J.*, 1984, **224**, 895-901.
211. R. N. F. Thorneley and D. J. Lowe, *Biophys. J.*, 1984, **224**, 887-894.
212. R. N. F. Thorneley and D. J. Lowe, *Biophys. J.*, 1984, **224**, 903-909.
213. J. T. Groves and Y.-Z. Han, *In Cytochrome P-450. Structure, Mechanism, and Biochemistry*, Plenum Press, New York, 1995.
214. L. Que, Jr. and R. Y. N. Ho, *Chem. Rev.*, 1996, **96**, 2607-2624.
215. J. L. Li, X. Zhang and X. R. Huang, *Phys. Chem. Chem. Phys.*, 2012, **14**, 246-256.
216. C. Y. Geng, S. Ye and F. Neese, *Angew. Chem. Int. Ed.*, 2010, **49**, 5717-5720.
217. F. Ogliaro, S. P. de Visser and S. Shaik, *J. Inorg. Biochem.*, 2002, **91**, 554-567.
218. L. Que, Jr. and W. B. Tolman, *Nature*, 2008, **455**, 333-340.

219. A. Bassan, M. R. A. Blomberg, P. E. M. Siegbahn and L. Que, *Angew. Chem. Int. Ed.*, 2005, **44**, 2939-2941.
220. A. Bassan, M. R. A. Blomberg, P. E. M. Siegbahn and L. Que, Jr., *J. Am. Chem. Soc.*, 2002, **124**, 11056-11063.
221. A. Company, Y. Feng, M. Guell, X. Ribas, J. M. Luis, L. Que, Jr. and M. Costas, *Chem. Eur. J.*, 2009, **15**, 3359-3362.
222. S. Kundu, J. V. Thompson, A. D. Ryabov and T. J. Collin, *J. Am. Chem. Soc.*, 2011, **133**, 18546-18549.
223. M. L. Hoppe, E. O. Schlemper and R. K. Murmann, *Acta Crystallogr B*, 1982, **38**, 2237-2239.
224. M. Herren and H. U. Gudel, *Inorg. Chem.*, 1992, **31**, 3683-3684.
225. M. Atanasov, H. Adamsky and K. Eifert, *J. Solid. State. Chem*, 1997, **128**, 1-16.
226. K. Wissing, M. T. Barriuso, J. A. Aramburu and M. Moreno, *J. Chem. Phys*, 1999, **111**, 10217-10228.
227. R. J. Audette, J. W. Quail and P. J. Smith, *Tetrahedron Lett*, 1971, 279-&.
228. Y. Tsuda and S. Nakajima, *Chem. Lett*, 1978, 1397-1398.
229. M. D. Johnson and B. J. Hornstein, *Inorg. Chim. Acta*, 1994, **225**, 145-150.
230. H. Goff and R. K. Murmann, *J. Am. Chem. Soc.*, 1971, **93**, 6058-&.
231. L. Delaude and P. Laszlo, *J. Org. Chem*, 1996, **61**, 6360-6370.
232. M. D. Johnson and J. F. Read, *Inorg. Chem.*, 1996, **35**, 6795-6799.
233. A. E. Shilov and A. A. Shteinman, *Acc. Chem. Res.*, 1999, **32**, 763-771.
234. T. Kamachi and K. Yoshizawa, *J. Am. Chem. Soc.*, 2003, **125**, 4652-4661.
235. J. P. Guthrie, *J. Am. Chem. Soc.*, 1996, **118**, 12886-12890.
236. J. M. Mayer, *Acc. Chem. Res.*, 2011, **44**, 36-46.
237. J. A. Labinger and J. E. Bercaw, *Nature*, 2002, **417**, 507-514.
238. B. J. Wallar and J. D. Lipscomb, *Chem. Rev.*, 1996, **96**, 2625-2657.
239. M. Merkx, D. A. Kopp, M. H. Sazinsky, J. L. Blazyk, J. Muller and S. J. Lippard, *Angew. Chem. Int. Ed.*, 2001, **40**, 2782-2807.
240. K. E. Liu, A. M. Valentine, D. L. Wang, B. H. Huynh, D. E. Edmondson, A. Salifoglou and S. J. Lippard, *J. Am. Chem. Soc.*, 1995, **117**, 10174-10185.
241. S. K. Lee, B. G. Fox, W. A. Froland, J. D. Lipscomb and E. Munck, *J. Am. Chem. Soc.*, 1993, **115**, 6450-6451.
242. B. F. Gherman, S. J. Lippard and R. A. Friesner, *J. Am. Chem. Soc.*, 2005, **127**, 1025-1037.
243. E. A. Ambundo, R. A. Friesner and S. J. Lippard, *J. Am. Chem. Soc.*, 2002, **124**, 8770-8771.
244. S. K. Lee, J. C. Nesheim and J. D. Lipscomb, *J. Biol. Chem*, 1993, **268**, 21569-21577.
245. J. A. Broadwater, J. Y. Ai, T. M. Loehr, J. Sanders-Loehr and B. G. Fox, *Biochemistry.*, 1998, **37**, 14664-14671.
246. L. J. Murray, S. G. Naik, D. O. Ortillo, R. Garcia-Serres, J. K. Lee, B. H. Huynh and S. J. Lippard, *J. Am. Chem. Soc.*, 2007, **129**, 14500-14510.
247. V. V. Vu, J. P. Emerson, M. Martinho, Y. S. Kim, E. Münck, M. H. Park and L. Que, *Proc. Natl. Acad. Sci. USA.*, 2009, **106**, 14814-14819.
248. G. Q. Xue, A. Pokutsa and L. Que, Jr., *J. Am. Chem. Soc.*, 2011, **133**, 16657-16667.
249. E. Mu and L. Que, Jr., *PNAS*, 2008, **105**, 20615-20620.
250. G. Xue, R. De Hont, E. Münck and L. Que, Jr., *Nature Chem.*, 2010, **2**, 400-405.

251. A. Chanda, X. P. Shan, M. Chakrabarti, W. C. Ellis, D. L. Popescu, F. T. de Oliveira, D. Wang, L. Que, T. J. Collins, E. Münck and E. L. Bominaar, *Inorg. Chem.*, 2008, **47**, 3669-3678.
252. G. T. Rowe, E. V. Rybak-Akimova and J. P. Caradonna, *Inorg. Chem.*, 2007, **46**, 10594-10606.
253. G. T. Rowe, E. V. Rybak-Akimova and J. P. Caradonna, *Chem. Eur. J.*, 2008, **14**, 8303-8311.
254. P. E. M. Siegbahn and R. H. Crabtree, *J. Am. Chem. Soc.*, 1997, **119**, 3103-3113.
255. D. Rinaldo, D. M. Philipp, S. J. Lippard and R. a. Friesner, *J. Am. Chem. Soc.*, 2007, **129**, 3135-3147.
256. A. Fiedler, D. Schroder, S. Shaik and H. Schwarz, *J. Am. Chem. Soc.*, 1994, **116**, 10734-10741.
257. K. Yoshizawa, Y. Shiota and T. Yamabe, *Chem. Eur. J.*, 1997, **3**, 1160-1169.
258. M.-h. Baik, M. Newcomb, R. A. Friesner and S. J. Lippard, 2003.
259. H. F. Hsu, Y. H. Dong, L. J. Shu, V. G. Young and L. J. Que, *J. Am. Chem. Soc.*, 1999, **121**, 5230-5237.
260. J. M. Bollinger, S. X. Chen, S. E. Parkin, L. M. Mangravite, B. A. Ley, D. E. Edmondson and B. H. Huynh, *J. Am. Chem. Soc.*, 1997, **119**, 5976-5977.
261. M. Martinho, G. Q. Xue, A. T. Fiedler, L. J. Que, E. L. Bominaar and E. Münck, *J. Am. Chem. Soc.*, 2009, **131**, 5823-5830.
262. R. F. De Hont, G. Xue, M. P. Hendrich, L. Que, Jr., E. L. Bominaar and E. Münck, *Inorg. Chem.*, 2010, **49**, 8310-8322.
263. J. M. Mayer, *Biomimetic Oxidants Catalyzed by Transition Metal Complexes*, Imperial College Press, London, 2000.
264. S. P. de Visser, *J. Am. Chem. Soc.*, 2010, **132**, 1087-1097.
265. A. Gerli, M. Sabat and L. G. Marzilli, *J. Am. Chem. Soc.*, 1992, **114**, 6711-6718.
266. D. Kumar, S. P. De Visser and S. Shaik, *J. Am. Chem. Soc.*, 2004, **126**, 5072-5073.
267. J. L. M. Abboud, R. Notario, M. Berthelot, R. M. Claramunt, P. Cabildo, J. Elguero, M. J. Elghomari, W. Bouab, R. Mokhlisse and G. Guiheneuf, *J. Am. Chem. Soc.*, 1991, **113**, 7489-7493.
268. H. Hirao, D. Kumar, W. Thiel and S. Shaik, *J. Am. Chem. Soc.*, 2005, **127**, 13007-13018.
269. N. Sutin, *Prog Inorg Chem*, 1983, **30**, 441-498.
270. Generally, the concept of an intrinsic barrier was developed for ET theory, and λET can be defined as the energy to distort the reactants to the nuclear configuration of the products without the electron transferring. This ET has been proved to work just as well for reactions in which H• is transferred.89,90 In this semiclassical model, λHAT is the energy to take the reactants to the configuration of the product without the H• (e- and H+) transferring. In computational chemistry, λHAT is usually obtained from the self-exchange reaction in which the reactants first diffuse together to form a precursor complex (PC) and then undergoes reaction to form a successor complex (SC) that dissociates to products. Unfortunately, computational comparison among these diiron self-exchange reactions proved problematic, since they are susceptible to steric effects. The bulky groups on each of the separated diiron reactions limit the close association of the proton donor and acceptor. So that neither a hydrogen-bonded complex (PC) nor a true transition state for the diiron self-exchange reactions could be

located. Pseudo-self-exchange reaction in which we tried to substitute the bulky TPA ligands with ammonia or other simple ligands were also failed.
271. M. Christmann, *Angew. Chem. Int. Ed.*, 2008, **47**, 2740-2742.
272. A. Bondi, *J. Phys. Chem.*, 1964, **68**, 441.
273. The DHA H-abstaction by 1-Fcis proved problematic, since the other hydrogen atoms of the substrate are susceptible to the attraction of F atom, forming hydrogen bonds between them. Therefore, we cannot directly compare the HAT reactivity of 1-Fcis with the others since the newly formed hydrogen may exert influence on its reactivity.
274. D. Janardanan, D. Usharani, H. Chen and S. Shaik, *J. Phys. Chem. Lett*, 2011, **2**, 2610-2617.